The Pennsylvania State University
The Graduate School
College of Engineering

DEVELOPMENT OF MODELING AND SIMULATION TOOLS FOR ANALYSIS OF DUCTED FAN AIRCRAFT

A Thesis in
Aerospace Engineering
by
Eric L. Tobias

Submitted in Partial Fulfillment
of the Requirements
for the Degree of

Master of Science

August 2008

The thesis of Eric L. Tobias was reviewed and approved* by the following:

Joseph F. Horn
Associate Professor of Aerospace Engineering
Thesis Advisor

Dennis K. McLaughlin
Professor of Aerospace Engineering

Edward C. Smith
Professor of Aerospace Engineering

George A. Lesieutre
Professor of Aerospace Engineering
Head of the Department of Aerospace Engineering

*Signatures are on file in the Graduate School.

Abstract

A generic simulation model was developed for stability / control analysis and real-time simulation of ducted fan aircraft. The simulation environment was produced concurrently in MATLAB for rapid model development, as well as in FLIGHTLAB for comparison and validation. The generic simulation model features a modified inflow model for ducted rotors, a basic model of control vane forces and moments, and empirical correction factors to account for duct thrust augmentation, duct pitching moment, and flow turning effects. Two empirical flow turning efficiency factors, one applied before the plane of the rotor, k_{χ_R}, and the other from freestream to far-wake flow, denoted by k_{χ_∞}, were investigated. A range of k_{χ_R} values of 0.20 to 0.75 and a range of k_{χ_∞} values of 0.20 to 0.90 were successfully implemented. A model of duct pitching moment was developed in which the duct thrust offset normalized by the rotor radius is given as a function of airspeed. Wind tunnel data and literature from several sources have been analyzed and compared in order to refine the pitching moment model and tune the empirical factors. Validation of the simulation model is provided through correlation studies with experimental data of a 29-inch ducted fan UAV. Steady-state, trim, and maneuver results obtained using both the generic simulation model and FLIGHTLAB model are presented and discussed.

Table of Contents

List of Figures

List of Tables

List of Symbols

u, v, w	Body Axis Velocities (Longitudinal, Lateral, Vertical)
p, q, r	Body Angular Rates (Roll, Pitch, Yaw)
ϕ, θ, ψ	Euler Angles (Roll, Pitch, Yaw)
X, Y, Z	Body Axis Forces (Longitudinal, Lateral, Vertical)
L, M, N	Body Axis Moments (Roll, Pitch, Yaw)
A	Area
α	Angle of Attack
B	Blade Tip Loss Factor
β	Sideslip Angle
C_d	Section Drag Coefficient
C_l	Section Lift Coefficient
C_M	Pitching Moment Coefficient
c	Chord Length
D	Drag
δ_{col}	Collective Stick Displacement
δ_{lat}	Lateral Cyclic Stick Displacement
δ_{lon}	Longitudinal Cyclic Stick Displacement

δ_{ped}	Yaw Pedal Displacement
g	Acceleration due to Gravity
k_{aug}	Thrust Augmentation Factor
k_χ	Flow Turning Efficiency Factor
L	Lift
μ	Advance Ratio
μ'	Airspeed Ratio
Ω	Rotor Speed
Q	Torque
q	Dynamic Pressure
R	Rotor Radius
Re	Reynolds Number
r_0	Blade Root Cutout
ρ	Air Density
S	Planform Area
T	Thrust
θ_0	Collective Pitch
θ_{1c}	Longitudinal Cyclic Pitch (Rigid Rotor)
θ_{1s}	Lateral Cyclic Pitch (Rigid Rotor)
θ_{tw}	Blade Linear Twist
v_i	Induced Velocity
W	Weight
χ	Wake Skew Angle

Subscripts

0	Freestream
∞	Far-Wake
b	Blade
D	Duct
f	Fuselage
h	Hub
m	Momentum
R	Rotor
seg	Blade Segment
v	Vane
w	Wind

Acknowledgments

I would like to acknowledge my advisor, Dr. Joe Horn, for his support and encouragement throughout the entirety of my graduate studies. His knowledge and experience was invaluable and I clearly could not have completed this thesis without him. I would also like to recognize my fellow students, especially Brian Geiger and Wei Guo, for their resources and patience with my frequent questions.

I'd like to acknowledge Dr. Mark Tischler and Christy Ivler of the Army Aeroflightdynamics Directorate at NASA Ames Research Center for their contribution of the 29-inch ducted fan UAV wind tunnel data. The data sets were a key element in the formulation and validation of our model.

Most importantly, I would like to express my deepest appreciation for the support, confidence and love provided to me by my family and Penelope. My graduate work would not have been possible without such blessings and I am forever grateful.

This project was sponsored by the Office of Naval Research, Grant Number N00014-06-1-0205, with Technical Monitor Mr. Michael Fallon.

Dedication

To the late Edward Paul Tobias.

Chapter 1

Background and Literature Review of Ducted Fan Modeling

1.1 Background of Ducted Fan Aircraft

1.1.1 Brief History

The idea of using ducted rotors for the production of lift in Vertical Take-Off and Landing (VTOL) aircraft is not at all a new idea. Although many advances have been made in the development and production of ducted rotor vehicles, the basic principles are still the same. The vision of "flying cars" has been around since the birth of aviation itself. The goal was to not only have these "flying cars" used for special operations, such as for law enforcement and military use, but to also provide the average citizen an advanced form of transportation. One of the first successful vertical flight vehicles in which ducted rotors were utilized was the Piasecki VZ-8 Flying Geep of the late 1950s, as seen in Figure 1.1. The VZ-8 was a medium-sized utility vehicle that was powered by two reciprocating engines and generated lift with two ducted rotors orientated in a tandem configuration.

A few initial setbacks for this type of aircraft configuration included poor performance and controllability, compliance issues with regular FAA safety standards, and a small demand for non-conventional VTOL aircraft [1]. With advances in technology, particularly in the area of automated flight control and fly-by-wire systems, the basic ideas originally proposed many years ago are now successfully

Figure 1.1. Piasecki VZ-8 Flying Geep.

being developed with improved performance and increased usefulness. Modern technology not only allows for the improvement of performance and safety of these vehicles, but it also improves the economics and practicality associated with the development and production.

1.1.2 Advantages of Ducted Fan Systems

A prominent advantage of ducted propulsion is better overall efficiency at low speeds when compared to a conventional rotor. One reason for this increase in efficiency is the reduction of blade tip losses. When properly designed there are very small clearances between the rotor blade tips and the inside wall of the duct, thus reducing pressure losses usually associated with a conventional rotor. Another key contributer to the efficiency of ducted rotors is the effect the duct has on the wake produced. Efficiency is sacrificed when the wake of a rotor naturally contracts on a conventional helicopter. The inside wall of the shroud provides a predetermined cross section and, when carefully designed, it ensures a uniform wake size [2]. In addition, thrust is produced by the duct itself because of the suction force developed at the leading edge of the duct as the flow is accelerated into the rotor [3].

Empirical data show that the total thrust produced by a ducted rotor system in hover is usually 20 to 50 percent greater than that of an identical unducted rotor operating at the same power [3]. This is an outstanding feature of ducted propulsion, and therefore it is highly desirable in the application of vertical take-off vehicles.

Reduction of noise is also a benefit of using ducted propulsion. Noise is reduced by physically shielding the rotor and possibly components of the power plant, such as the engine or transmission. Blade tip vortices are also natural producers of noise on rotorcraft. Reducing the flow of high pressure air from the bottom of the rotor disk to the top weakens the strength of the vortices, thus attenuating the noise generated.

Perhaps the most prominent feature of encasing a rotor within a duct, especially when used for precision flight near the ground, is greatly improving safety by placing a physical barrier between the rotor and its surroundings. Also, the inclusion of control vanes at the inlet and exit of the duct may also provide a barrier from the bottom and top of the rotor, thus potentially isolating the rotor completely from outside obstacles. The duct not only protects the rotor from coming into contact with obstacles during flight, but it also protects people around the aircraft prior to flight, such as ground crew or other personnel.

1.1.3 Issues with Ducted Fan Systems

Although there are several key advantages of ducted rotors over the conventional configuration, there are also a few challenging issues. One significant disadvantage is the strong nose-up pitching moment produced by the duct in edgewise flight. The pitching moment is caused by the dissymmetry of lift produced by the duct itself because of the unequal flow experienced by the front and aft sections of the duct. Momentum drag, or ram drag, is the drag caused by the turning of the flow from the freestream direction into the axial direction of the duct. The momentum drag may be very large and must be accounted for.

Control vanes at the exit of the duct may loose effectiveness during certain flight conditions. Although the wake skew angle formed by a ducted rotor in forward flight is generally less than that of an unducted rotor, the skew angle may still be large at times. Knowledge of the wake skew characteristics for a range of flight conditions is necessary in order to properly design exit control vanes.

Most of the other issues with ducted propulsion arise when trying to model an entire ducted rotor system. There are significant interactions between the rotor and the duct that may change based on the flight condition, and accurately modeling

these interactions may be difficult. Also, there may be unpredictable characteristics when flow separation occurs at the lip of the duct. Experimental results may be necessary in order to capture these effects and successfully account for them.

1.2 Literature Review of Ducted Fan Research

A significant amount of theoretical and experimental research has been done solely on the aerodynamics of a rotor within a duct. However, as the usefulness of ducted rotor designs has become more evident, more research has subsequently been conducted on other aspects of the ducted rotor system, such as performance characteristics, controllability, acoustic properties, and simulation modeling.

1.2.1 CFD Analysis

Computational fluid dynamics analysis of a ducted rotor system with validation is presented in a paper by Chang and Rajagopalan [4]. The paper outlines the development of a grid and an axisymmetric, incompressible Navier-Stokes solver used to calculate the flow through a ducted rotor system. The results were then validated using wind tunnel data of the duct in hovering conditions. Also in a paper by Guerrero *et al* [5], specific aerodynamic characteristics of ducted fans are explored and generalized into an aerodynamic prediction methodology, which was then validated using wind tunnel data. These results were then compiled into a design optimization computer program applicable for a wide range of ducted rotor designs.

A study of the dynamic relations between collective pitch and thrust produced by a ducted rotor system is presented by Alpman and Long [6]. CFD analysis was used for the flowfield predictions, in which thrust and moment response was studied in hover and forward flight conditions. Findings on the transient response and thrust buildup of the ducted system are also discussed.

Results of the CFD analysis, as validated by experimental wind tunnel testing, show that accurate representations of the flow through a ducted rotor system can be obtained. The results also confirm that the interactions between the rotor and the shroud can be captured computationally, which is important for the formulation

of simulation models.

1.2.2 Performance and Stability

Performance and stability analysis of various ducted fan models have been investigated and tested using many different methods. Lind *et al* [7] researched ducted rotor performance using a computer module as well as experimental wind tunnel data. The research mainly concentrated on thrust produced by the duct and rotor system, as well as the aerodynamic pitching moments experienced by the model in an array of flow conditions. Avanzini *et al* [8] present a model formed by numerical analysis of the flowfield around the airframe of a ducted fan vehicle and investigate the performance and stability characteristics.

In a paper by De Divitiis [9], the aerodynamic coefficients of two ducted fan models were calculated. The research concentrated on the complex flow interaction between the rotor and the shroud, and two separate models were developed to better interpret this interaction. One model was used to determine the aerodynamic coefficients of the shroud itself, and the other was used to calculate thrust and moment data for the rotor. Performance and stability were then studied for significant flight conditions.

Results of the performance and stability analysis indicate that the presence of a substantial pitching moment greatly affects the performance of a shrouded rotor vehicle by limiting its operational range. It was also found that the vehicle's moment derivatives with respect to angular velocity have an important effect on stability. An accurate evaluation of the moment derivatives through wind tunnel testing is necessary to insure the vehicle's stability throughout the maneuvering envelope.

1.2.3 Controllability

Controllability of ducted rotor systems has also been a heavily researched topic. The development and testing of linear controllers for an unmanned ducted fan vehicle is described in an article by Avanzini *et al* [10]. After the development of the controllers, the system was then tested and compared against rotorcraft handling qualities specifications. The system was also tested using simulated flight condi-

tions and various aircraft configurations. The flight control system demonstrated good handling qualities in real-time simulation testing.

Hess and Bakhtiari-Nejad [11] present a sliding mode control design for use in an unmanned ducted fan aircraft. This control system is applicable to a nonlinear, unstable and coupled model in various flight conditions. The effects of this controller were then tested using a computer simulation. It was shown that a sliding mode control system, with the inclusion of gain scheduling, was capable of controlling a nonlinear and unstable vehicle.

A dynamic inversion control system was developed and analyzed for a small ducted fan UAV, as presented by Spaulding *et al* [12]. The nonlinear dynamic inversion is completed using experimental wind tunnel data and state feedback. The research focuses on control robustness, gust rejection and vehicle velocity control. Similar research was conducted by Johnson *et al* [13], with the addition of neural-network adaptation and extensive flight test data to validate the characteristics of the developed simulation model and controller. It was concluded that a dynamic inversion control system effectively reduces the complex aircraft dynamics throughout the entire flight envelope without the use of gain scheduling.

Through the research on controllability it was found that an advanced control system may be required for stability of certain ducted fan UAVs, due to the vehicle's nonlinear and unstable characteristics. It is apparent that the intended mission of the vehicle dictates the complexity of the control system as well.

1.2.4 Simulation Modeling

Modeling of an entire ducted fan system is of great interest when wanting to properly simulate the flight characteristics of an applicable aircraft. In a paper by Xin and He [14], a ducted fan simulation model was developed for UAV lifting applications. The model was developed using nonuniform and unsteady flow analysis; thus the model can effectively be used for both steady and unsteady flight conditions. The model was investigated through a series of flight conditions, including axial flight and crosswind conditions, to validate the accuracy of the model in realistic conditions. It also incorporates the aerodynamic interactions between the duct and the fan, which greatly improves the realistic nature and usefulness of the

model.

The work conducted by Xin and He forms the basis for the ducted fan model included as a standard component in FLIGHTLAB. The ducted fan FLIGHTLAB model is discussed in greater detail in Chapter 3.

Chapter 2

Development of Generic Ducted Fan Simulation Model

A generic, modular ducted fan simulation model was developed in order to effectively and accurately model a range of configurations of ducted fan aircraft. The model was implemented in MATLAB for ease of development and to provide a user-friendly environment. This chapter documents the theory behind the various elements of the generic ducted fan simulation model including the inflow, rotor, shroud, exit control vanes, and pitching moment model.

2.1 Derivation of Inflow

There are fundamental differences in the inflow characteristics of a ducted rotor as opposed to an open rotor. The duct has an influence on the inflow in two distinct ways. Firstly, the duct produces an additional lift force due to suction on the lip of the duct that must be considered in the momentum conservation analysis. Also, the duct causes a flow turning effect that tends to align the flow with the axis of the duct when it is operating near edgewise flight. Modeling inflow characteristics properly is critical since the inflow affects both the rotor performance and the forces generated by the control vanes in the exit flow.

Two inflow models were developed that are modifications of basic momentum theory inflow of an open rotor. The method in which the flow turning effects are modeled in each, however, are different. The first inflow model was used for

preliminary analysis and applies a reduction in the horizontal component of the flow velocity before and after the rotor. However, after comparison of results obtained using other simulation models and a review of wind tunnel data, it was deduced that modeling the turning of the velocity vector (rather than simply reducing the horizontal component) would improve the accuracy of the model. Therefore, a more advanced inflow derivation that accounts for the turning of the flow before and after the plane of the rotor is used to formulate the second inflow model.

2.1.1 Inflow Model 1

An illustration of the original inflow model is shown in Figure 2.1. Note that only the horizontal component of the freestream velocity vector, $\mathbf{V_0}$, is affected by the duct before and after the plane of the rotor. The vertical component of the flow is affected, however, upstream of the rotor by the increased vertical velocity induced by the rotor, v_i. Because the rotor disk encounters a flow that is similar to that of an open rotor, it is assumed that a translational lift effect is experienced by the ducted rotor system.

It is assumed that the total force vector, $\mathbf{T}$, consists of a vertical thrust component and a horizontal momentum drag component,

$$\mathbf{T} = D_m \boldsymbol{i} + T \boldsymbol{j} \ . \tag{2.1}$$

The thrust component of the total force vector is a combination of rotor thrust and duct thrust,

$$T = T_R + T_D = (1 + k_{aug})\, T_R \ , \tag{2.2}$$

in which the thrust augmentation factor, k_{aug}, represents the increase in thrust due to the duct lift effect. A k_{aug} value of 1 corresponds to a duct that generates the same amount of lift as the rotor, thus the total thrust of the ducted rotor system would be twice that of the rotor alone. However, a range of k_{aug} values of approximately 0.2 to 0.4 were primarily investigated in this simulation model.

The rotor induces a downward velocity component, v_i, at the plane of the rotor, as well as far downstream, denoted by v_∞. Because of the duct flow turning factor, k_χ, it is assumed that the horizontal velocity component is reduced at the rotor

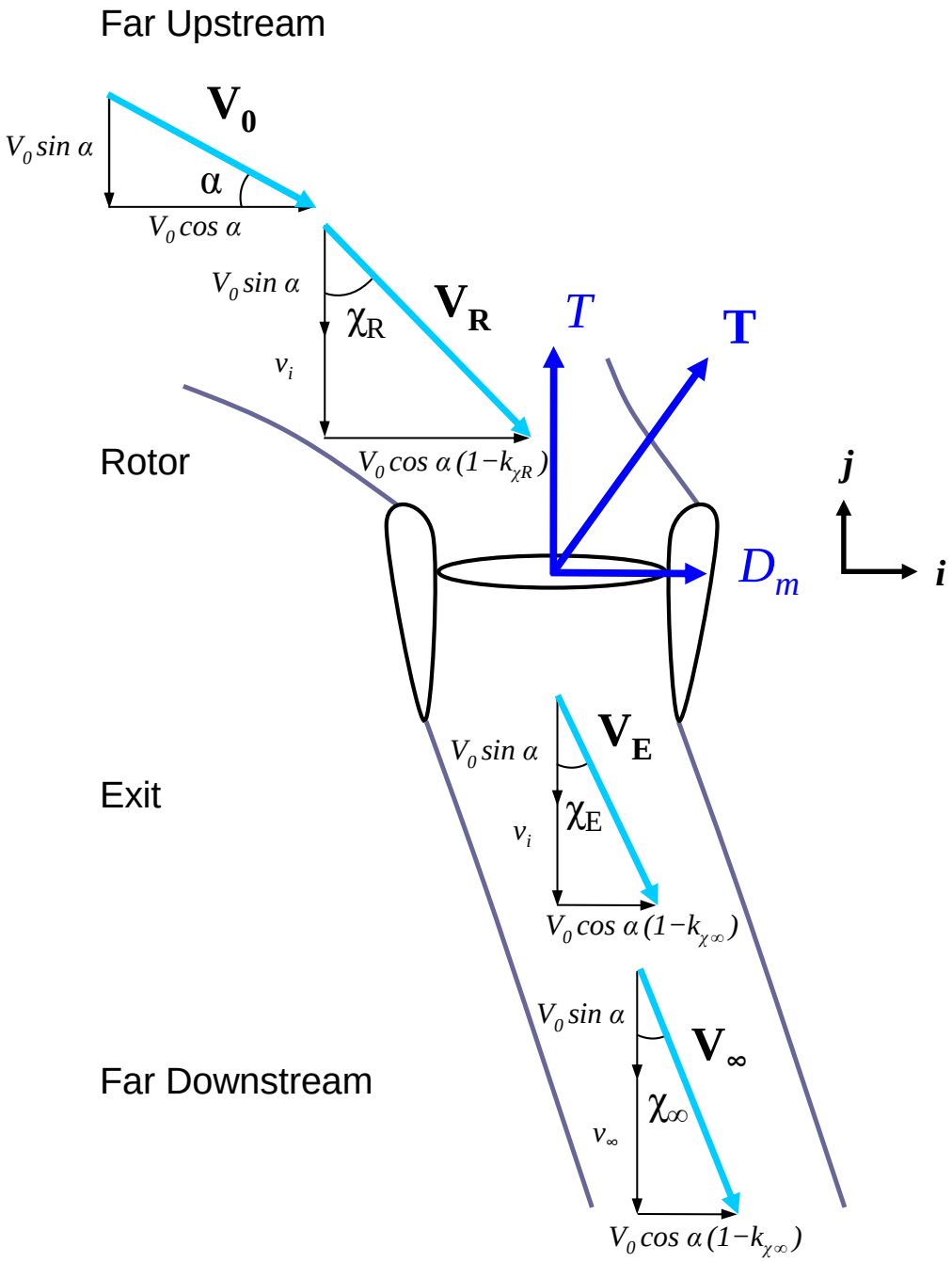

Figure 2.1. Inflow Model 1 Illustration.

disk in the duct. Based on the assumptions, the flow velocity vectors upstream of the rotor, at the disk of the rotor, and far downstream of the rotor are presented below.

$$\begin{aligned} \mathbf{V_0} &= V_0 \cos\alpha\, \boldsymbol{i} - V_0 \sin\alpha\, \boldsymbol{j} \\ \mathbf{V_R} &= (1 - k_{\chi_R})\, V_0 \cos\alpha\, \boldsymbol{i} - (V_0 \sin\alpha + v_i)\, \boldsymbol{j} \\ \mathbf{V_\infty} &= (1 - k_{\chi_\infty})\, V_0 \cos\alpha\, \boldsymbol{i} - (V_0 \sin\alpha + v_\infty)\, \boldsymbol{j} \end{aligned} \tag{2.3}$$

Note that when $k_{\chi_R} = 0$ the flow is affected by the duct only after the plane of the rotor. When $k_{\chi_\infty} = 1$ the flow is completely turned to align with the axis of the duct, which results in only a vertical component of the velocity vector far downstream of the rotor. If $k_{\chi_\infty} = 0$ the flow is deflected downward but not turned, which is equivalent to an open rotor. The corresponding wake skew angles at the duct and far downstream of the duct, given the velocity vectors in Equation 2.3, are shown below.

$$\chi = \tan^{-1}\left(\frac{(1 - k_{\chi_R})\, V_0 \cos\alpha}{V_0 \sin\alpha + v_i}\right) \tag{2.4}$$

$$\chi_\infty = \tan^{-1}\left(\frac{(1 - k_{\chi_\infty})\, V_0 \cos\alpha}{V_0 \sin\alpha + v_\infty}\right) \tag{2.5}$$

The mass flow rate of air through the duct is given by

$$\dot{m} = \rho\, A_D\, |\mathbf{V_R}| \ , \tag{2.6}$$

where ρ is the local air density and A_D is the duct area at the plane of the rotor. Conservation of momentum, which states that the total momentum of a closed system remains constant, is then applied across the stream tube. Conservation of momentum from freestream flow to the far-wake flow is given by

$$\mathbf{T} = \dot{m}\, (\mathbf{V_\infty} - \mathbf{V_0}) \ . \tag{2.7}$$

By considering only the horizontal component of Equation 2.7, the expression for momentum drag is found to be

$$D_m = \dot{m}\, ((1 - k_{\chi_\infty})\, V_0 \cos\alpha - V_0 \cos\alpha) = \dot{m}\, k_{\chi_\infty} V_0 \cos\alpha \ . \tag{2.8}$$

Similarly, considering only the vertical component of Equation 2.7, the expression

for thrust is given by

$$T = \dot{m}\,(V_0\,\sin\alpha + v_\infty - V_0\,\sin\alpha) = \dot{m}\,v_\infty\ , \tag{2.9}$$

which is consistent with momentum theory for an open rotor.

It is assumed that energy enters the system through the rotor thrust. Therefore conservation of energy, which states that the total energy of a closed system remains constant, can be applied. Conservation of energy from the freestream to the far-wake flow is shown in the following derivation.

$$\begin{gathered}
-\mathbf{T_R}\cdot\mathbf{V_R} = \frac{1}{2}\,\dot{m}\,(\mathbf{V_\infty}\cdot\mathbf{V_\infty} - \mathbf{V_0}\cdot\mathbf{V_0}) \\
T_R\,(V_0\sin\alpha + v_i) = \frac{1}{2}\,\dot{m}\,\left(((1-k_{\chi_\infty})\,V_0\cos\alpha)^2 + (V_0\sin\alpha + v_\infty)^2 - {V_0}^2\right) \\
\frac{T}{1+k_{aug}}\,(V_0\sin\alpha + v_i) = \frac{1}{2}\,\dot{m}\,\left(\left(k_{\chi_\infty}^2 - 2\,k_{\chi_\infty}\right){V_0}^2\cos^2\alpha + 2\,v_\infty V_0\sin\alpha + v_\infty^2\right)
\end{gathered} \tag{2.10}$$

Substituting the expression for thrust found in Equation 2.9, a quadratic expression is derived for the induced velocity far downstream from the duct, as shown below.

$$\begin{gathered}
\frac{\dot{m}\,v_\infty}{1+k_{aug}}\,(V_0\sin\alpha + v_i) = \frac{1}{2}\,\dot{m}\,\left(\left(k_{\chi_\infty}^2 - 2\,k_{\chi_\infty}\right){V_0}^2\cos^2\alpha + 2\,v_\infty V_0\sin\alpha + v_\infty^2\right) \\
v_\infty^2 + 2\left(\frac{k_{aug}\,V_0\sin\alpha - v_i}{1+k_{aug}}\right)v_\infty + \left(k_{\chi_\infty}^2 - 2\,k_{\chi_\infty}\right){V_0}^2\cos^2\alpha = 0
\end{gathered} \tag{2.11}$$

The induced velocity far downstream from the duct, v_∞, can be solved using the quadratic formula. Substituting expressions for v_∞ and $\dot{m}$ found in Equation 2.6 and Equation 2.9, respectively, yields the following expression.

$$\begin{gathered}
\sqrt{(1-k_{\chi_R})^2\,{V_0}^2\cos^2\alpha + (V_0\sin\alpha + v_i)^2} \\
\left(-\frac{k_{aug}\,V_0\sin\alpha - v_i}{1+k_{aug}} + \sqrt{\left(\frac{k_{aug}\,V_0\sin\alpha - v_i}{1+k_{aug}}\right)^2 - \left(k_{\chi_\infty}^2 - 2\,k_{\chi_\infty}\right){V_0}^2\cos^2\alpha}\right) \\
-\frac{T}{\rho\,A_D} = 0
\end{gathered} \tag{2.12}$$

The result is a relatively complex nonlinear algebraic equation. However, given

the thrust, freestream velocity, angle of attack, thrust augmentation and flow turning factors, the induced velocity at the rotor, v_i, can be solved using iterative numerical techniques.

2.1.2 Inflow Model 2

A revised inflow derivation was formulated that accounts for the turning of the velocity vectors rather than only a reduction in the horizontal components. The updated velocity vectors upstream of the rotor, at the disk of the rotor, and far downstream of the rotor are shown below.

$$\begin{aligned} \mathbf{V_0} &= V_0 \cos\alpha \boldsymbol{i} - V_0 \sin\alpha \boldsymbol{j} \\ \mathbf{V_R} &= V_0 \cos\left(\alpha + k_{\chi_R}\left(\frac{\pi}{2} - \alpha\right)\right)\boldsymbol{i} - \left(V_0 \sin\left(\alpha + k_{\chi_R}\left(\frac{\pi}{2} - \alpha\right)\right) + v_i\right)\boldsymbol{j} \\ \mathbf{V_\infty} &= V_0 \cos\left(\alpha + k_{\chi_\infty}\left(\frac{\pi}{2} - \alpha\right)\right)\boldsymbol{i} - \left(V_0 \sin\left(\alpha + k_{\chi_\infty}\left(\frac{\pi}{2} - \alpha\right)\right) + v_\infty\right)\boldsymbol{j} \end{aligned} \tag{2.13}$$

Note that the amount of flow turned before the rotor is a function of the rotor flow turning efficiency factor, denoted by k_{χ_R}. A k_{χ_R} value equal to k_{χ_∞} means that all of the flow turning is experienced before the plane of the rotor. An illustration of the velocity and force vectors of the revised inflow model are depicted in Figure 2.2, in which the affected angles of attack, denoted by α^R and α^∞, are given by

$$\alpha^R = \alpha + k_{\chi_R}\left(\frac{\pi}{2} - \alpha\right) \tag{2.14}$$

$$\alpha^\infty = \alpha + k_{\chi_\infty}\left(\frac{\pi}{2} - \alpha\right) \ . \tag{2.15}$$

The corresponding wake skew angles at the exit of the duct and far downstream are given as

$$\chi = \tan^{-1}\left(\frac{V_0 \cos\alpha^R}{V_0 \sin\alpha^R + v_i}\right) \tag{2.16}$$

$$\chi_\infty = \tan^{-1}\left(\frac{V_0 \cos\alpha^\infty}{V_0 \sin\alpha^\infty + v_\infty}\right) \ . \tag{2.17}$$

The mass flow rate is given by Equation 2.6 in the derivation of the first inflow model. Likewise, applying the conservation of momentum (Equation 2.7) yields

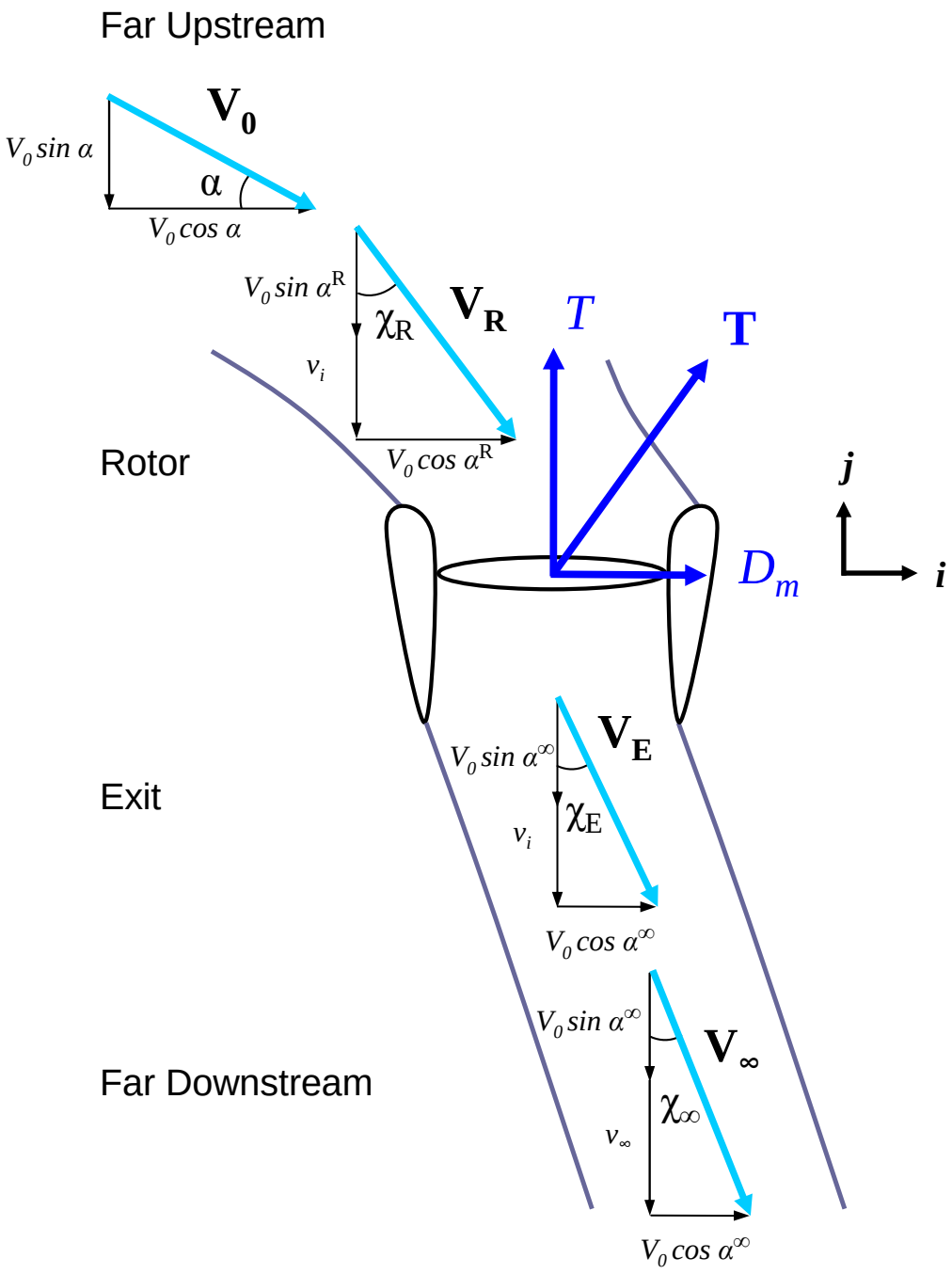

Figure 2.2. Inflow Model 2 Illustration.

the expressions for momentum drag and thrust as seen in the following equations.

$$D_m = \dot{m}\left(\cos\alpha - \cos\alpha^{\infty}\right) V_0 \tag{2.18}$$

$$T = \dot{m}\left(\left(-\sin\alpha + \sin\alpha^{\infty}\right) V_0 + v_{\infty}\right) \tag{2.19}$$

Conservation of energy (Equation 2.10) is then applied using the newly formulated velocity vectors (Equation 2.13), and the solution for thrust is then substituted. A quadratic expression for the induced velocity far downstream of the duct, v_{∞}, is found and the final result after substitution is an expression that is a function of induced velocity, v_i. The newly formulated inflow equation is given as

$$\begin{aligned} &\frac{1}{1+k_{aug}}\Bigg[v_i - \sin\alpha\, V_0 + \sin\alpha^R\, V_0 - \sin\alpha\, k_{aug}\, V_0 \\ &\qquad + \frac{1}{2}\Big[8\left(-\sin\alpha + \sin\alpha^{\infty}\right)\left(1+k_{aug}\right) V_0 \left(v_i + \sin\alpha^R\, V_0\right) \\ &\qquad + 4\left(v_i + \left(\sin\alpha^R - \sin\alpha^{\infty} - \sin\alpha^{\infty}\, k_{aug}\right) V_0\right)^2\Big]^{\frac{1}{2}}\Bigg] \\ &- \frac{T}{\rho\, A_D \sqrt{v_i^2 + 2\sin\alpha^R\, v_i\, V_0 + V_0^2}} = 0\ , \end{aligned} \tag{2.20}$$

where α^R and α^{∞} are defined in Equation 2.14 and Equation 2.15, respectively.

2.2 Model Documentation

This section outlines the various equations and code development theory used in the ducted fan simulation model. The complete MATLAB code can be found in Appendix B.

2.2.1 Blade Element Rotor Model

A blade element rotor is modeled within each duct. Blade Element Momentum Theory (BEMT) is used as the basis for determining the distribution of inflow and lift on the rotor blades. BEMT is a hybrid method that combines the principles of Blade Element Theory (BET) and momentum theory. BET works on the assumption that each rotor blade section acts as a quasi-two-dimensional airfoil

that produces aerodynamic forces and moments, and momentum theory provides a calculation of rotor thrust, power, and induced velocity [2].

Radial blade elements are defined, each with equal annular areas. The annular area can be calculated from

$$A_{annulus} = \frac{\pi\,(R^2 - r_0^2)}{NR}\ , \tag{2.21}$$

in which R is the radius of the rotor, r_0 is the blade root cutout, and NR is the number of radial blade elements. Six radial elements per blade is used as the default value. The radial location of the blade segment,

$$r_{seg} = \frac{1}{2}\,r_0 + \sqrt{\left(\frac{1}{2}\,r_0\right)^2 + \frac{A_{annulus}}{4\,\pi}}\ , \tag{2.22}$$

and the width of the blade segment,

$$dr = \frac{A_{annulus}}{2\,\pi\,r_{seg}}\ , \tag{2.23}$$

are used to determine the forces and moments over the entire rotor by summing the forces and moments created from the individual segments.

A series of different transformations are used throughout the code in order to represent forces and moments from one coordinate frame in the main body frame. The transformation matrix used to obtain the rotor shaft incidence, if any, relative to the body axes is represented by

$$\mathbf{T_{shaft}} = \begin{pmatrix} \cos i_{shaft} & 0 & \sin i_{shaft} \\ 0 & 1 & 0 \\ -\sin i_{shaft} & 0 & \cos i_{shaft} \end{pmatrix}\ , \tag{2.24}$$

where i_{shaft} is the rotor shaft incidence angle. The hub/wind axis velocities and angular rates are then calculated using the following matrix multiplication, which

includes the transformation matrix shown in Equation 2.24,

$$\mathbf{V_h} = \mathbf{T_{shaft}} \begin{pmatrix} u - q\, h_R - r\, y_R \\ v + p\, h_R + r\, x_R \\ w - q\, x_R + p\, y_R \end{pmatrix} = \begin{pmatrix} V_{h_x} \\ V_{h_y} \\ V_{h_z} \end{pmatrix} \tag{2.25}$$

in which h_R, x_R, and y_R are the vertical, longitudinal, and lateral locations, respectively, of the rotor hub relative to the vehicle c.g. The total velocity and the in-plane velocity in the hub/wind axis are found to be

$$V = |\mathbf{V_h}| \tag{2.26}$$

$$V_{inplane} = \sqrt{V_{h_x}^2 + V_{h_y}^2}\ . \tag{2.27}$$

The blade pitch, in degrees, can be calculated from the following set of equations for a counterclockwise rotor and clockwise rotor, respectively:

$$\begin{aligned} \theta_b &= \theta_0 + \theta_{1s} \sin\psi + \theta_{1c} \cos\psi \\ \theta_b &= \theta_0 - \theta_{1s} \sin\psi + \theta_{1c} \cos\psi \end{aligned} \tag{2.28}$$

in which θ_0 is the collective pitch and θ_{1s} and θ_{1c} are the lateral and longitudinal cyclic pitch, respectively, for a rigid rotor. The corresponding pitch of each blade segment can then be calculated using

$$\theta_{seg} = \theta_b + \theta_{tw}\, \frac{r_{seg} - r_0}{R - r_0}\ , \tag{2.29}$$

where θ_{tw} is the rotor blade linear twist angle.

The velocity vector at the plane of the rotor, $\mathbf{V_R}$, is calculated based on the selected inflow model. The x- and z-components of the velocity at the rotor for Inflow Model 1 and Inflow Model 2 are given by Equation 2.30 and Equation 2.31, respectively.

$$\begin{aligned} V_{R_x} &= V_{inplane}\,(1 - k_{\chi_R}) \\ V_{R_z} &= V_z + v_{i_0} \end{aligned} \tag{2.30}$$

$$\begin{aligned} V_{R_x} &= V\cos\left(\alpha + k_{\chi_R}\left(\frac{\pi}{2} - \alpha\right)\right) \\ V_{R_z} &= V\sin\left(\alpha + k_{\chi_R}\left(\frac{\pi}{2} - \alpha\right)\right) + v_{i_0} \end{aligned} \tag{2.31}$$

In either case, the total magnitude of the velocity at the rotor is given by

$$V_R = \sqrt{V_{R_x}^2 + V_{R_z}^2}\ . \tag{2.32}$$

After the flow velocity at the rotor is determined, the local velocity at each blade segment can then be calculated. Perpendicular velocity is defined as

$$V_p = -V_{R_z} - v_{i_0} + r_{seg}\left(p\ \sin\psi + q\ \cos\psi\right) \tag{2.33}$$

and tangential velocity for a counterclockwise rotor and a clockwise rotor, respectively, is given as

$$\begin{aligned} V_t &= r_{seg}\left(\Omega - r\right) + V_{R_x}\left(\sin\psi\cos\psi_w + \cos\psi\sin\psi_w\right) \\ V_t &= r_{seg}\left(\Omega + r\right) + V_{R_x}\left(\sin\psi\cos\psi_w - \cos\psi\sin\psi_w\right)\ , \end{aligned} \tag{2.34}$$

in which ψ_w is the azimuth angle of the relative wind. In addition, $\sin\psi_w$ and $\cos\psi_w$ can be written as

$$\sin\psi_w = \frac{V_{h_y}}{V} \tag{2.35}$$

$$\cos\psi_w = \frac{V_{h_x}}{V}\ . \tag{2.36}$$

The total magnitude of the velocity at the blade segment is defined as

$$V_{seg} = \sqrt{{V_p}^2 + {V_t}^2}\ . \tag{2.37}$$

Using the pitch of the blade segment and the local velocities shown above, the angle of attack of the blade segment is found to be

$$\alpha_{seg} = \theta_{seg} + tan^{-1}\left(\frac{V_p}{V_t}\right)\ . \tag{2.38}$$

Similarly, the Reynolds number of the blade segment is calculated using

$$Re_{seg} = \frac{\rho \, V_{seg} \, c}{\mu} \ , \tag{2.39}$$

in which ρ is the local air density, c is the blade chord at the segment, and μ is the local air viscosity.

Table lookups are then used to calculate lift coefficient, C_l, and drag coefficient, C_d, values for each blade segment at every azimuth location, given the angle of attack and Reynolds number of the blade segments. The perpendicular and tangential forces produced by each blade segment, in turn, are found using the following equations.

$$F_{p_{seg}} = \frac{1}{2} \, \rho \, c \, dr \, V_{seg} \left(C_{l_{seg}} \, V_t + C_{d_{seg}} \, V_p \right) \tag{2.40}$$

$$F_{t_{seg}} = \frac{1}{2} \, \rho \, c \, dr \, V_{seg} \left(C_{d_{seg}} \, V_t - C_{l_{seg}} \, V_p \right) \tag{2.41}$$

Finding the total forces and moments on each blade is accomplished by summing the forces and moments of each individual blade segment, as can be seen in the following sets of equations.

$$F_{p_b} = \sum F_{p_{seg}} \tag{2.42}$$

$$F_{t_b} = \sum F_{t_{seg}} \tag{2.43}$$

$$M_{f_b} = \sum F_{p_{seg}} r_{seg} \tag{2.44}$$

$$M_{l_b} = \sum F_{t_{seg}} r_{seg} \tag{2.45}$$

Total forces and moments generated by the rotor are then calculated by time

averaging the individual blade forces and moments over the rotor as shown by

$$\begin{aligned} L_R &= \sum \pm M_{f_b} \sin \psi Nb/N_\psi \\ M_R &= \sum M_{f_b} \cos \psi Nb/N_\psi \\ Q_R &= \sum M_{l_b} Nb/N_\psi \\ T_R &= \sum F_{p_b} Nb/N_\psi \\ X_R &= \sum -F_{t_b} \sin \psi Nb/N_\psi \\ Y_R &= \sum \pm F_{t_b} \cos \psi Nb/N_\psi \ , \end{aligned} \tag{2.46}$$

where L_R and Y_R are negative for a counterclockwise rotor.

2.2.2 Inflow Iteration

Once the thrust created by the ducted rotor system is determined, the quasi-steady induced velocity is found by iterating the inflow equation (Equation 2.12 when using Inflow Model 1 and Equation 2.20 when using Inflow Model 2). A Newton-Raphson iteration process is implemented, in which the previous solution to the quasi-steady inflow is used as the initial guess for the current iteration when running a sweep of velocities or when running a trim.

2.2.3 Vane Model

Exit control vanes are implemented in the ducted fan model. The exit control vanes are modeled as all-moving control surfaces that operate in the wake of the rotor, and provide yaw control and thrust augmentation. A table lookup of the vane cross section, a NACA 0012 airfoil [15], is used to determine the forces and moments produced by each control vane. A coordinate transformation is then used to convert the forces and moments from the vane axis into the rotor hub axis.

The flow velocity vector at the exit of the duct, denoted by $\mathbf{V_E}$, is computed from the chosen inflow model. The x- and z-components of the exit flow velocity vector for Inflow Model 1 and Inflow Model 2 are presented in Equation 2.47 and

Equation 2.48, respectively.

$$\begin{aligned} V_{E_x} &= V_{inplane}\,(1 - k_{\chi_\infty}) \\ V_{E_z} &= V_{R_z} \end{aligned} \tag{2.47}$$

$$\begin{aligned} V_{E_x} &= V\cos\left(\alpha + k_{\chi_\infty}\left(\frac{\pi}{2} - \alpha\right)\right) \\ V_{E_z} &= V\sin\left(\alpha + k_{\chi_\infty}\left(\frac{\pi}{2} - \alpha\right)\right) + v_{i_0} \end{aligned} \tag{2.48}$$

The total magnitude of the velocity at the exit of the duct is therefore

$$V_E = \sqrt{V_{E_x}^2 + V_{E_z}^2}\ . \tag{2.49}$$

A model of flow swirl velocity inside the duct is included in the ducted fan model, which improves the realistic nature of the model. The drag created by the spinning rotor tends to swirl the flow within the duct at a rotational speed proportional to the rotor torque [16]. The swirl velocity of the flow is given by

$$\Omega_{swirl} = \frac{Q_R}{\frac{1}{2}\,\rho\,A_D\,V_R\,R^2}\ , \tag{2.50}$$

in which Q_R is the rotor torque. Because of this added component to the exit flow velocity, proper care must be taken in order to properly orient the exit control vanes at a particular angle of attack. A uniform vane deflection bias may be implemented, in which all control vanes are deflected a few degrees. A more detailed discussion of the vane deflection bias can be found in Section 4.5 and Section 5.1.

The chordwise, spanwise, and normal velocities at the vane are denoted by u_v, v_v, and w_v, respectively. The vane velocities are found using the following transformation from hub-wind axes to vane axes:

$$\begin{pmatrix} u_v \\ v_v \\ w_v \end{pmatrix} = \begin{pmatrix} 0 & 0 & -1 \\ -1 & 0 & 0 \\ 0 & 1 & 0 \end{pmatrix} \begin{pmatrix} \cos\psi_v & -\sin\psi_v & 0 \\ \sin\psi_v & \cos\psi_v & 0 \\ 0 & 0 & 1 \end{pmatrix} \begin{pmatrix} V_{E_x}\cos\psi_w \\ V_{E_x}\sin\psi_w \\ -V_{E_z} \end{pmatrix} + \begin{pmatrix} 0 \\ 0 \\ r\,\Omega_{swirl} \end{pmatrix} \tag{2.51}$$

where ψ_v is the azimuthal location of the control vane.

Given the exit flow velocity calculated from the inflow solution and the flow swirl velocity, the angle of attack and sideslip angle of a vane (accounting for the vane deflection angle) are given by

$$\alpha_v = tan^{-1}\left(\frac{w_v}{u_v}\right) - \delta_v \tag{2.52}$$

$$\beta_v = sin^{-1}\left(\frac{v_v}{V_v}\right) \tag{2.53}$$

in which δ_v is the vane deflection angle and V_v is the magnitude of the velocity at the vane. The vane deflection is defined to be positive when the trailing edge of the vane is deflected in a clockwise direction as viewed from the top of the rotor, regardless of the rotational direction of the rotor. The Reynolds number of the flow across the vane can be calculated in the same manner as the Reynolds number of the rotor blade segments found earlier using

$$Re_v = \frac{\rho\, V_v\, c_v}{\mu}\ , \tag{2.54}$$

where c_v is the vane chord.

Likewise, table lookups using the angle of attack and Reynolds number of the vane are used to find lift and drag coefficients. The total lift and drag on a vane are found using

$$L_v = C_{l_v}\, q_v\, S_v \tag{2.55}$$

$$D_v = C_{d_v}\, q_v\, S_v\ , \tag{2.56}$$

in which q_v is the dynamic pressure at the vane and S_v is the vane planform area. The vane forces and moments are then calculated and transformed into the rotor hub axis.

2.2.4 Fuselage Drag Model

A function is integrated into the simulation model that calculates the fuselage drag, lift, and side force on the ducted fan aircraft. The function computes equivalent flat plate areas based on the local air velocity and the aircraft's frontal, vertical, and sideward drag areas. Formulas used for drag, lift, and side force equivalent

flat plate areas are given by

$$D_q = S_{f_x} + (S_{f_z} - S_{f_x}) \sin^2\alpha_f + \left(S_{f_y} - S_{f_z} - S_{f_x}\right) \sin^2\beta_f \cos^2\alpha_f \tag{2.57}$$

$$L_q = \frac{1}{2} L_{1f} \sin 2\alpha_f \cos^2\beta_f \tag{2.58}$$

$$Y_q = -\frac{1}{2} Y_{1f} \sin 2\beta_f \cos^2\alpha_f \ , \tag{2.59}$$

where α_f and β_f are the fuselage angle of attack and sideslip angle, S_{f_x}, S_{f_z}, and S_{f_y} are the frontal, vertical, and sideward fuselage drag areas, and L_{1f} and Y_{1f} are the lift and side force slopes, respectively.

A transformation is then performed from wind axes to body axes, given by

$$\boldsymbol{T_{w/f}} = \begin{pmatrix} \cos\beta_f \cos\alpha_f & -\sin\beta_f & -\cos\beta_f \sin\alpha_f \\ \sin\beta_f \cos\alpha_f & \cos\beta_f & -\sin\beta_f \sin\alpha_f \\ \sin\alpha_f & 0 & \cos\alpha_f \end{pmatrix} \tag{2.60}$$

The forces are then scaled by dynamic pressure, q_f, and the moments are resolved about the vehicle c.g., shown in vector form by

$$\boldsymbol{F_f} = \boldsymbol{T_{w/f}} \begin{pmatrix} -D_q \\ Y_q \\ -L_q \end{pmatrix} q_f \tag{2.61}$$

$$\boldsymbol{M_f} = \begin{pmatrix} 0 & h_f & 0 \\ -h_f & 0 & -x_f \\ 0 & x_f & 0 \end{pmatrix} \boldsymbol{F_f} \ , \tag{2.62}$$

in which x_f and h_f are the longitudinal and vertical positions, respectively, of the fuselage aerodynamic center.

The fuselage drag model was a key element in the correlation with the 29-inch UAV wind tunnel data, especially axial and normal forces. The correlation studies are presented in Chapter 4.

2.2.5 Total Forces and Moments

Because of the ducted rotor configuration, the thrust produced by the duct itself must be accounted for when determining the total system thrust. The thrust generated by the duct and the corresponding total thrust equations are given below.

$$T_D = k_{aug}\, T_R \tag{2.63}$$

$$T = T_D + T_R \tag{2.64}$$

The momentum drag experienced by the ducted rotor system is dependent on the inflow model used. The equations for momentum drag using Inflow Model 1 and Inflow Model 2 are presented in Equation 2.65 and Equation 2.66, respectively.

$$D_m = \rho\, A_D\, V_R\, k_\chi\, V_{inplane} \tag{2.65}$$

$$D_m = \rho\, A_D\, V_R \left(\cos\alpha - \cos\left(\alpha + k_{\chi_\infty}\left(\frac{\pi}{2} - \alpha\right)\right)\right) V \tag{2.66}$$

The total forces and moments in the rotor hub system, represented in vector form containing the x-, y-, and z-components of such forces and moments, are given as

$$\mathbf{F_h} = \begin{pmatrix} X_R - D_m\, \cos\psi_w + X_v \\ Y_R - D_m\, \sin\psi_w + Y_v \\ -T + Z_v \end{pmatrix} \tag{2.67}$$

$$\mathbf{M_h} = \begin{pmatrix} L_R - T_D\, x_{T_D}\, \sin\psi_w + L_v \\ M_R + T_D\, x_{T_D}\, \cos\psi_w + M_v \\ \pm Q_R + N_v \end{pmatrix}, \tag{2.68}$$

in which Q_R is positive for a counterclockwise rotating rotor. The duct thrust offset, x_{T_D}, is defined in Section 2.3.2.

2.3 Duct Pitching Moment Modeling

One of the most challenging aspects of properly modeling a ducted fan system is accurately modeling the strong adverse pitching moment experienced in forward flight. For a given vehicle design and flight condition, the duct pitching moment

may be a function of airspeed, angle of attack, advance ratio, and inflow velocity. The pitching moment may also be unpredictable in certain flight conditions, especially when flow separation occurs over the lip of the duct, further adding to the complexity of the model.

There are essentially two common ways of modeling the duct pitching moment in forward flight. The two methods, one a function of the ram drag and one a function of the duct thrust, are described in detail in Section 2.3.1 and Section 2.3.2, respectively.

2.3.1 Ram Drag Pitching Moment Model

A popular method of modeling the pitching moment generated by a ducted rotor in forward flight is to assume that the momentum drag, or ram drag, can be resolved at a center of pressure at some height above the plane of the rotor. The vertical offset of the ram drag center of pressure produces the nose-up pitching moment on the ducted rotor in forward flight. The height above the rotor at which the ram drag center of pressure is located is denoted by z_{D_m} in Figure 2.3. The vertical offset is assumed to be a function of angle of attack and forward speed, but it may also be affected by other factors, such as duct lip separation.

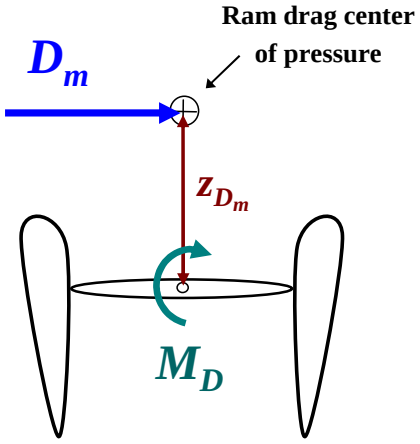

Figure 2.3. Ram Drag Pitching Moment Model.

Modeling the pitching moment using the momentum drag offset method is presented in several papers [5, 17, 18]. In each case, empirical data were obtained to formulate the model.

2.3.2 Duct Thrust Pitching Moment Model

An alternate way of modeling the pitching moment produced by the ducted fan is to assume that the thrust generated by the duct itself in edgewise flight is offset from the centerline of the duct. The duct thrust offset is caused by asymmetric lift due to differences in velocity between the leading and aft portions of the duct. This longitudinal offset of the duct thrust, denoted by x_{T_D} in Figure 2.4, creates the pitching moment in forward flight. This is thought to be a more meaningful way of representing the effect of pitching moment because the moment is proportional to the duct thrust, which is a result of the duct design. A particular duct in a ducted fan system may not be generating thrust based on its design, but there will be momentum drag produced from the turning of the flow from the freestream direction to the duct's axis direction. Therefore, representing pitching moment as a function of duct thrust more closely ties the ducted fan design with its performance.

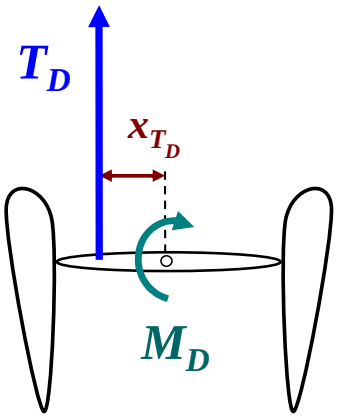

Figure 2.4. Duct Thrust Pitching Moment Model.

A schematic is presented in Figure 2.5 that shows the changes in duct thrust as the ducted fan transitions from low-speed edgewise flight to high-speed axial flight. Empirical evidence suggests that the longitudinal offset of duct thrust increases linearly with an increase in advance ratio until the point at which separation on the lip of the duct occurs. At this point, the duct thrust rapidly moves to the aft portion of the duct, and a nose-down pitching moment is experienced. As the duct pitches more toward axial flight, the separated flow region reattaches and the duct thrust moves back to the centerline of the duct. Thus the pitching moment is reduced to zero.

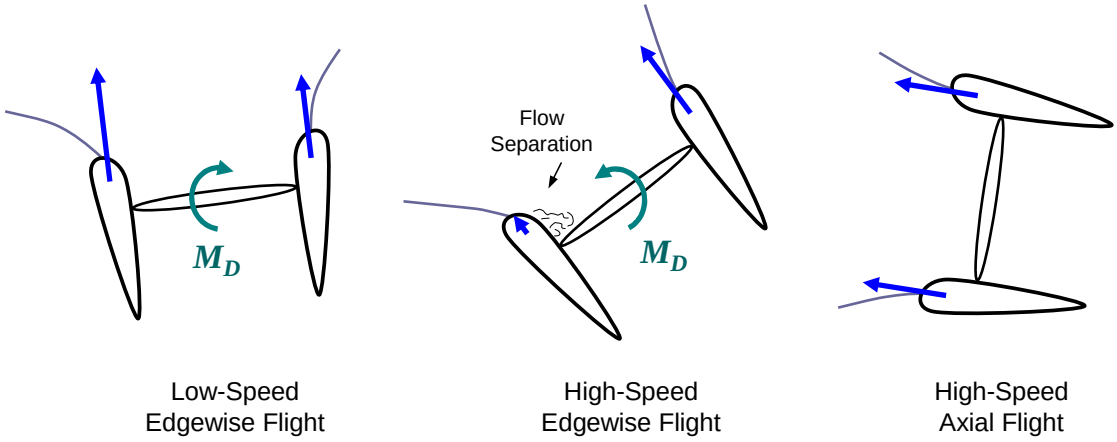

Figure 2.5. Variation in Duct Thrust in Transition from Edgewise to Axial Flight.

It is theorized that the longitudinal offset of duct thrust not only varies with advance ratio, but also with inflow velocity. Example cases include a ducted rotor operating at a low flight speed but at a high thrust level, or a ducted rotor operating at a high flight speed but at a low thrust level. The ducted rotors may experience similar pitching moments in both cases, regardless of the difference in advance ratio, because of the effect inflow has on the turning of the flow and the pitching moment produced.

2.3.3 Pitching Moment Model Formulation

Wind tunnel data and other analytical results were used to formulate and refine the duct pitching moment model for use in the generic ducted fan simulation model. The pitching moment model provides the duct thrust offset normalized by the rotor radius, written x_{T_D}/R, for a given airspeed. The pitching moment model is implemented solely as a function of airspeed for simplicity; however a more advanced model as a function of airspeed, angle of attack, and inflow velocity may be considered in future versions of the simulation model. A plot of the current values of duct thrust offset normalized by rotor radius versus total airspeed is presented in Figure 2.6.

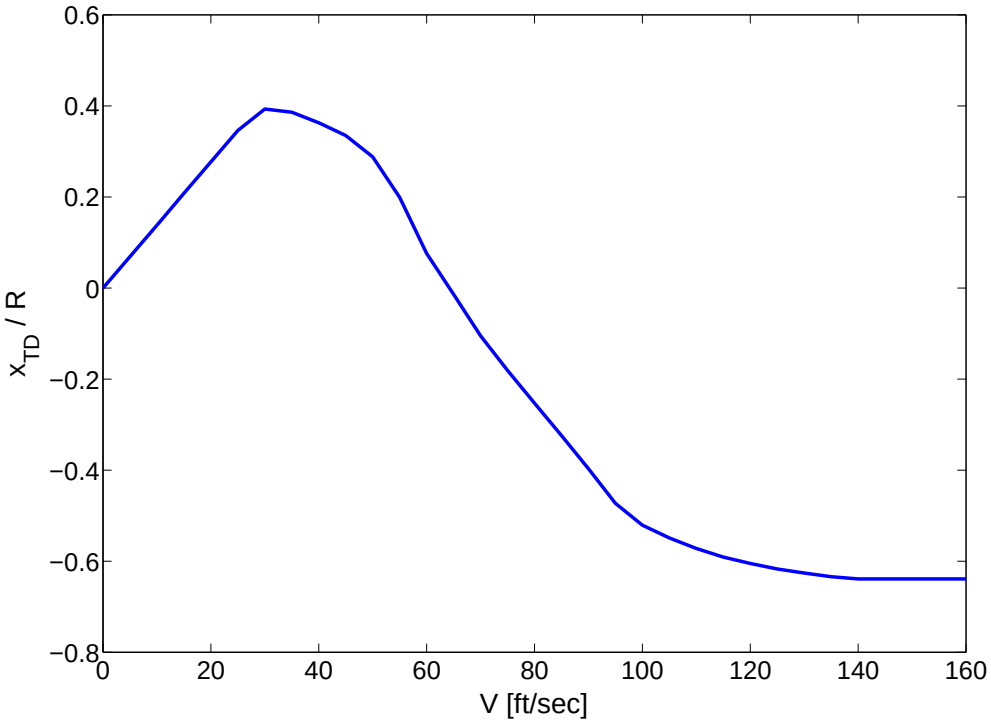

Figure 2.6. Normalized Duct Thrust Offset vs Airspeed for Duct Pitching Moment Model.

2.4 MATLAB Implementation

2.4.1 Code Vectorization

Vectorized code implemented in MATLAB was used for the simulation environment. Code vectorization is a method in which vector and matrix multiplication is utilized in place of conventional loops to form arrays. MATLAB, in essence, is a matrix processing language that utilizes very efficient built-in operations for data contained in arrays [19]. MATLAB's run speed, however, is slow when data is accessed through interpreted loops. Although loop-based code is often more intuitive to develop and to understand, vectorization can significantly increase the efficiency and performance of a program at runtime. It is in this respect that vectorized code was developed in order to run the simulation in real time.

2.4.2 State Space Representation

A state space representation [20] is used in the generic ducted fan simulation model. The state equations of the dynamic system can be expressed as

$$\dot{x}(t) = f(x_1(t), x_2(t), \ldots, x_n(t), u_1(t), u_2(t), \ldots, u_m(t)) \ , \tag{2.69}$$

where x_1 through x_n are the state variables and u_1 through u_m are the input variables. Similarly, the output variables of the system, which are functions of the input variables and the state variables, can be represented as

$$y(t) = g(x_1(t), x_2(t), \ldots, x_n(t), u_1(t), u_2(t), \ldots, u_m(t)) \ . \tag{2.70}$$

Together, the state equations and the output equations form the dynamic equations of the system.

To easily express the dynamic equations in a simulation environment, the dynamic equations are represented in vector-matrix form. The state vector, $\mathbf{x}(t)$, is a vector that contains the state variables of the simulation model. The particular states used in the generic ducted fan simulation model are given by the following aircraft state vector:

$$\mathbf{x}(t) = [\, u \ \ v \ \ w \ \ p \ \ q \ \ r \ \ \phi \ \ \theta \ \ \psi \ \ x \ \ y \ \ z \ \ v_{i_0} \,]^T \tag{2.71}$$

A first-order dynamic model is used to calculate inflow, which requires v_{i_0} to be a state variable. Therefore, the quasi-steady inflow (solved iteratively in Equation 2.12 when using Inflow Model 1 and Equation 2.20 when using Inflow Model 2) is passed through a first-order filter,

$$\dot{v}_{i_0} = -\frac{1}{\tau} v_{i_0} + \frac{1}{\tau} v_{i_{qs}} \ , \tag{2.72}$$

in which τ is the inflow time constant. Note that induced velocity, v_{i_0}, is currently the only rotor state variable. Future versions of the simulation model may include the three state Pitt-Peters inflow, which includes v_{i_0}, $v_{i_{1s}}$ and $v_{i_{1c}}$ [21].

The input vector, $\mathbf{u}(t)$, contains the inputs to the dynamic system. In the generic simulation model, the inputs to the system are the pilot's control inputs.

The pilot control input vector is given by

$$\mathbf{u}(t) = [\ \delta_{lat}\ \ \delta_{lon}\ \ \delta_{col}\ \ \delta_{ped}\ ]^T\ . \tag{2.73}$$

Additionally, the output vector, $\mathbf{y}(t)$, contains the outputs of the system. The output vector may be used for monitoring or data collection purposes, and can contain any variables used in the simulation model. Using the state, input, and output vectors, the state equations can be written as

$$\dot{\mathbf{x}}(t) = \mathbf{f}[\mathbf{x}(t), \mathbf{u}(t)]\ . \tag{2.74}$$

Likewise, the output equations are given by

$$\mathbf{y}(t) = \mathbf{g}[\mathbf{x}(t), \mathbf{u}(t)]\ . \tag{2.75}$$

The state equations are then integrated with the aircraft equations of motion for use in a maneuvering flight application.

2.5 Physical Description of Test Aircraft

2.5.1 Small Single Ducted Fan Configuration

The first aircraft model is a small, single ducted fan design with rigid rotor blades and four control vanes placed radially at the exit of the duct. The single duct model was configured to match wind tunnel data of a 29-inch ducted fan UAV (Unmanned Aerial Vehicle). A schematic and picture of the 29-inch UAV are presented in Figure 2.7.

Physical parameters similar to those of the 29-inch UAV were implemented in the generic single ducted fan model, and empirical correction factors, such as the thrust augmentation and flow turning factors, were tuned to match the 29-inch UAV data set. The physical properties and empirical factors that most closely correlated with the 29-inch UAV data are provided in Table 2.1. Results of the correlation studies can be found in Chapter 4.

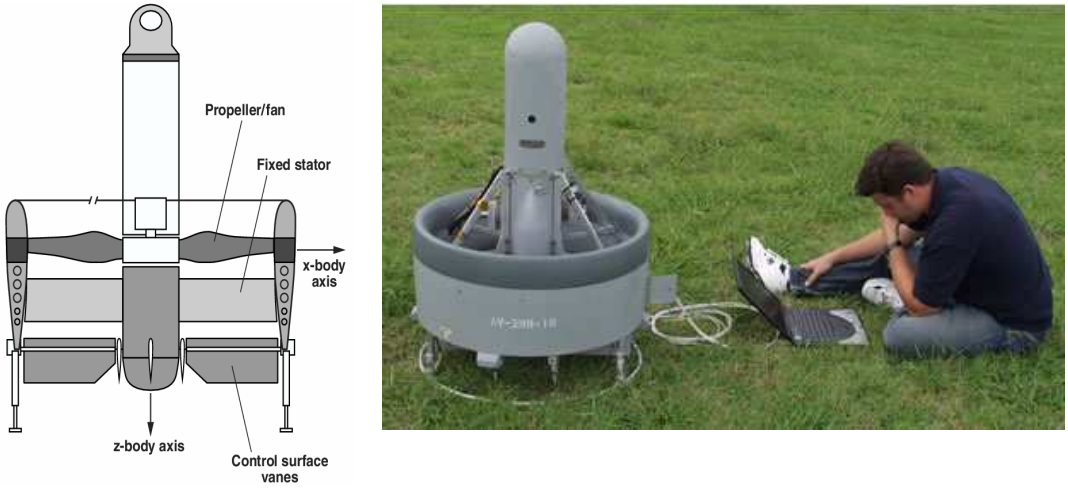

Figure 2.7. 29-Inch Ducted Fan UAV [12, 11].

Property	Value	Unit
W	68.8	lbs
Ω	575.9 / 628.3	rad/sec
θ_0	14.81	deg
θ_{tw}	-8.0	deg
R	1.208	ft
c_b	0.2	ft
r_0	$0.2\,R$	ft
S_v	0.78	ft^2
N_b	4	–
B	0.98	–
k_{aug}	0.3	–
k_{χ_R}	0.5	–
k_{χ_∞}	0.9	–

Table 2.1. Generic Single Ducted Fan Configuration Properties.

2.5.2 Large Tandem Ducted Fan Configuration

The second model is a large tandem ducted fan configuration with four control vanes placed in the exit flow of each duct as well. Rigid rotors, specifically a counterclockwise rotating front rotor and a clockwise rotating aft rotor, are modeled. Modeling of a full-size aircraft was chosen because of the current attention devoted to this type of vehicle, such as the Urban Aeronautics X-Hawk, and its apparent usefulness in modern aviation.

The X-Hawk, as seen in Figure 2.8, is a large VTOL vehicle designed for operations in complex urban environments, such as delivering medical personnel in order to reduce response time in the event of an emergency [1]. The X-Hawk has a very elaborate fuselage design, an array of many control vanes located at the inlets and outlets of the ducts, and a venting system incorporated into the leading portion of the fuselage to reduce flow turning effects.

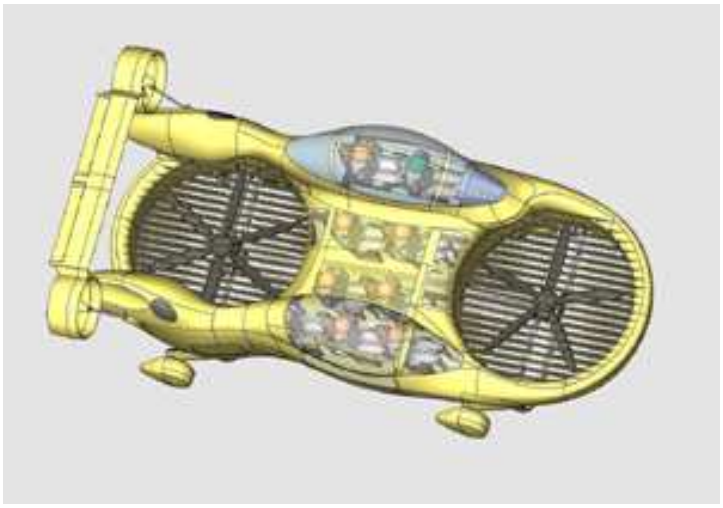

Figure 2.8. Urban Aeronautics X-Hawk.

Note that the vehicle configuration used in the generic simulation model is greatly simplified. A schematic of the aircraft configuration used in the generic tandem ducted fan simulation model can be seen in Figure 2.9. Several physical properties of the tandem ducted fan aircraft configuration are shown in Table 2.2.

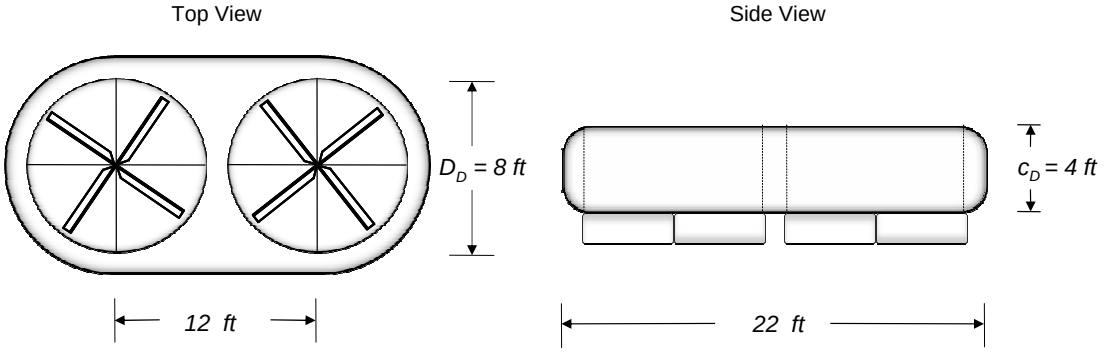

Figure 2.9. Tandem Ducted Fan Aircraft Schematic.

Property	Value	Unit
W	4000	lbs
Ω	188.5	rad/sec
θ_{tw}	-10.0	deg
R	4.0	ft
c_b	0.6	ft
r_0	0.5	ft
S_v	6.0	ft^2
N_b	6	$-$
B	0.98	$-$

Table 2.2. Generic Tandem Ducted Fan Configuration Properties.

Chapter 3

Model Development Using FLIGHTLAB Software

FLIGHTLAB was used to model a complete tandem ducted fan aircraft and to compare and validate the generic ducted fan model. The same physical properties and empirical factors used in the generic ducted fan MATLAB model were implemented along with an identical control system. FLIGHTLAB proved to be an efficient and accurate tool in the development of a detailed tandem ducted fan model, in which the results were used to further develop and refine the generic ducted fan model.

3.1 FLIGHTLAB Overview

FLIGHTLAB is a flight vehicle modeling and analysis software application developed by Advanced Rotorcraft Technology, Inc. This software enables users to produce models interactively from a library of modeling components, modify physical properties and dimensions, and interconnect them in a customizable architecture. The simulation language used in FLIGHTLAB is an operating environment that supports vector/matrix operations and uses syntax very similar to MATLAB. Graphical user interfaces are implemented in this software, including a hierarchical data tree structure in which the user enters and modifies various components of the aircraft. A sample screenshot of the data tree structure used in the FLIGHTLAB Model Editor (FLME) can be seen in Figure 3.1.

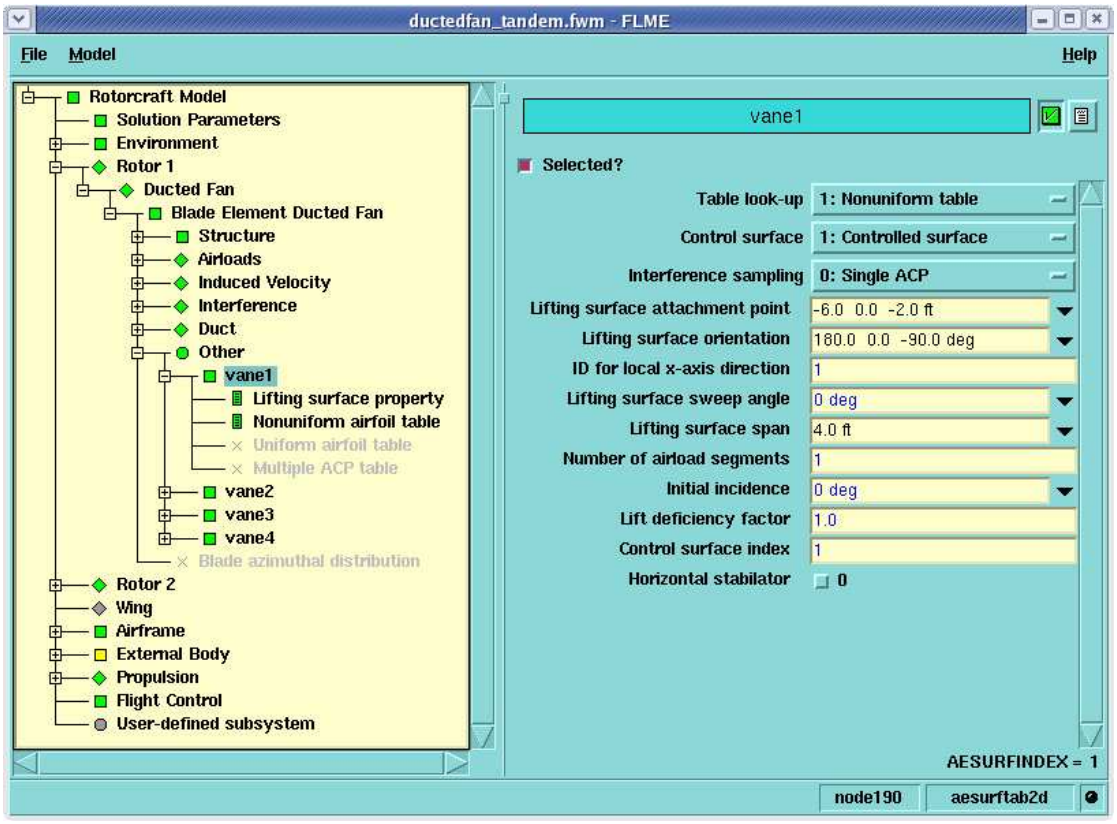

Figure 3.1. Screenshot of FLME with Data Tree Structure.

3.2 Developing the FLIGHTLAB Model

Modifications to a built-in ducted fan model were implemented in order to create the tandem ducted fan system. Although the supplied ducted fan model was primarily intended to be used for anti-torque applications on conventional helicopters, the theory used in the development of the ducted fan model is not limited to such applications. Therefore, the supplied model was also applicable to VTOL configurations in which a ducted fan is the primary source of lift.

3.2.1 Solution Parameters

Basic solution parameter values used for Newton-Raphson method were chosen. The parameters include integration time step, convergence tolerance, and maximum number of iterations. The integration time was selected to be in azimuth steps, and the option to use a Hilber-Hughes-Taylor (HHT) solver was not needed

because a small time step was selected.

3.2.2 Atmospheric Environment

The standard atmospheric environment model was used. This includes no turbulence modeling, a standard table of temperature gradient as a function of altitude, as well as standard, hot, tropical, polar and cold day atmospheric tables that are included with the software package. The standard day atmospheric environment was used exclusively in the analysis in order to easily and accurately compare results with other data sources.

3.2.3 Ducted Fan Model

A blade element rotor model with rigid blades, equal annulus area, and uniform blade distribution was implemented. The blade element model calculates the fan blade airloads with respect to the local angle of attack and Mach number of each individual blade segment. Specifically, the calculation of blade airloads is performed analytically in two loops. The inner loop determines the blade segment airloads as if the segment was a two-dimensional airfoil with a three-dimensional fan wake model used to formulate the blade effects. Blade segment airloads are computed with respect to the local angle of attack, Mach number, and dynamic pressure, which allows for a nonlinear airloads model with stall effect. The outer loop of the blade element analysis determines the fan wake using an enhanced finite state dynamic wake model that includes the effects of the duct [14].

A ring vortex duct model was used to represent the duct's effect on the flowfield and the duct's interaction with the rotor . The ring vortex duct model is included in the standard model editor, and it is derived from a potential flow solution which allows for a range of flight conditions from hover to forward flight [14]. The duct wake model includes trailing vortices only, and the duct interference affects the mean induced velocity on the rotor.

3.2.4 Control Vane Model

Exit control vanes are modeled using all-moving control surfaces with a NACA 0012 airfoil as the cross section. A common nonuniform lookup table including the angle of attack and Reynolds number at the vane is used to find the forces and moments generated by the control vane.

Eight control vanes, four for each ducted rotor, are included in the model. The indices of the exit control vanes are shown in Figure 3.2. Care was taken to insure that each vane was attached at the proper location and was orientated correctly using Euler rotations. The sequence of Euler rotations is through ψ, θ, and ϕ, and the local vane coordinate frame is defined as follows: y-axis pointing to the leading edge of the vane, z-axis pointing to the positive camber side of the vane, and x-axis defined by the right hand rule.

The attachment point of the control vane is in terms of fuselage (positive aft), buttline (positive left), and waterline (positive up) stations relative to the vehicle c.g. The attachment point and Euler rotation for each vane are shown in Table 3.1. The vanes are designated as controllable surfaces in FLME, which allows the vanes to be utilized within the Control System Graphical Editor (CSGE). The control mixing function for the vanes can be found in Section 5.1.

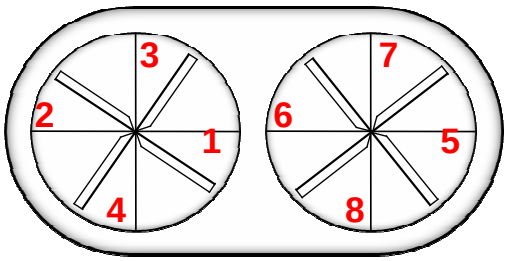

Figure 3.2. Exit Control Vane Indices.

3.2.5 Additional Modeling Components

Other modeling components include a rigid fuselage, in which the total vehicle mass and moments of inertia are entered, and an ideal engine for the propulsion system. An ideal engine maintains a constant rotational speed and has no limit on the power output. All other variables included within FLME not mentioned previously were simply set to the default values.

Vane Index	Attachment Point [ft]	Euler Rotation [deg]
1	-6 0 -2	180 0 -90
2	”	0 0 -90
3	”	90 0 -90
4	”	-90 0 -90
5	6 0 -2	180 0 -90
6	”	0 0 -90
7	”	90 0 -90
8	”	-90 0 -90

Table 3.1. Exit Control Vane Orientations.

3.3 Control Step Response Tests

Control step responses were performed in order to assure that the control system was properly configured. A step input was applied to a given control and the vehicle response was monitored to verify the expected behavior. Specifically, the aircraft was trimmed in hover, a step input was applied, and the vehicle accelerations, rates, and attitudes were analyzed. If the control system is set up correctly, an acceleration, with a corresponding rate, will be prominent in only one body axis.

Four individual step input tests were conducted, one in each of the primary control axes. The results of the step input responses can be found in Section A.2.2. Note that a large step input magnitude was applied in order to exaggerate the vehicle response, and that the results obtained shortly after the step input are unrealistic.

Chapter 4

Model Correlation Studies

Correlation studies were performed on results generated from the generic ducted fan simulation model, results obtained using FLIGHTLAB, and experimental wind tunnel data of the 29-inch ducted fan UAV. The comparison of results was crucial in the validation and refinement of the generic ducted fan simulation model.

4.1 Data Sources

4.1.1 29-Inch Ducted Fan UAV Wind Tunnel Data

Wind tunnel data sets of a 29-inch diameter ducted fan UAV were obtained courtesy of NASA Ames Research Center. The UAV was tested primarily for axial flight, so most of the useful data are for angles of attack near the axial flight region. Results for pure edgewise flow are valid at low flight speeds; however the data points for high flight speeds at angles of attack near edgewise flight are simply copies of data points taken at the axial flight region. Therefore, the copied data are not included in the comparison.

The model was tested at rotor speeds of 5500 RPM and 6000 RPM. This allowed for a correlation of static thrust for a given rotor speed. Additional plots of the UAV wind tunnel data can be found in Section A.1.1.

4.1.2 Steady-State FLIGHTLAB Results

Velocity sweeps were conducted on a single ducted fan model in which the solution reached steady-state for each given flight speed. The steady-state analysis allowed data of the forces, moments, and aircraft states to be collected as if the model was in a wind tunnel. In the steady-state "wind tunnel" mode, the controls are frozen and the model is fixed at a given angle of attack as forward flight speed is increased. More thorough steady-state sweeps included variations in rotor speed as well.

4.1.3 Generic Ducted Fan Simulation Results

The generic simulation model was used to generate results using the small single ducted fan configuration. Physical parameters and empirical correction factors used in the configuration can be found in Table 2.1. Physical characteristics similar to the 29-inch UAV were implemented in the generic ducted fan simulation model in order to generate results that match well with the experimental data; however, unknown variables, such as thrust augmentation factor, k_{aug}, and flow turning factors, k_{χ_R} and k_{χ_∞}, had to be inferred.

The matching of axial force data occurred first, which involved choosing values for the empirical correction factors and then adjusting the collective rotor pitch, θ_0, to match the experimental data in static conditions (at zero airspeed). Iterations were then performed until constant parameter values were found that yielded the best correlation over the range of angles of attack and airspeeds.

Inflow Model 1, as presented in Section 2.1.1, and Inflow Model 2, which is presented in Section 2.1.2, are both included in the correlation of results. Identical model parameters, however, are used in each case. Note that, in general, the use of Inflow Model 2 yields results that are slightly closer to the experimental data points. Also note that in some conditions, particularly at large negative angles of attack and at high airspeeds, the solution does not converge when Inflow Model 1 is implemented.

4.2 Correlation of Pitching Moment Coefficient

Figures 4.1 through 4.14 are of pitching moment coefficient versus airspeed ratio. Because of the differences in model sizes, layouts, and configurations applicable in the generic simulation model, the non-dimensional pitching moment coefficient, C_M, is used to compare results even though the correlation studies were performed using similar aircraft configurations. Applying the non-dimensional pitching moment coefficient allows for future correlations to be performed using the presented results. The definition of pitching moment coefficient used in the analysis is

$$C_M = \frac{M}{\rho A R \left(\Omega R\right)^2} \ . \tag{4.1}$$

Pitching moment coefficient is plotted versus airspeed ratio, which is given by

$$\mu' = \frac{V_\infty}{\Omega R} = \frac{\mu}{\cos \alpha} \ . \tag{4.2}$$

Airspeed ratio is defined as the freestream velocity divided by the rotor tip speed. Airspeed ratio can also be written as the advance ratio, μ, divided by the cosine of the angle of attack of the duct. Because of the wide range of possible flight conditions of ducted fan aircraft, the airspeed ratio is used to analyze the data instead of the conventional advance ratio in order to easily compare data of different angles of attack on the same plot [17].

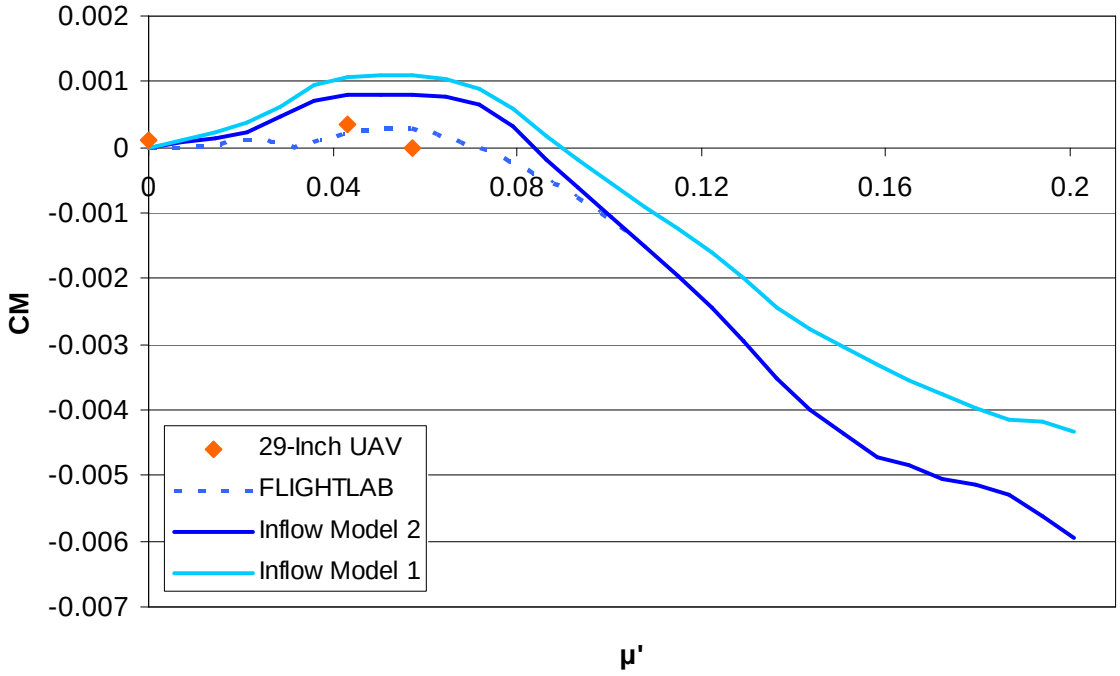

Figure 4.1. Pitching Moment Coeff. vs Airspeed Ratio ($\Omega = 5500$ RPM, $\alpha = 0°$).

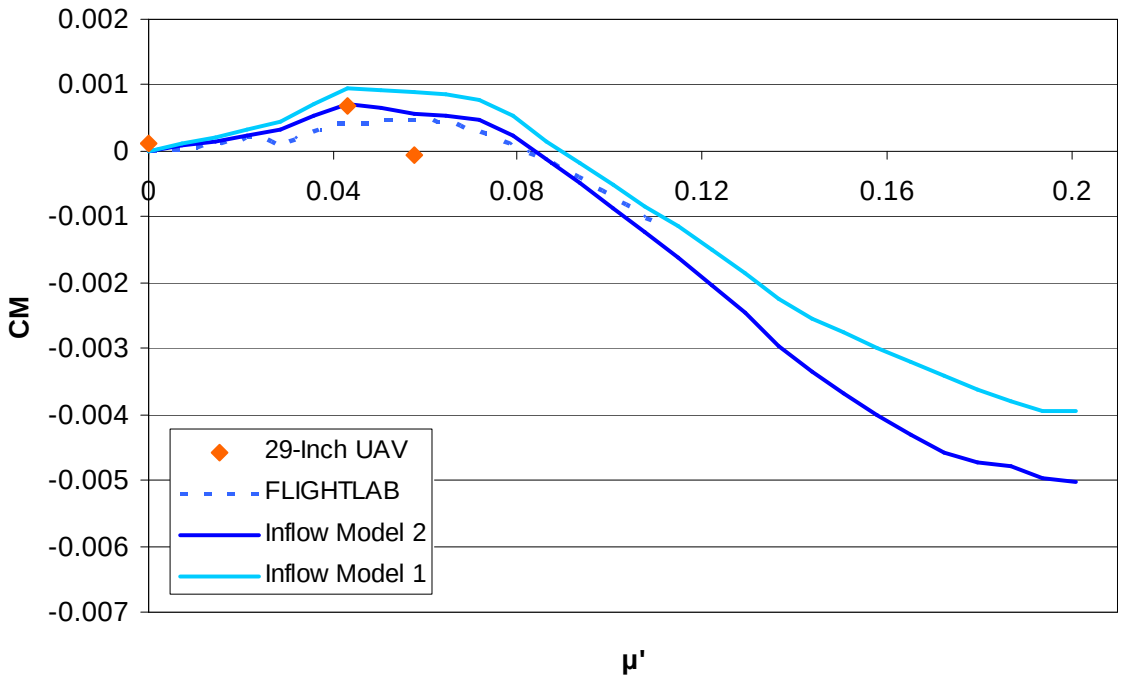

Figure 4.2. Pitching Moment Coeff. vs Airspeed Ratio ($\Omega = 5500$ RPM, $\alpha = -10°$).

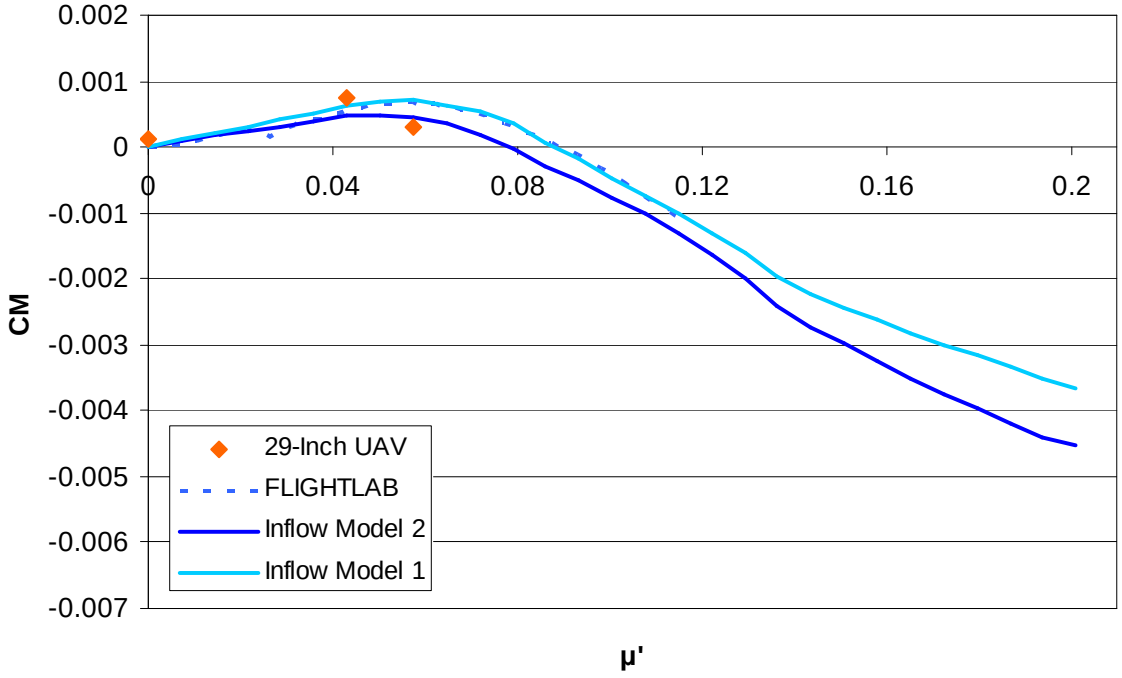

Figure 4.3. Pitching Moment Coeff. vs Airspeed Ratio ($\Omega = 5500$ RPM, $\alpha = -20°$).

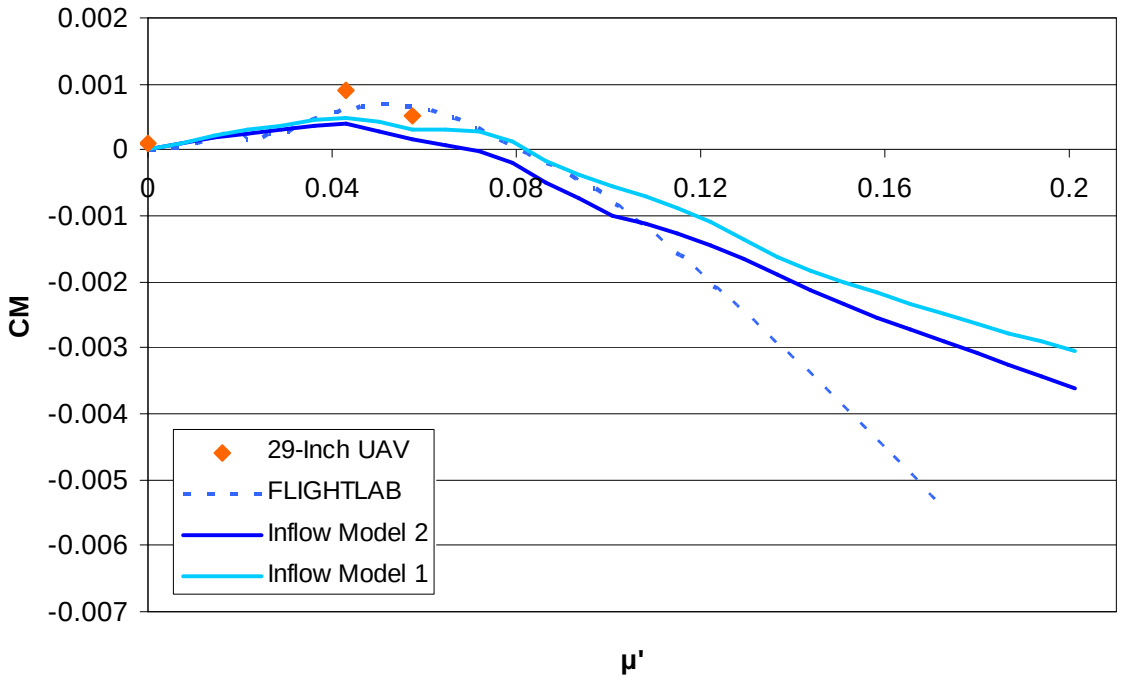

Figure 4.4. Pitching Moment Coeff. vs Airspeed Ratio ($\Omega = 5500$ RPM, $\alpha = -30°$).

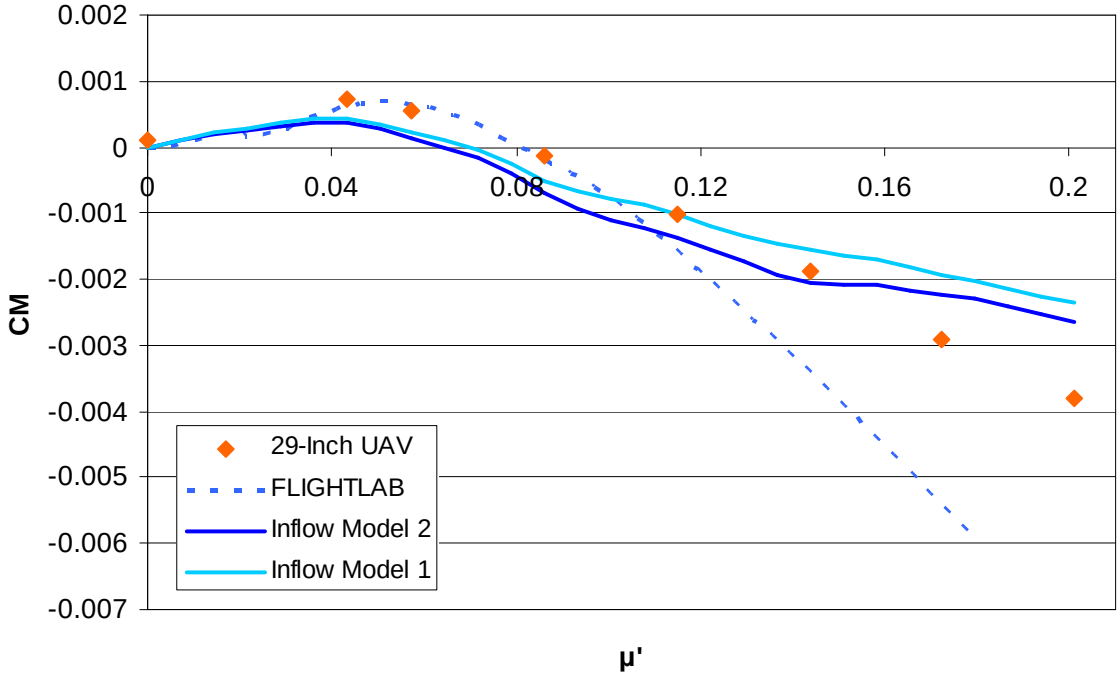

Figure 4.5. Pitching Moment Coeff. vs Airspeed Ratio ($\Omega = 5500$ RPM, $\alpha = -40°$).

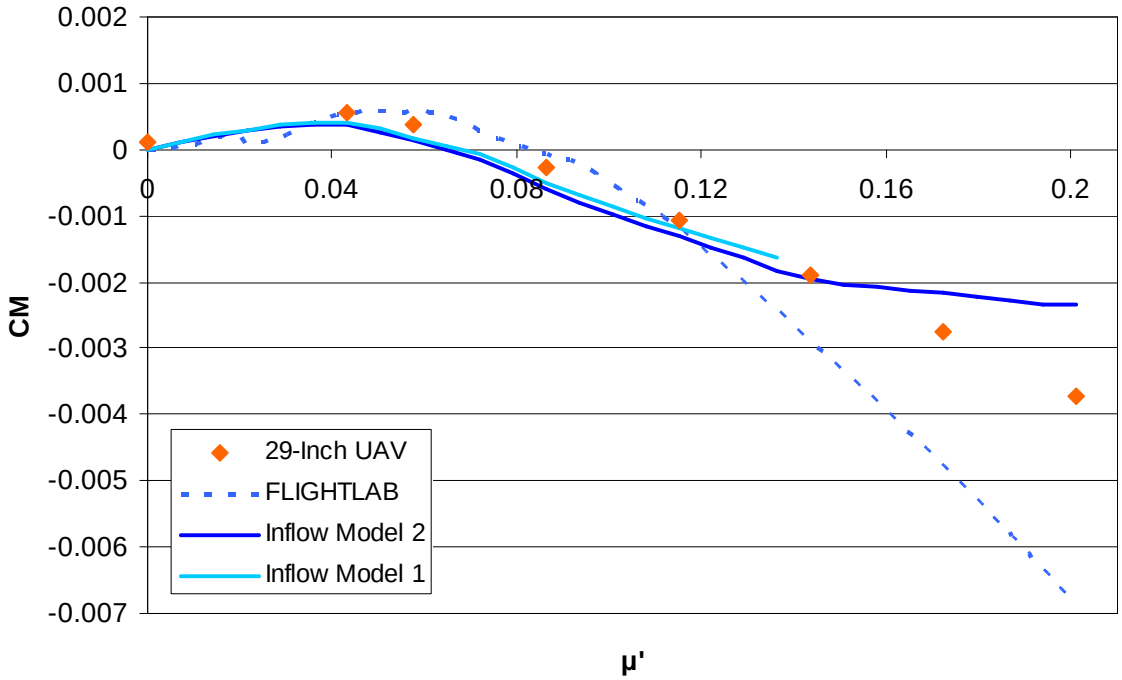

Figure 4.6. Pitching Moment Coeff. vs Airspeed Ratio ($\Omega = 5500$ RPM, $\alpha = -50°$).

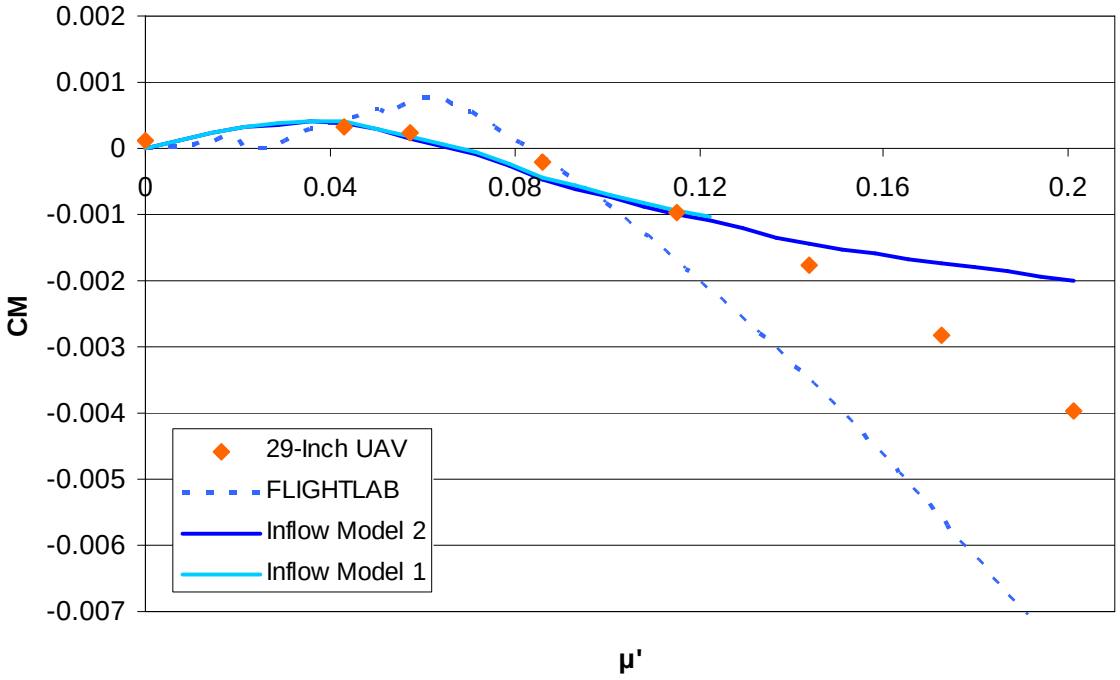

Figure 4.7. Pitching Moment Coeff. vs Airspeed Ratio ($\Omega = 5500$ RPM, $\alpha = -60°$).

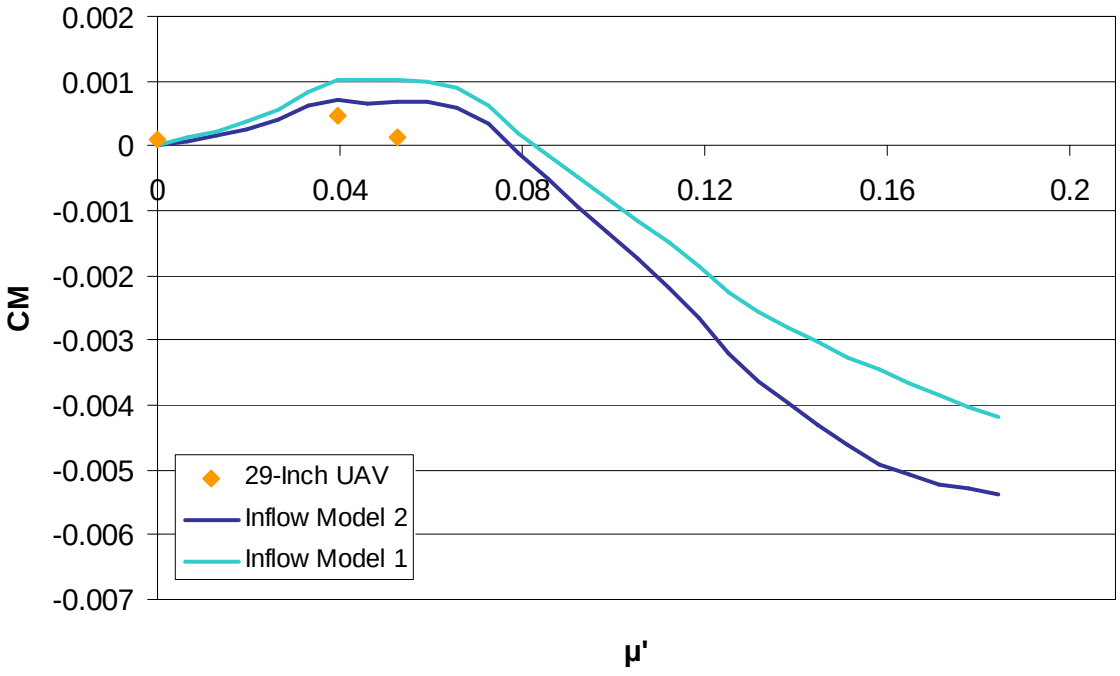

Figure 4.8. Pitching Moment Coeff. vs Airspeed Ratio ($\Omega = 6000$ RPM, $\alpha = 0°$).

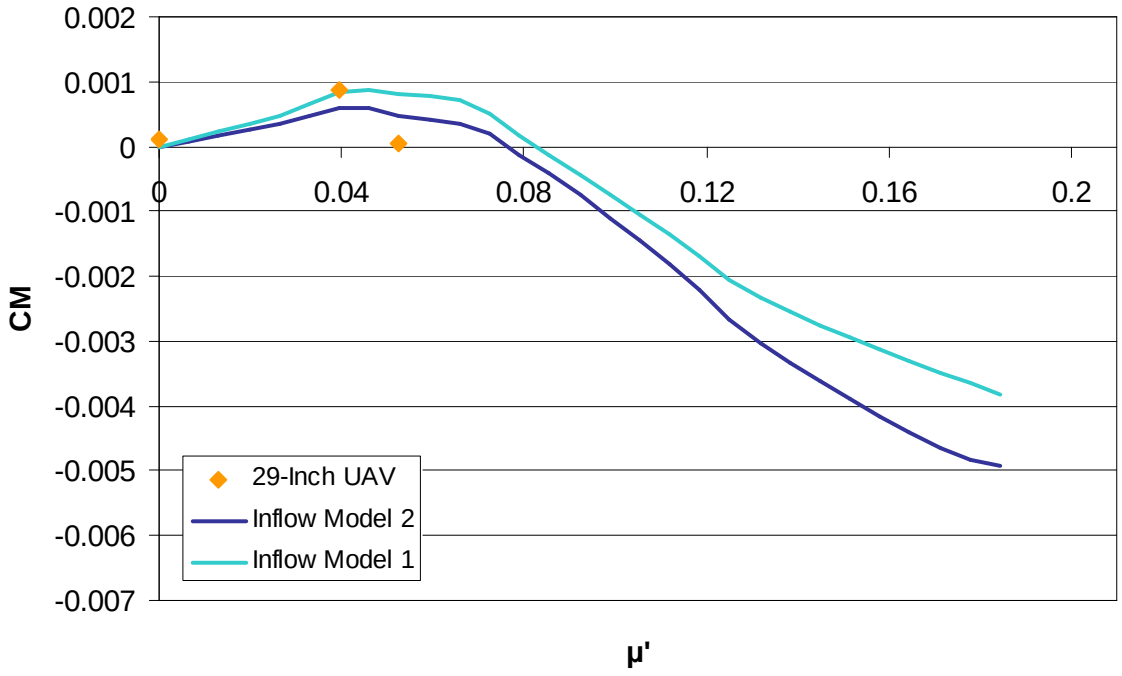

Figure 4.9. Pitching Moment Coeff. vs Airspeed Ratio ($\Omega = 6000$ RPM, $\alpha = -10°$).

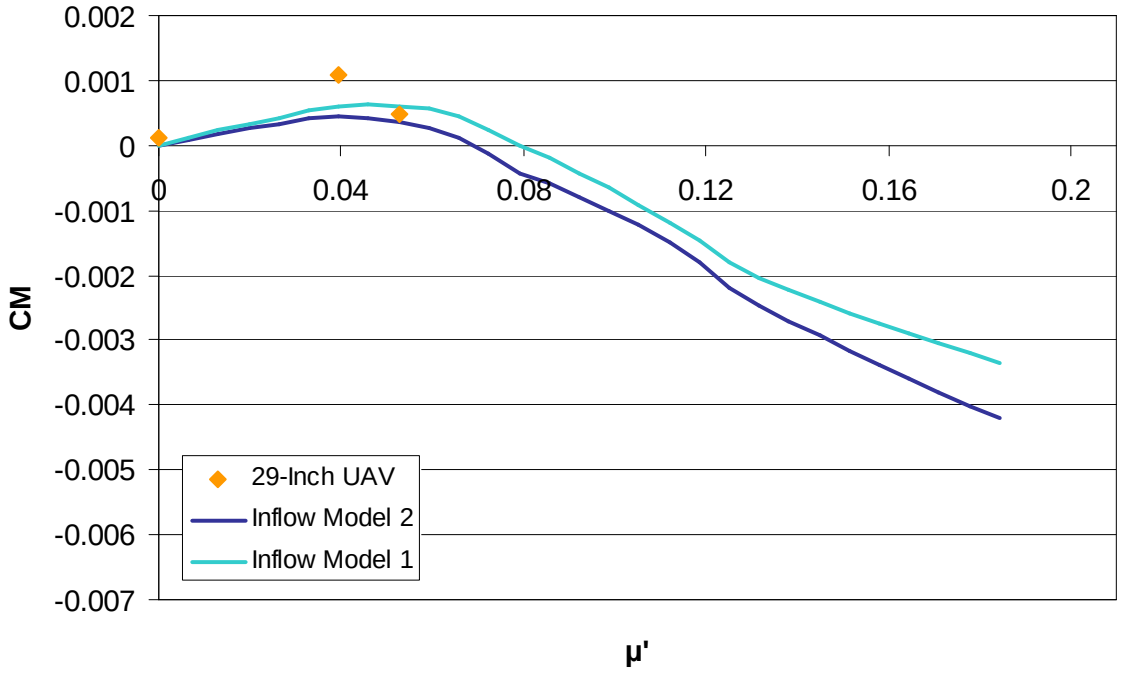

Figure 4.10. Pitching Moment Coeff. vs Airspeed Ratio ($\Omega = 6000$ RPM, $\alpha = -20°$).

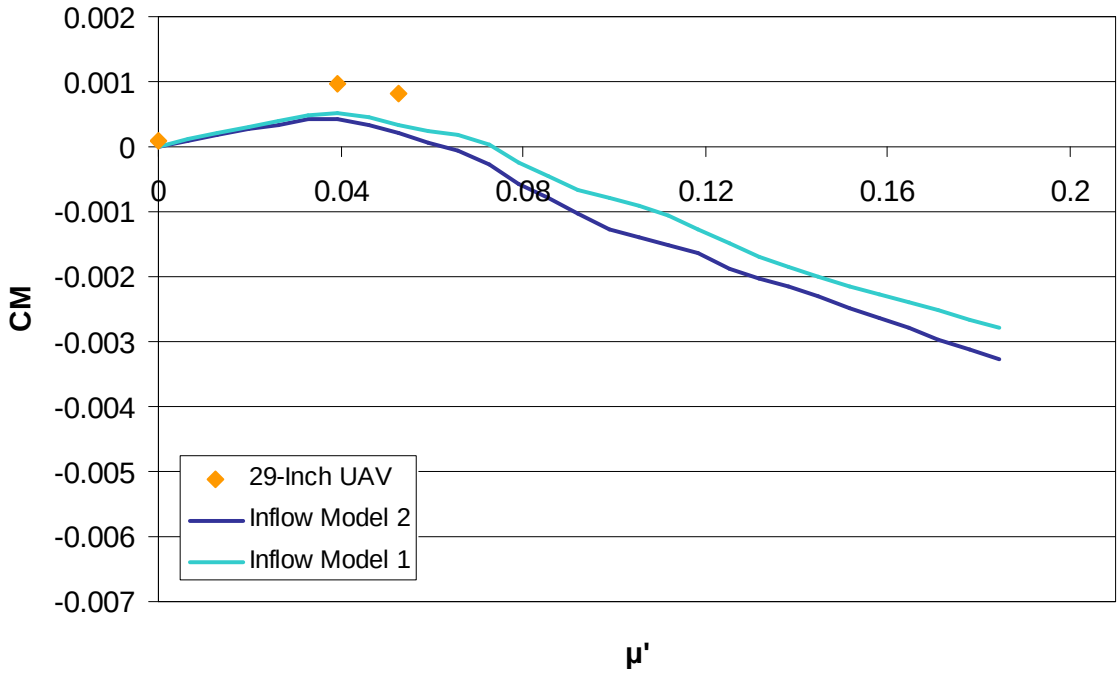

Figure 4.11. Pitching Moment Coeff. vs Airspeed Ratio ($\Omega = 6000$ RPM, $\alpha = -30°$).

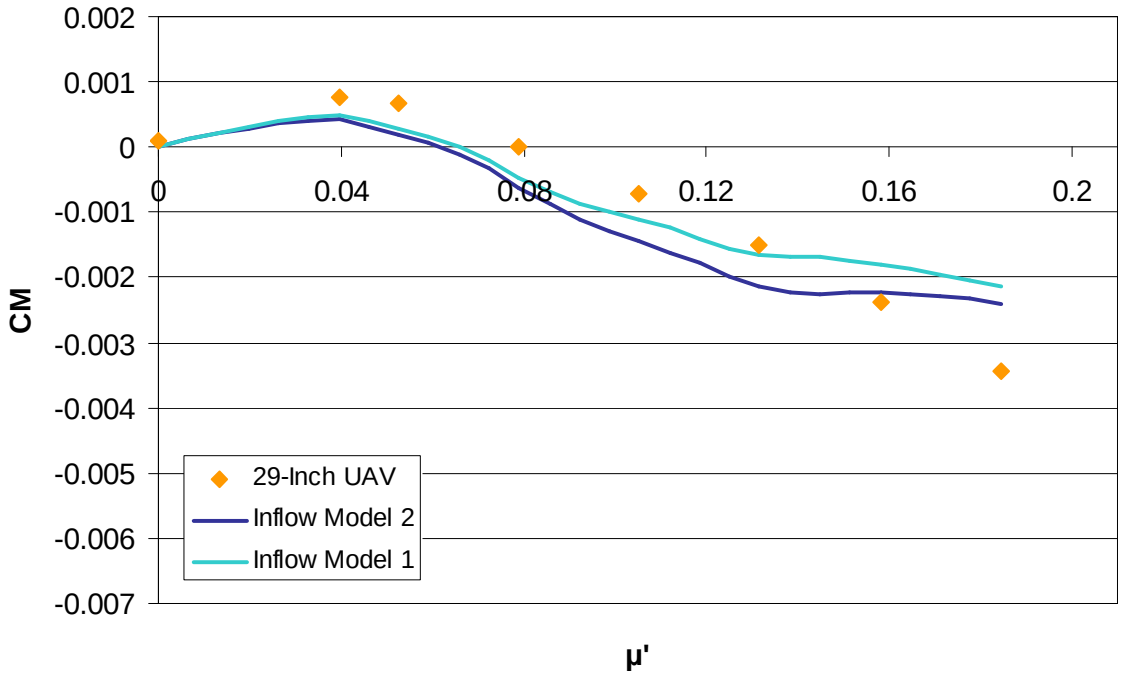

Figure 4.12. Pitching Moment Coeff. vs Airspeed Ratio ($\Omega = 6000$ RPM, $\alpha = -40°$).

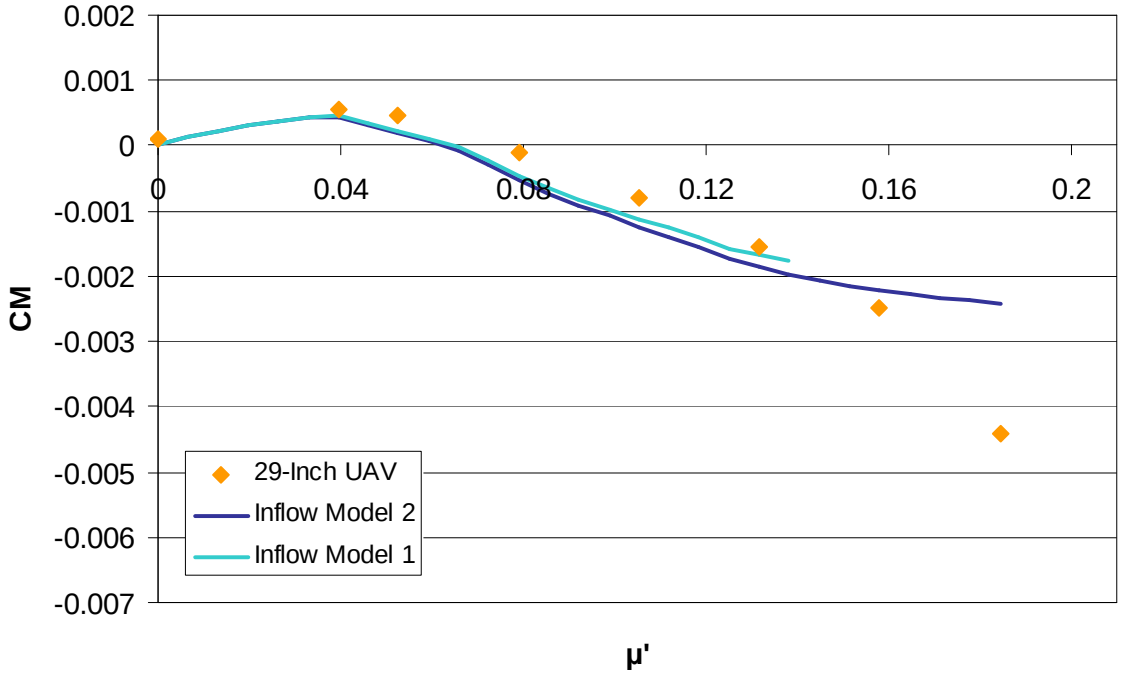

Figure 4.13. Pitching Moment Coeff. vs Airspeed Ratio ($\Omega = 6000$ RPM, $\alpha = -50°$).

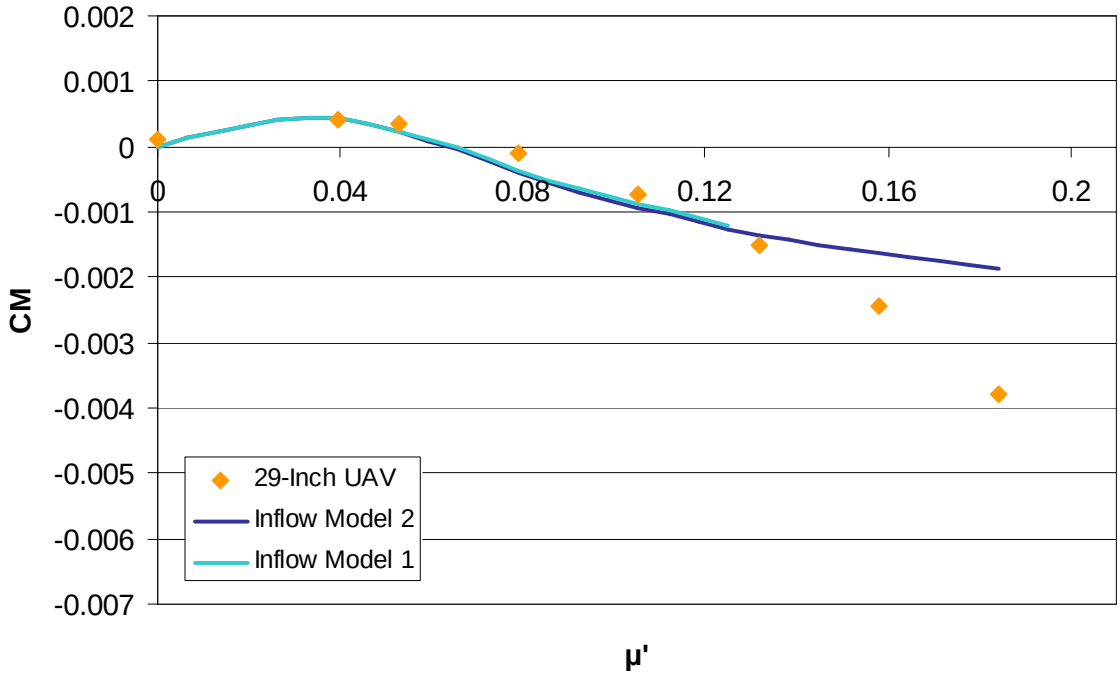

Figure 4.14. Pitching Moment Coeff. vs Airspeed Ratio ($\Omega = 6000$ RPM, $\alpha = -60°$).

The results generated using the generic ducted fan simulation model correlate well with the supplied UAV wind tunnel data, especially at larger nose-down angles of attack. This is important for the validation of the generic simulation model because inflow, pitching moment, and fuselage drag are all prominent factors at near-axial flight regimes. Further tuning of the fuselage drag model may improve the correlation at high airspeeds, at which point the drag forces are more significant.

4.3 Correlation of Axial Force

Figures 4.15 through 4.28 present results of axial force versus airspeed. Axial force, which is the force in the direction of the vertical axis of the ducted fan, was correlated by tuning the generic model to match the 29-inch UAV wind tunnel data in static conditions. Note that negative values of F_z represent a force in the upward vertical direction because the vertical (z-axis) is orientated positive down. A negative axial force is considered to be total thrust when the duct is operating at zero angle of attack.

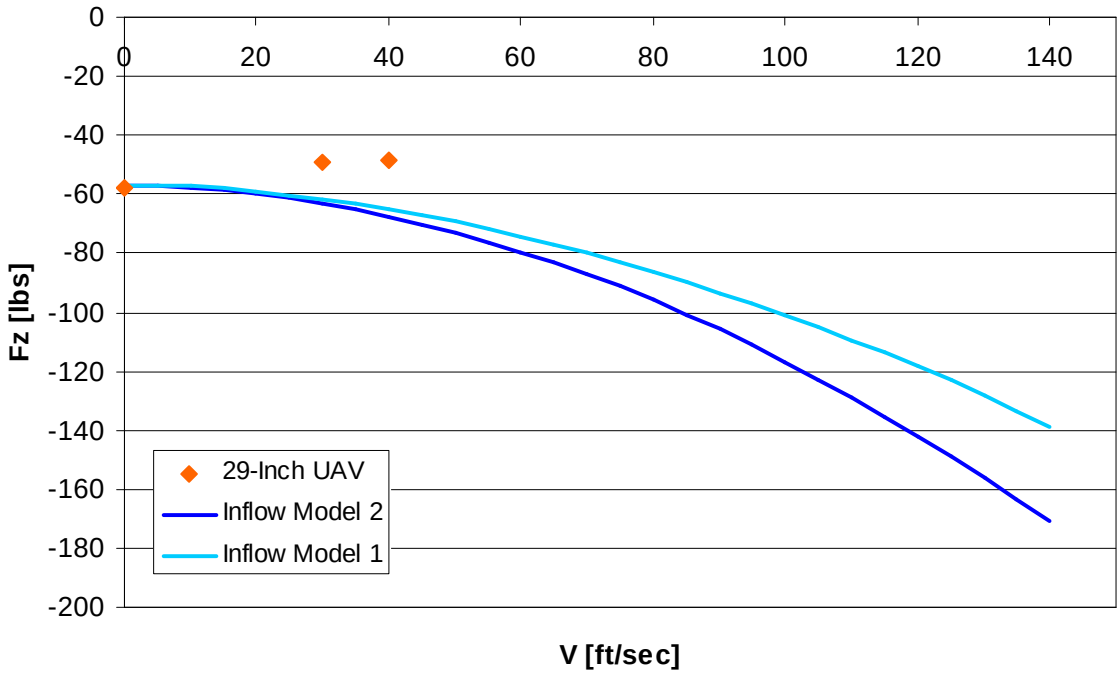

Figure 4.15. Axial Force vs Airspeed ($\Omega = 5500$ RPM, $\alpha = 0°$).

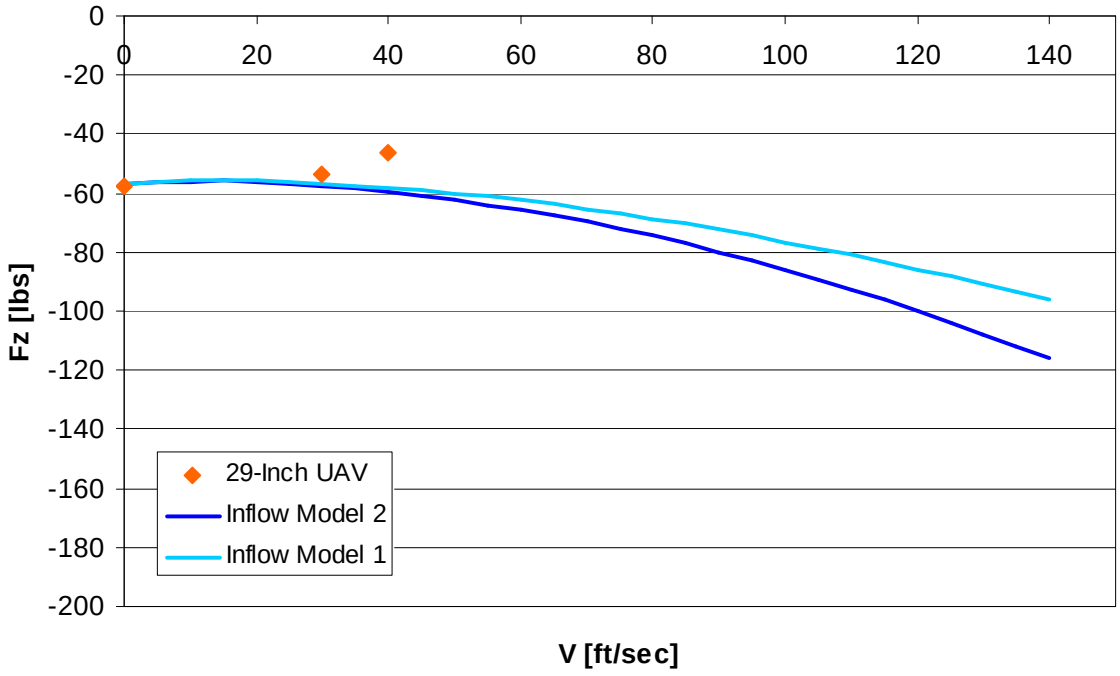

Figure 4.16. Axial Force vs Airspeed ($\Omega = 5500$ RPM, $\alpha = -10°$).

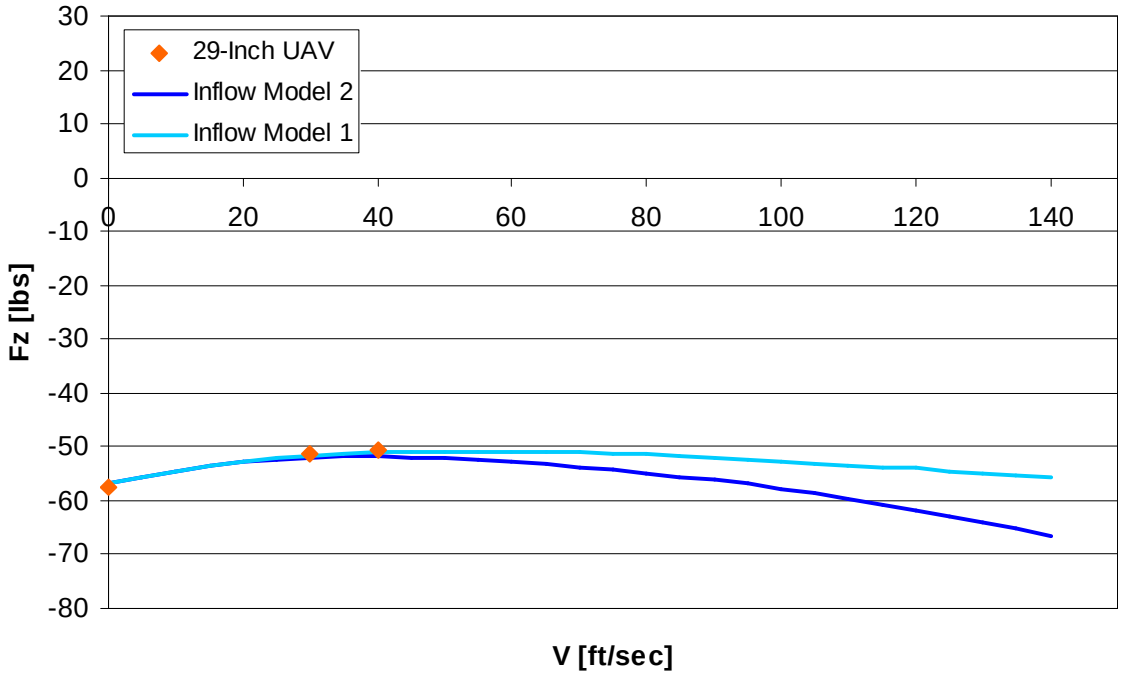

Figure 4.17. Axial Force vs Airspeed ($\Omega = 5500$ RPM, $\alpha = -20°$).

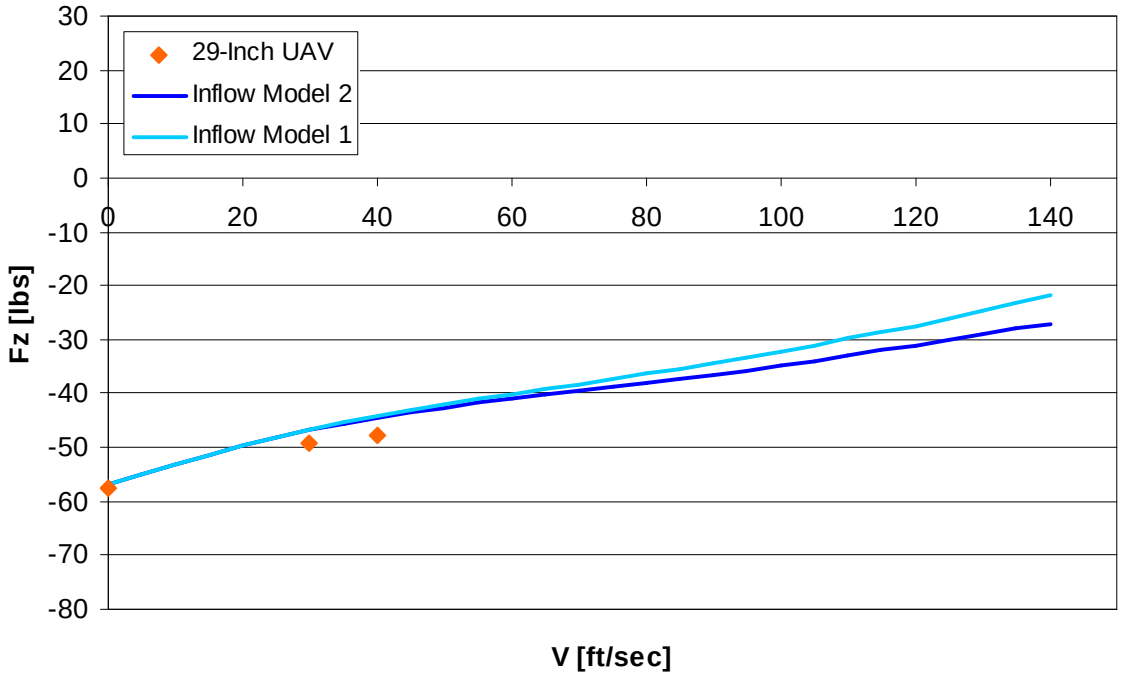

Figure 4.18. Axial Force vs Airspeed ($\Omega = 5500$ RPM, $\alpha = -30°$).

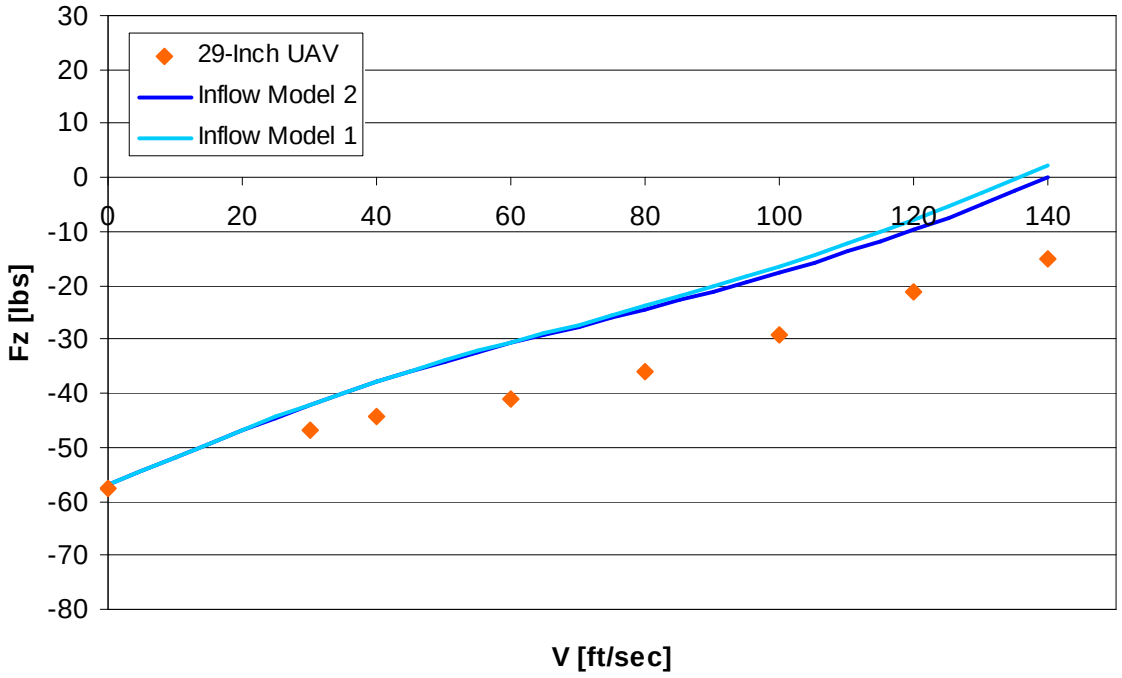

Figure 4.19. Axial Force vs Airspeed ($\Omega = 5500$ RPM, $\alpha = -40°$).

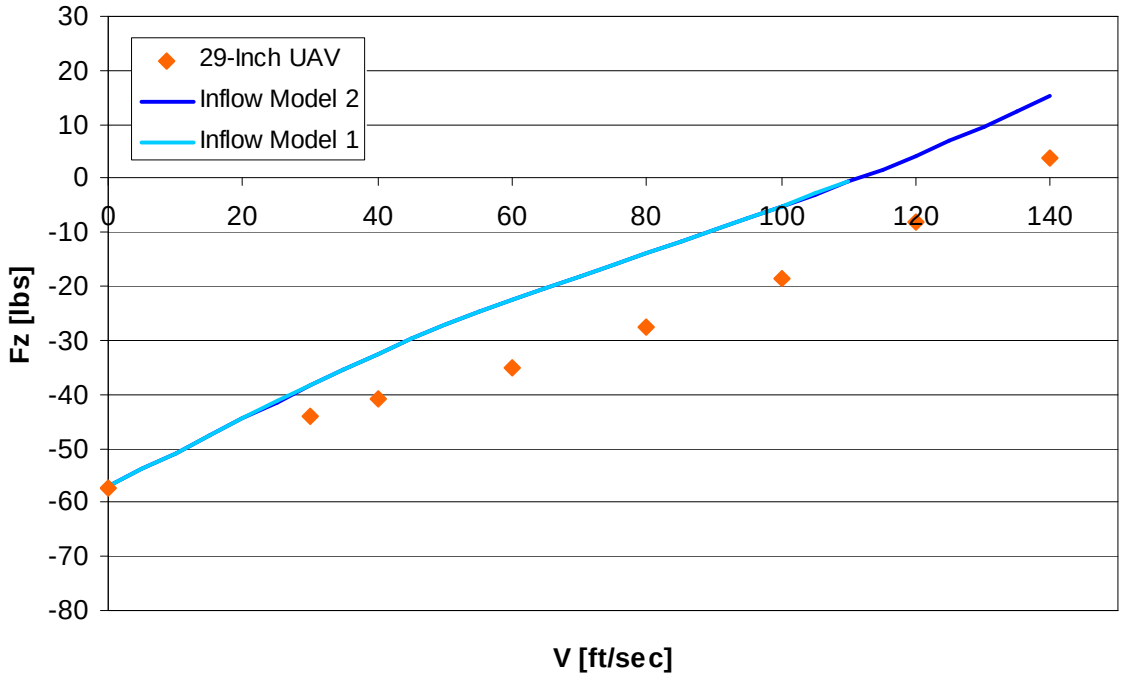

Figure 4.20. Axial Force vs Airspeed ($\Omega = 5500$ RPM, $\alpha = -50°$).

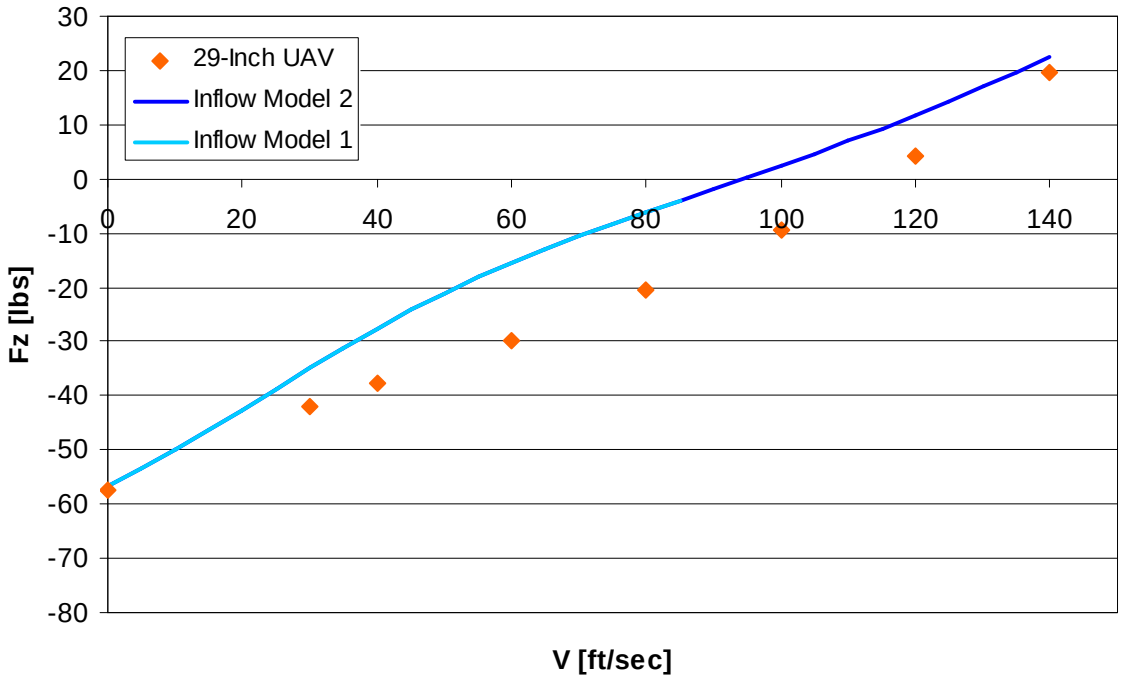

Figure 4.21. Axial Force vs Airspeed ($\Omega = 5500$ RPM, $\alpha = -60°$).

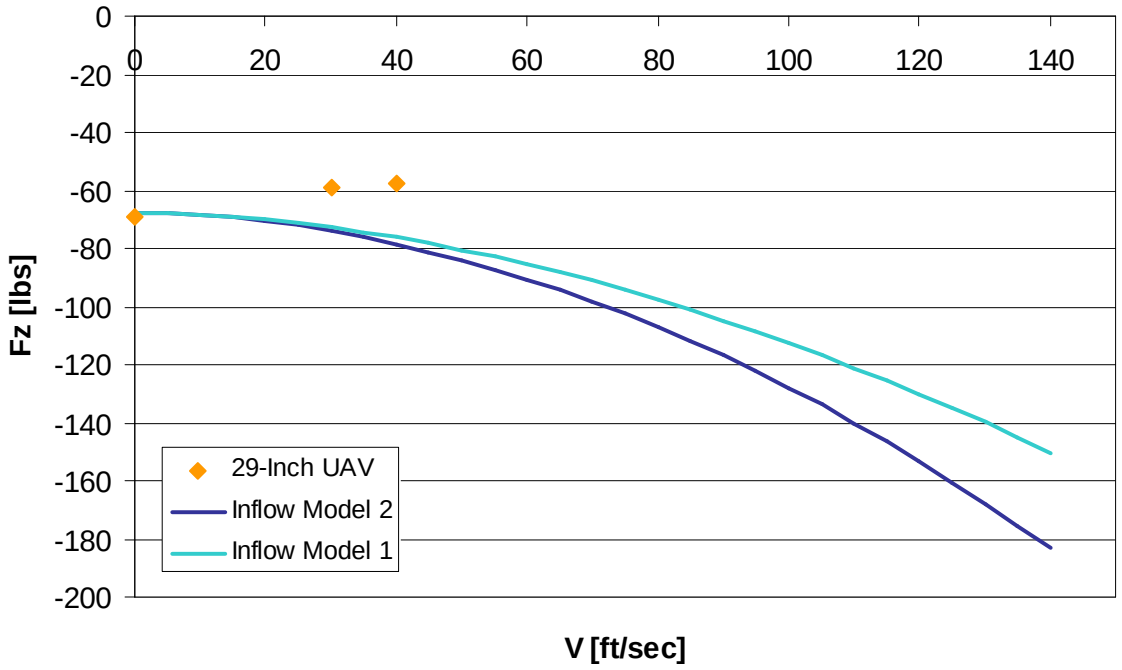

Figure 4.22. Axial Force vs Airspeed ($\Omega = 6000$ RPM, $\alpha = 0°$).

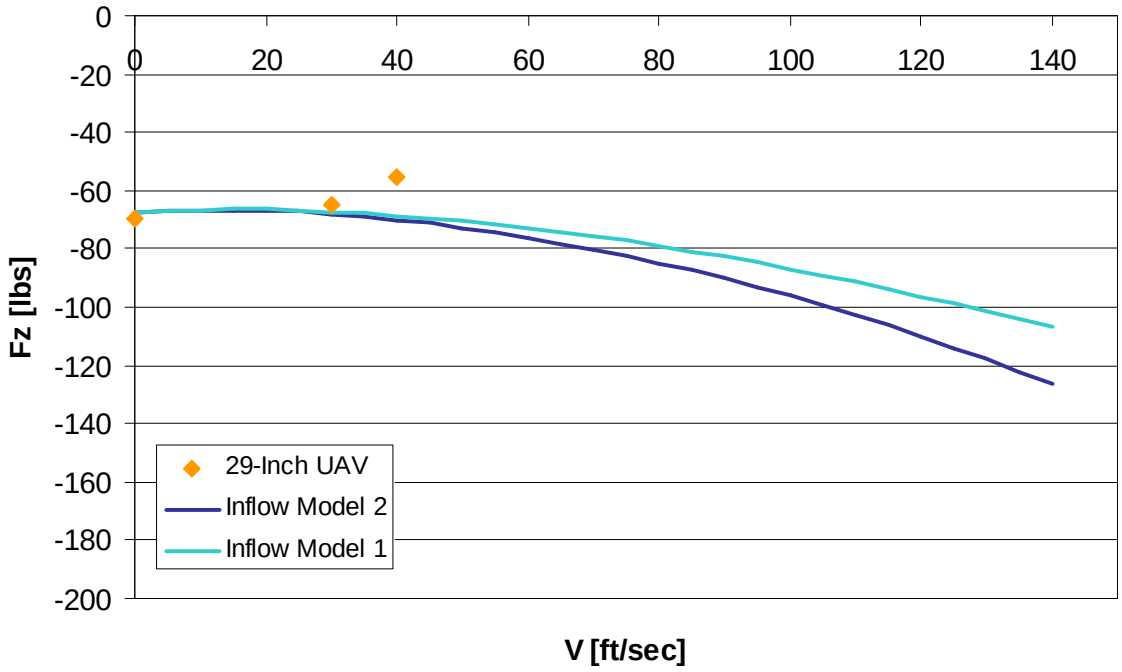

Figure 4.23. Axial Force vs Airspeed ($\Omega = 6000$ RPM, $\alpha = -10°$).

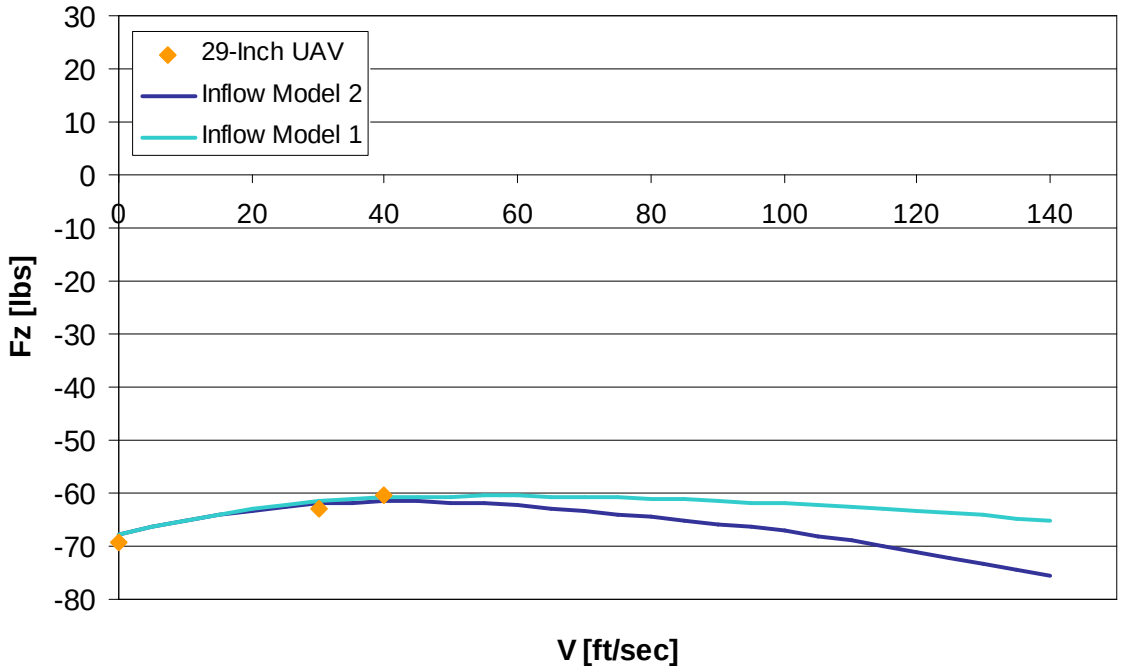

Figure 4.24. Axial Force vs Airspeed ($\Omega = 6000$ RPM, $\alpha = -20°$).

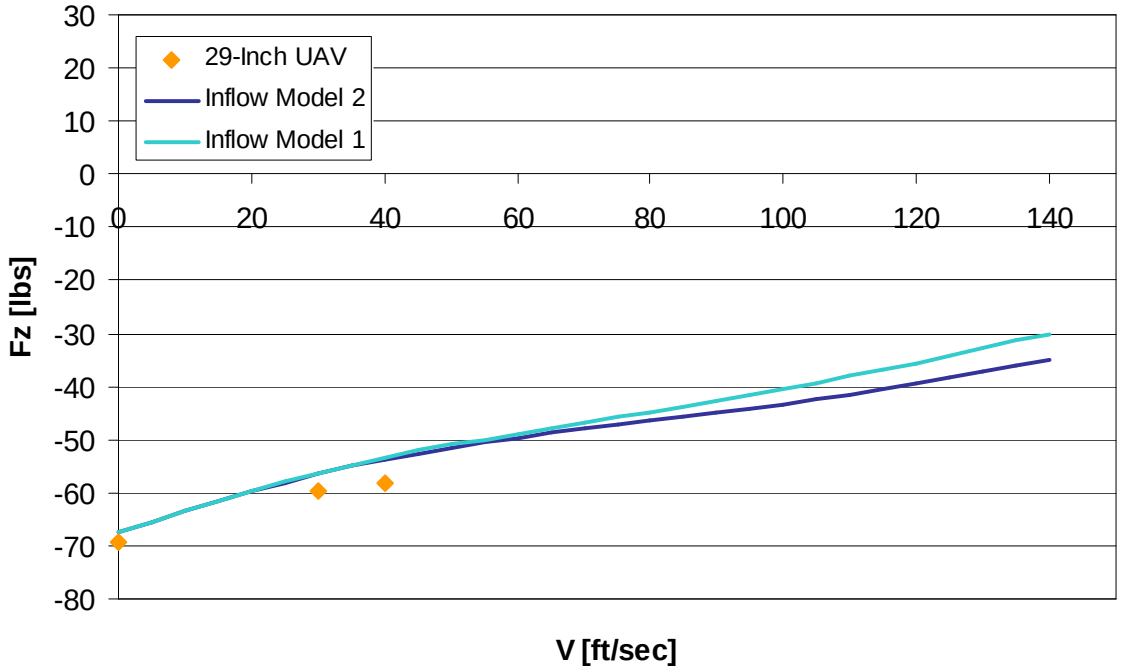

Figure 4.25. Axial Force vs Airspeed ($\Omega = 6000$ RPM, $\alpha = -30°$).

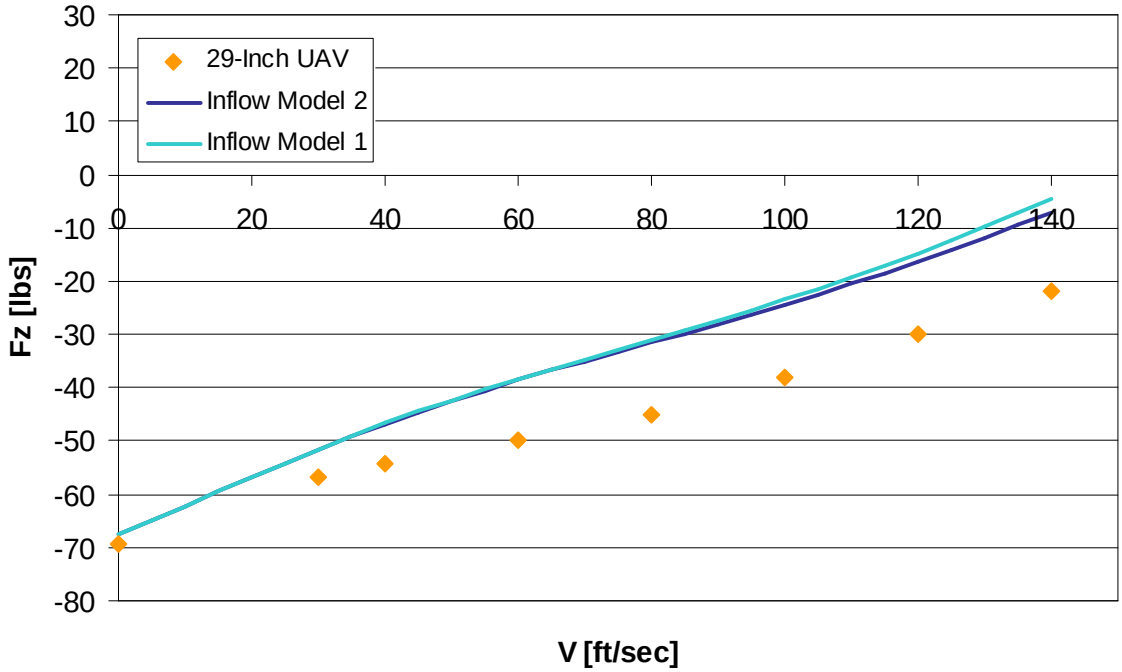

Figure 4.26. Axial Force vs Airspeed ($\Omega = 6000$ RPM, $\alpha = -40°$).

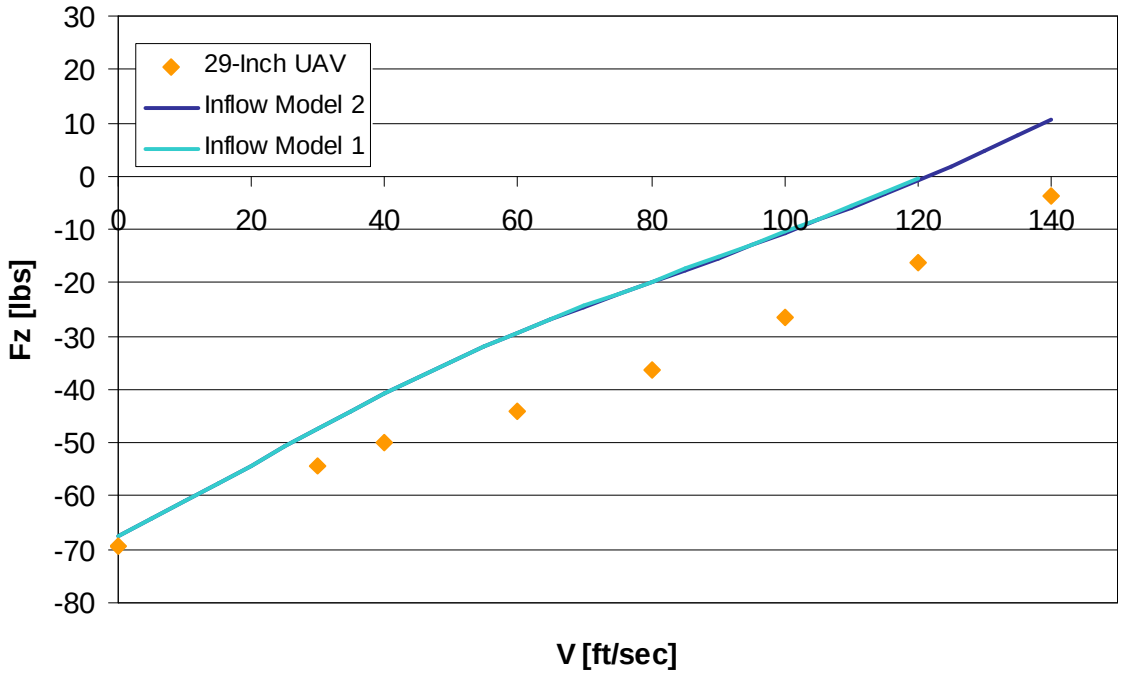

Figure 4.27. Axial Force vs Airspeed ($\Omega = 6000$ RPM, $\alpha = -50°$).

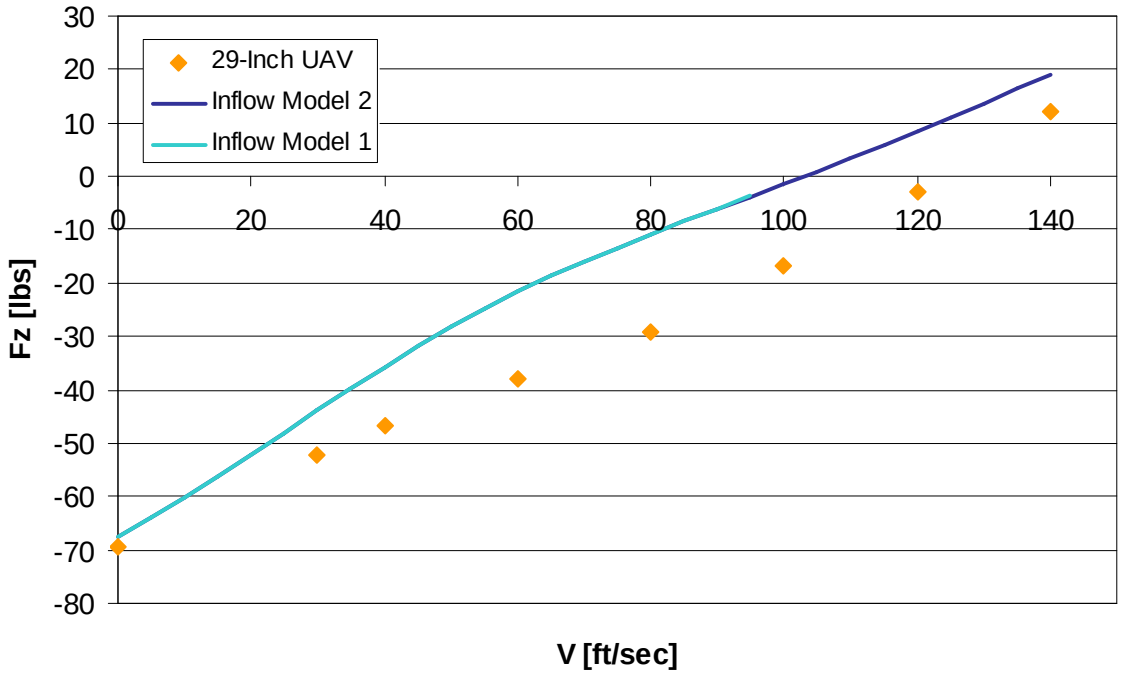

Figure 4.28. Axial Force vs Airspeed ($\Omega = 6000$ RPM, $\alpha = -60°$).

The results generated for axial force correlate well with the UAV wind tunnel data, particularly in the direction of the trends. The results indicate that axial force increases in magnitude (becomes more negative) as airspeed is increased at small angles of attack. This result is expected because the increase in airspeed produces more duct thrust, and therefore a larger axial force. At larger nose-down angles of attack, however, the axial force decreases in magnitude as airspeed is increased. The decrease in axial force is due to the inflow into the rotor. As the inflow is increased through the rotor, the angle of attack of the blades is reduced, and, in turn, the thrust generated. In addition, fuselage drag acts in the opposite direction of axial force at near-axial flight conditions, which also contributes to the decreasing trend.

4.4 Correlation of Normal Force

Normal force, F_x, is presented versus airspeed in Figures 4.29 through 4.42. Normal force is measured as positive in the negative longitudinal (x-axis) of the duct, and a positive normal force is considered to be a drag force when the duct is at zero angle of attack.

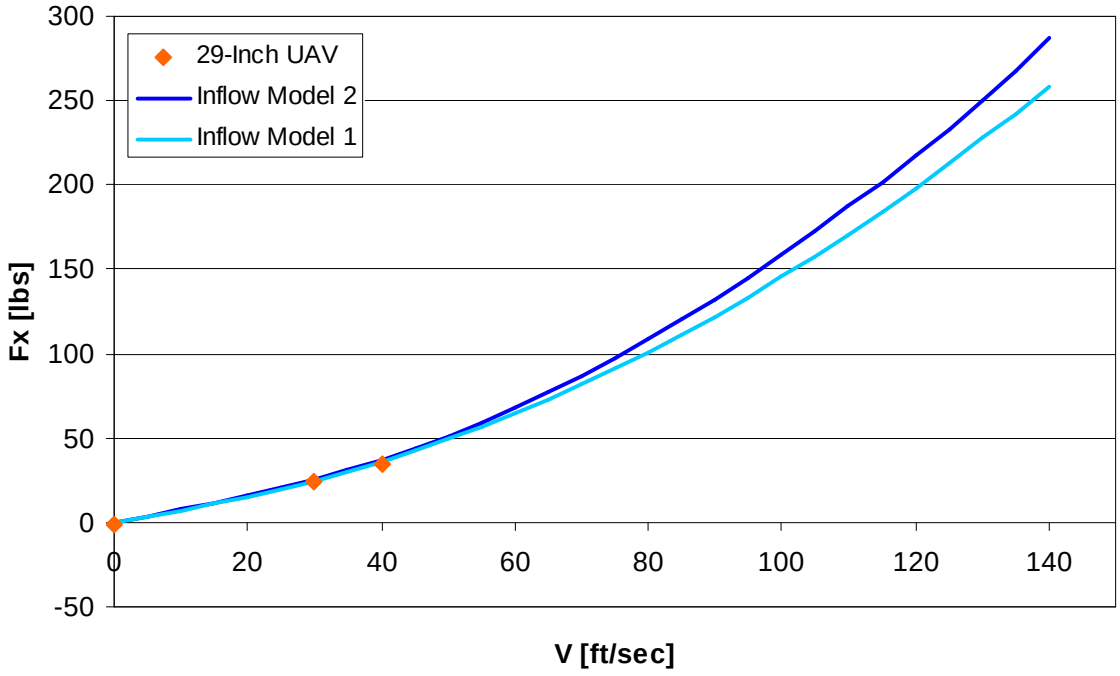

Figure 4.29. Normal Force vs Airspeed ($\Omega = 5500$ RPM, $\alpha = 0°$).

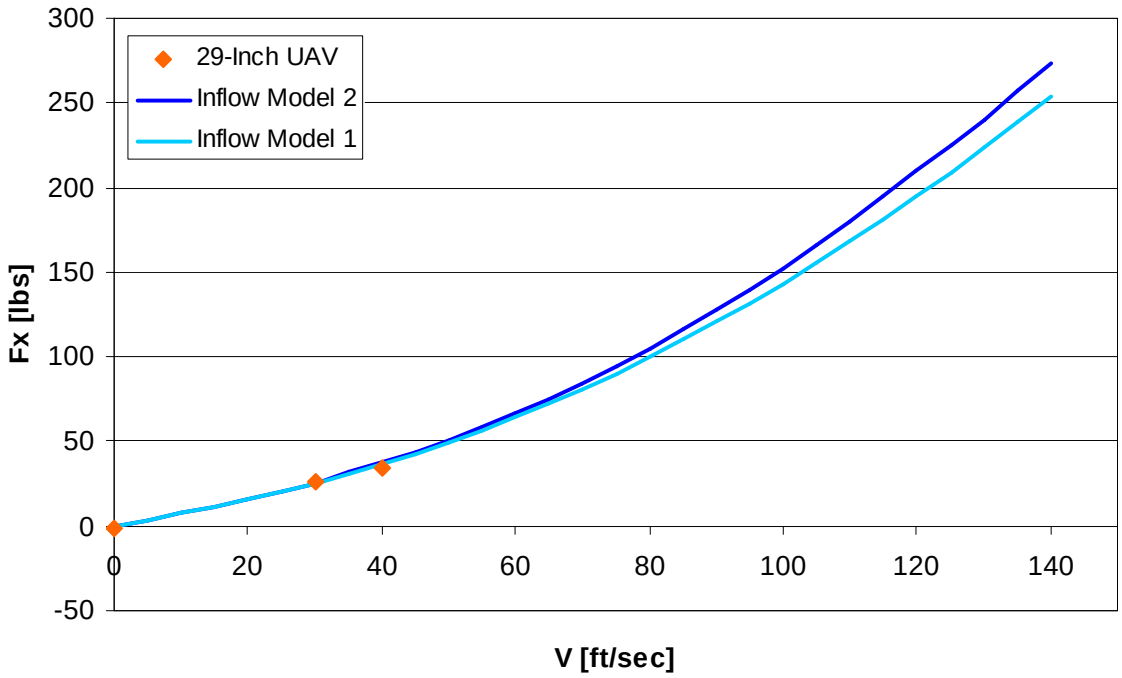

Figure 4.30. Normal Force vs Airspeed ($\Omega = 5500$ RPM, $\alpha = -10°$).

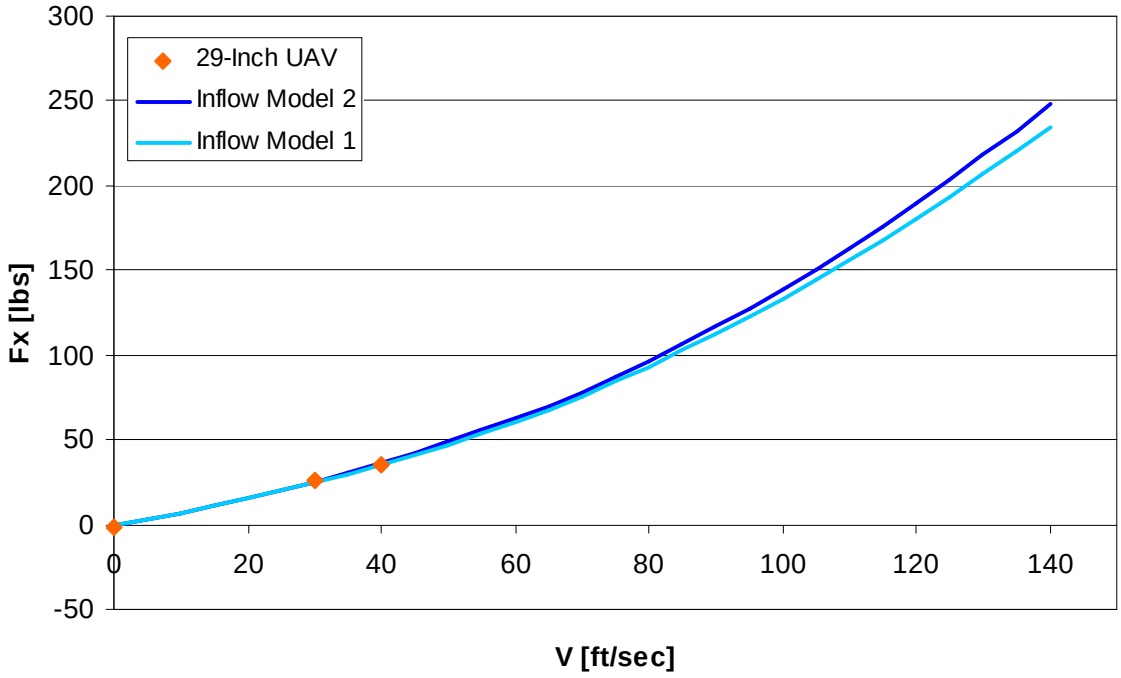

Figure 4.31. Normal Force vs Airspeed ($\Omega = 5500$ RPM, $\alpha = -20°$).

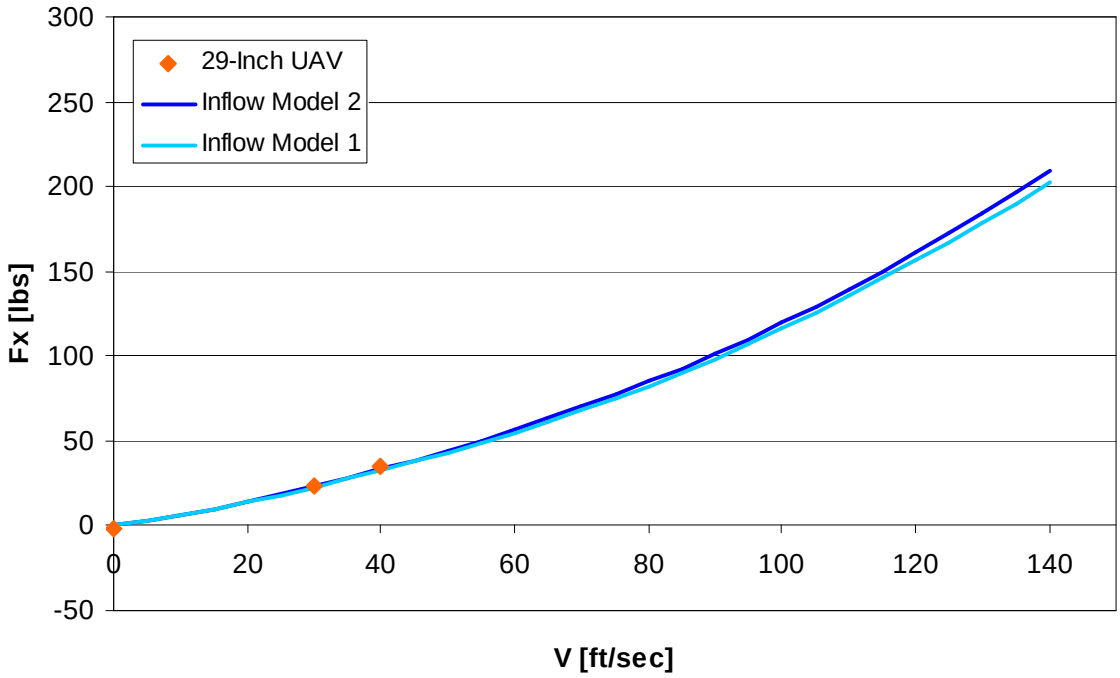

Figure 4.32. Normal Force vs Airspeed ($\Omega = 5500$ RPM, $\alpha = -30°$).

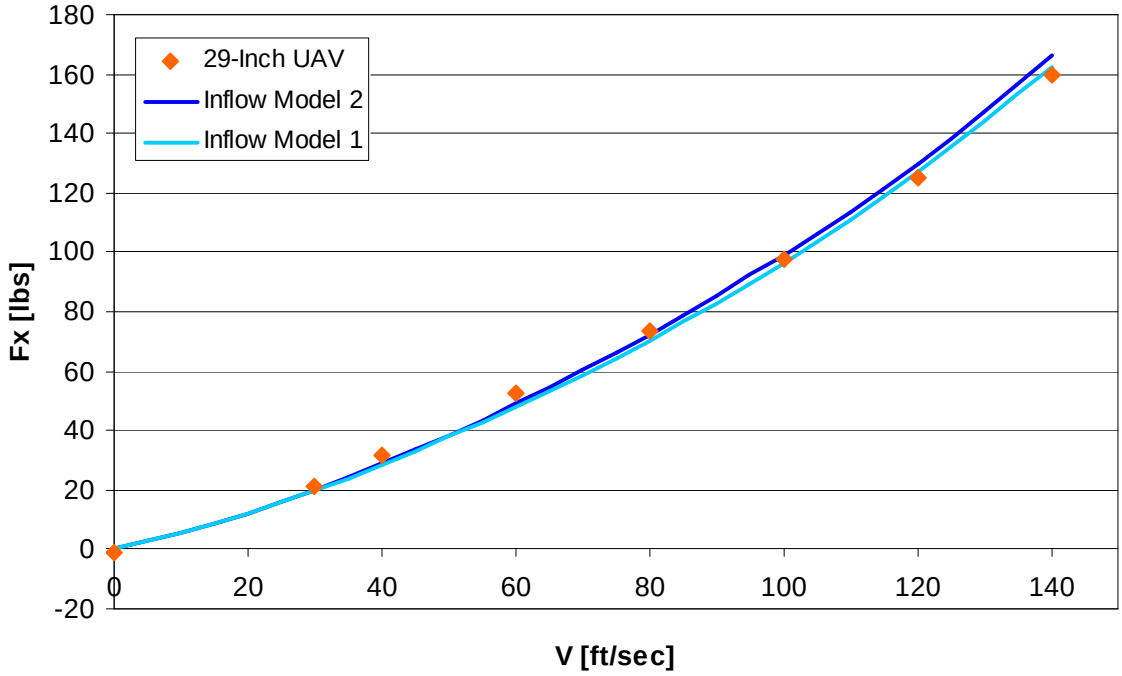

Figure 4.33. Normal Force vs Airspeed ($\Omega = 5500$ RPM, $\alpha = -40°$).

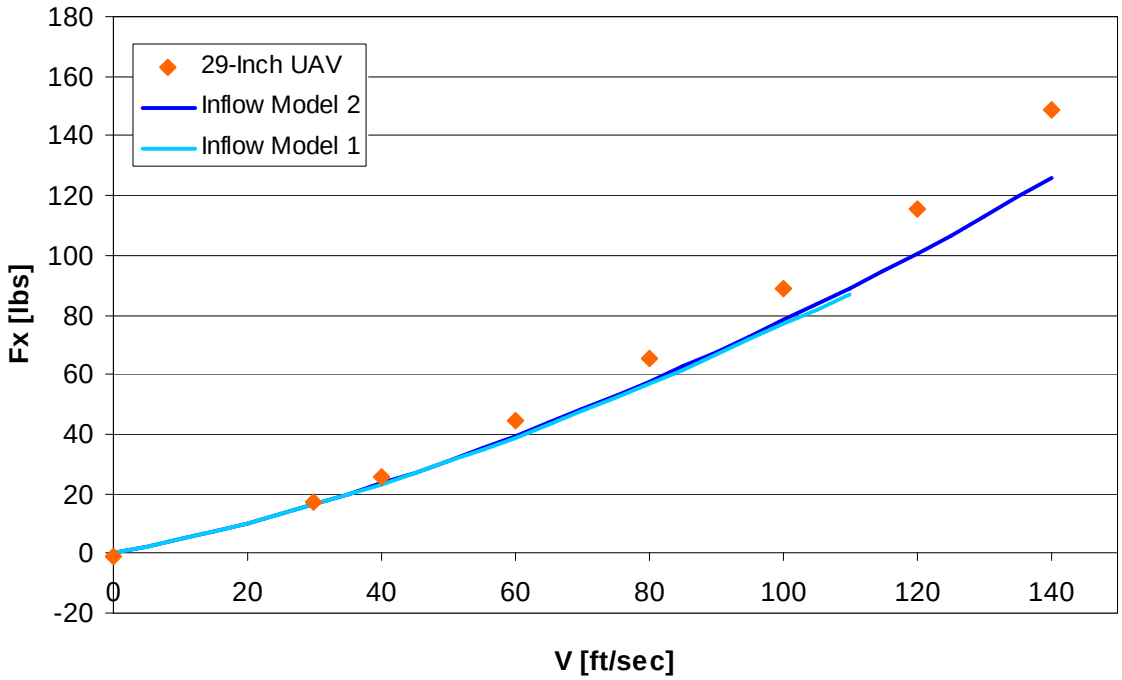

Figure 4.34. Normal Force vs Airspeed ($\Omega = 5500$ RPM, $\alpha = -50°$).

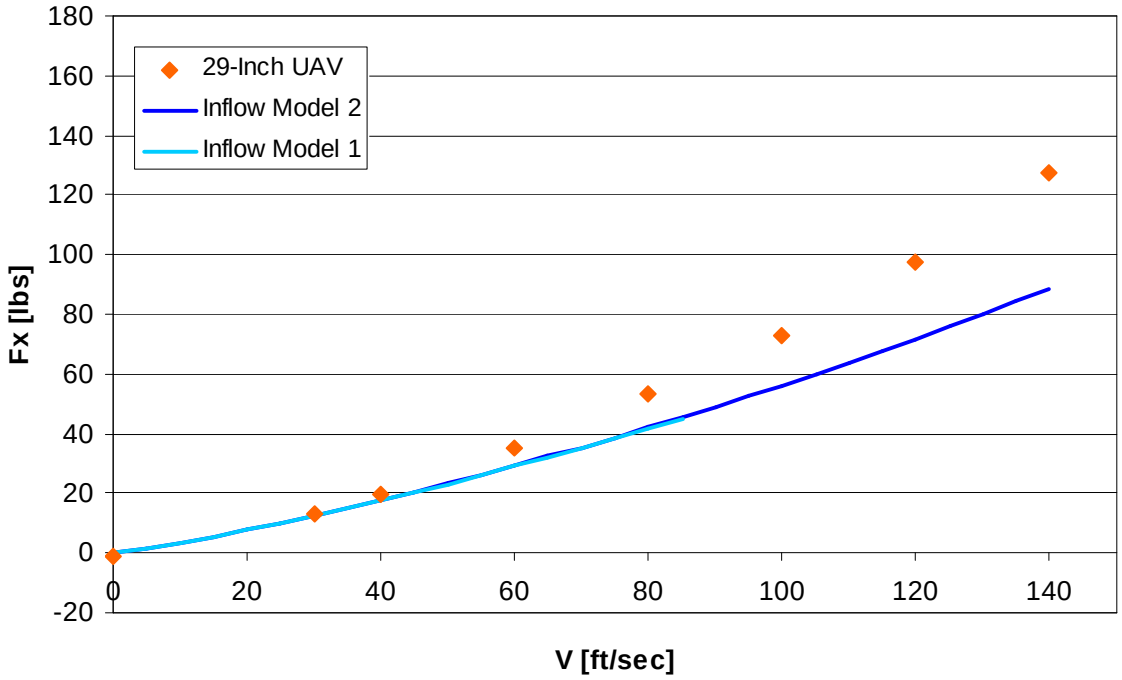

Figure 4.35. Normal Force vs Airspeed ($\Omega = 5500$ RPM, $\alpha = -60°$).

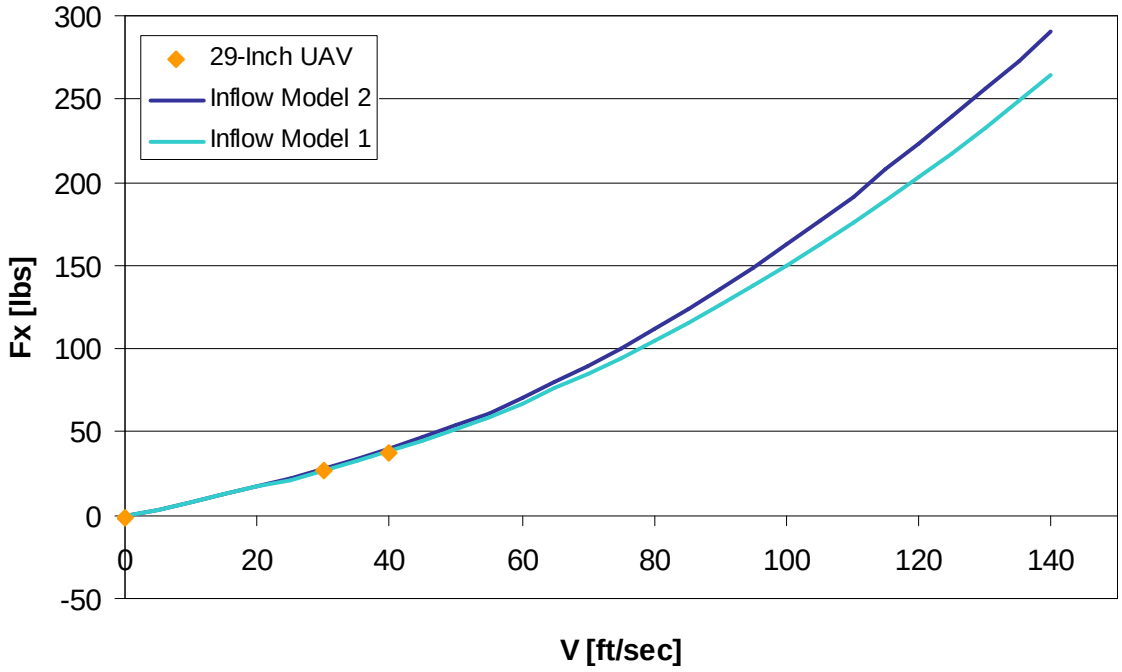

Figure 4.36. Normal Force vs Airspeed ($\Omega = 6000$ RPM, $\alpha = 0°$).

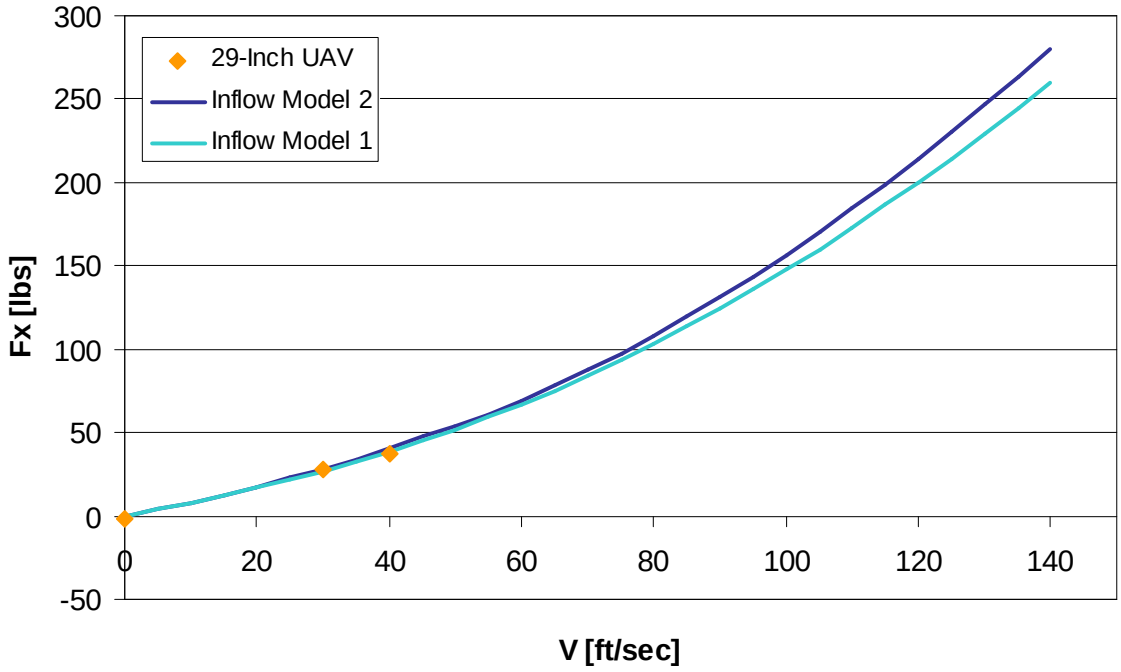

Figure 4.37. Normal Force vs Airspeed ($\Omega = 6000$ RPM, $\alpha = -10°$).

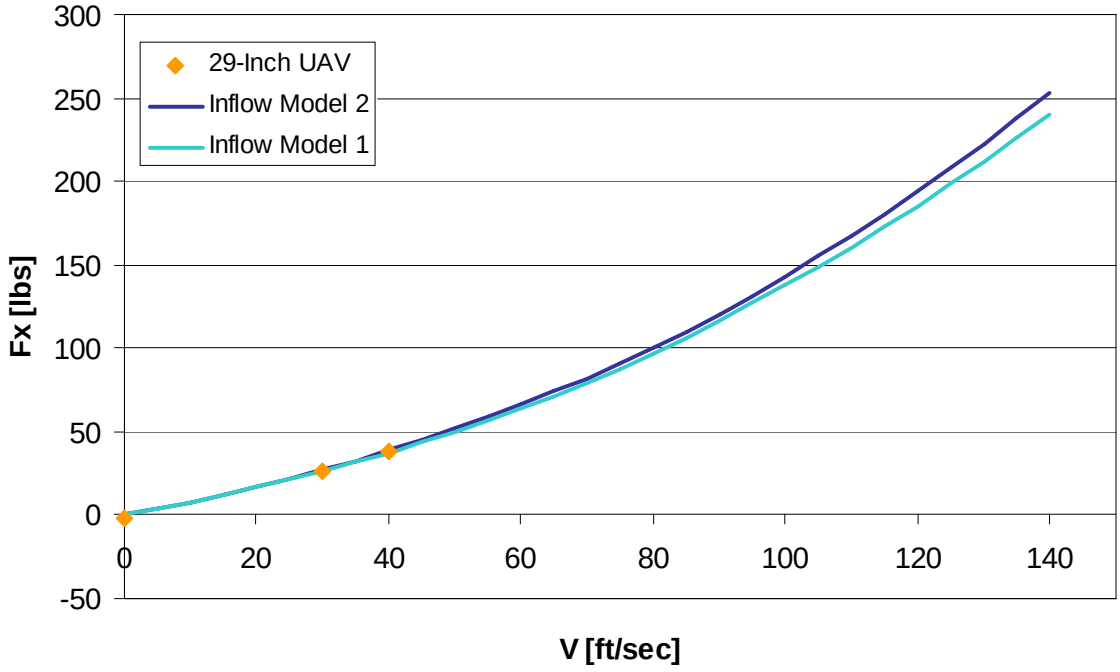

Figure 4.38. Normal Force vs Airspeed ($\Omega = 6000$ RPM, $\alpha = -20°$).

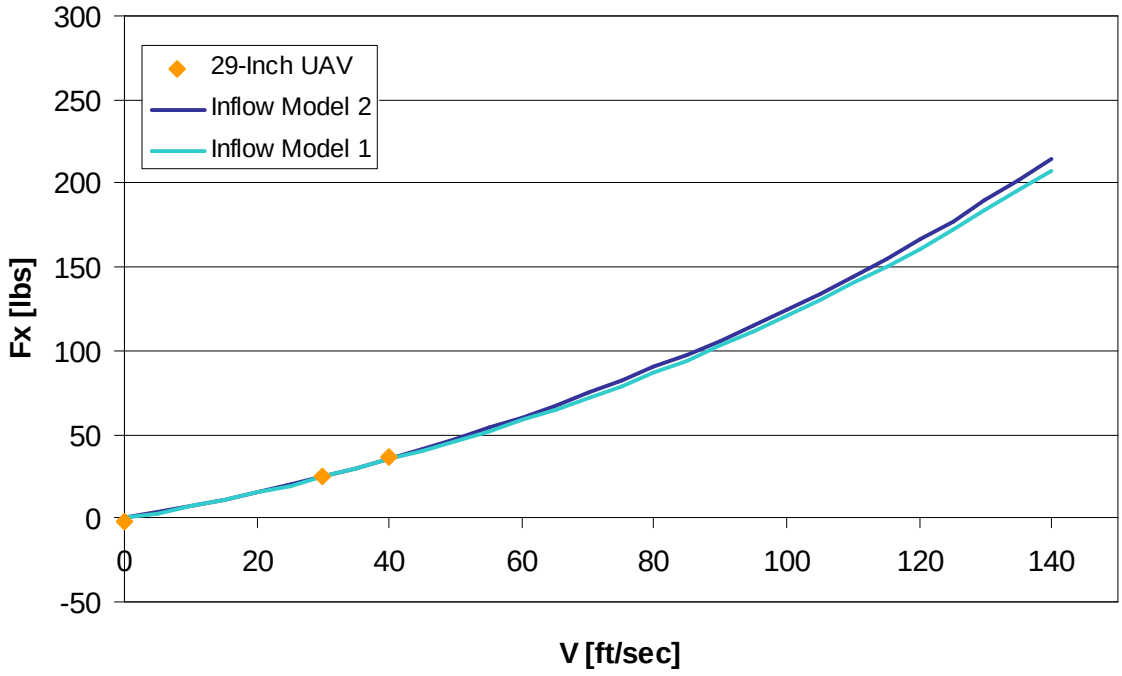

Figure 4.39. Normal Force vs Airspeed ($\Omega = 6000$ RPM, $\alpha = -30°$).

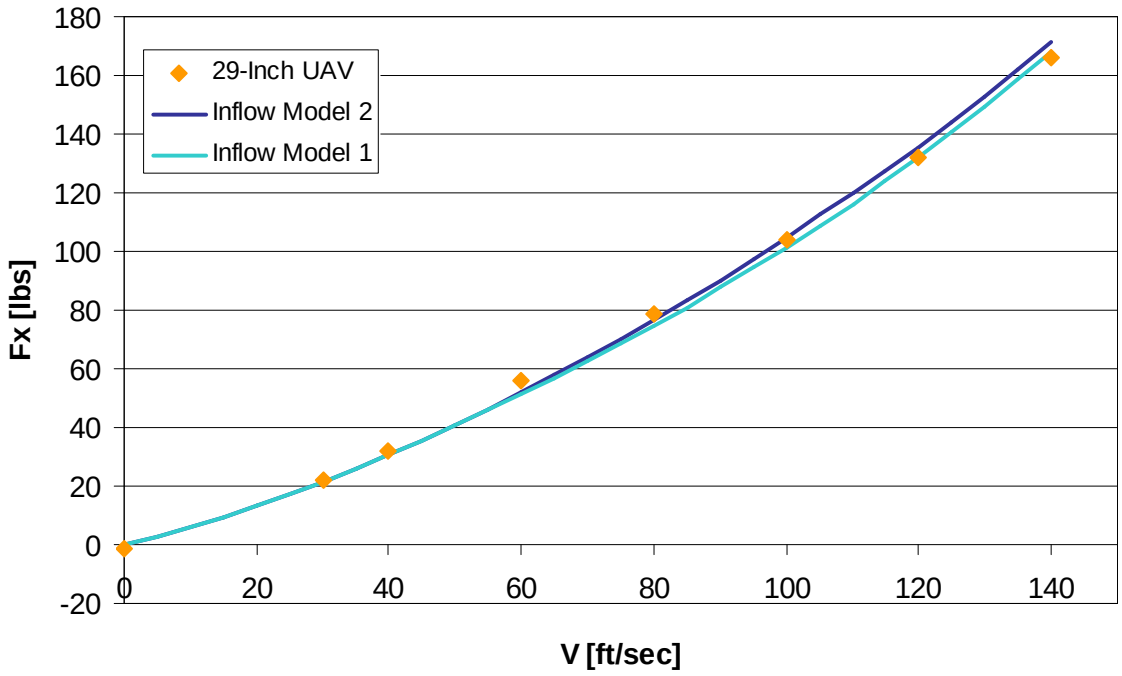

Figure 4.40. Normal Force vs Airspeed ($\Omega = 6000$ RPM, $\alpha = -40°$).

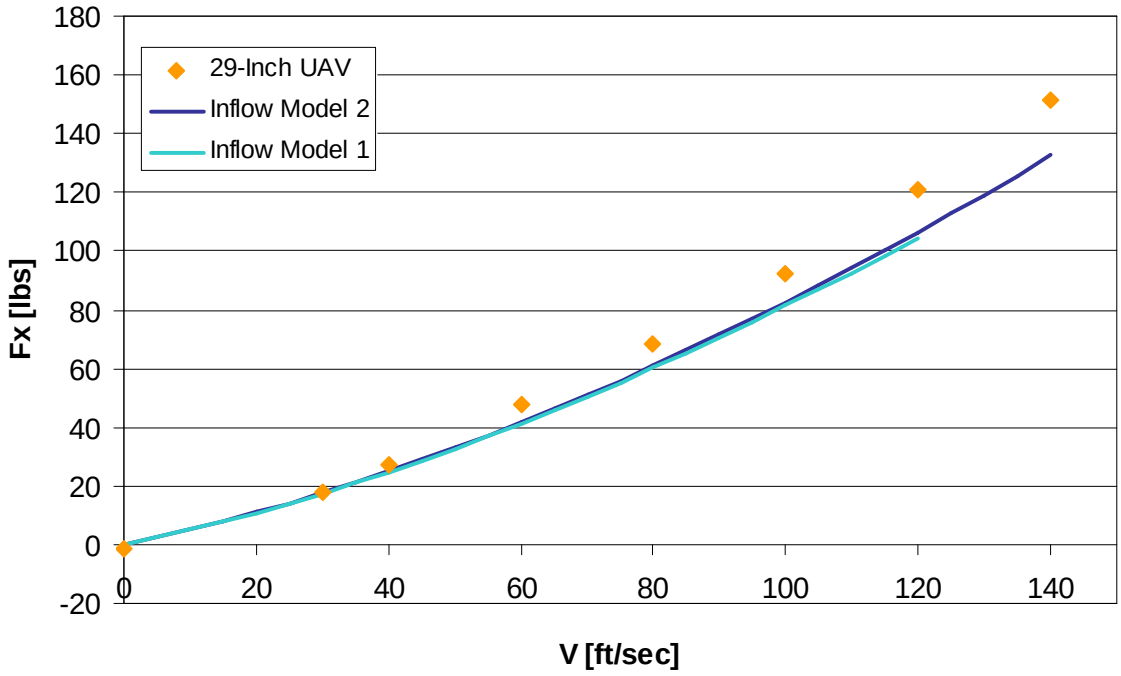

Figure 4.41. Normal Force vs Airspeed ($\Omega = 6000$ RPM, $\alpha = -50°$).

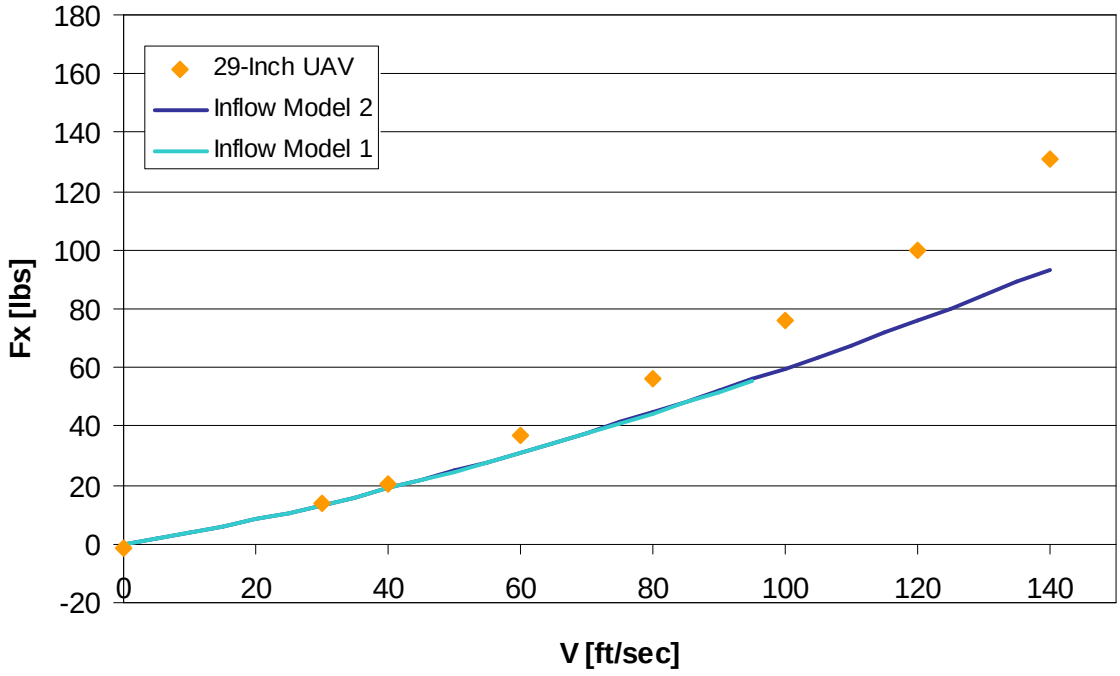

Figure 4.42. Normal Force vs Airspeed ($\Omega = 6000$ RPM, $\alpha = -60°$).

The results generated for normal force versus airspeed match quite well with the experimental wind tunnel data at all angles of attack. Discrepancies at high airspeeds and large nose-down angles of attack, in which the generic model slightly underestimates the normal force, are attributed to the calculation of fuselage drag. Further development of the fuselage drag model would improve the accuracy of the simulation model at high airspeeds.

4.5 Correlation of Pitching Moment due to Longitudinal Vane Deflection

The pitching moments created by the deflection of longitudinal control vanes on the ducted fan system were analyzed. Results produced using the generic ducted fan model, configured with Inflow Model 2, were compared with data of the 29-Inch UAV operating at a rotor speed of 6000 RPM. A limited amount of data on pitching moment versus vane deflection for the UAV were available; therefore only a few cases were included in the correlation study. Specifically, the cases include $\alpha = 0°$ at zero airspeed, $\alpha = 0°$, $30°$ and $60°$ at an airspeed of 40 ft/sec, and $\alpha = 40°$, $50°$ and $60°$ at an airspeed of 80 ft/sec.

The nonlinearity of the results computed using the generic simulation model are attributed to stalling of the control vanes. Also, because of the flow's swirl velocity component incorporated in the model, one longitudinal control vane may stall at a different deflection angle than the other, thus further complicating the nonlinear trend. Note that the 29-Inch UAV has stators positioned before the control vanes, as seen in Figure 2.7, that tend to remove the swirl component of the flow. Stators are not modeled in the generic simulation model, however.

A vane deflection bias of $5°$ was also implemented and investigated at an airspeed of 40 ft/sec. The bias adds $5°$ to the deflection of each control vane, thus accounting for the swirl component of the exit flow. Note that the vane deflection bias removes the nonlinearity in the pitching moment at small vane deflections, and causes the vanes to stall simultaneously at some deflection angle. The results of the investigation indicate that it is possible to tune the vane deflection bias to regulate vane stall and, in turn, the pitching moment generated.

Vane sizes and location used in the following comparisons are identical to those used in the other correlation studies. The results correlate relatively well; however, altering the vane size, placement, or perhaps the airfoil data may produce more closely matched results.

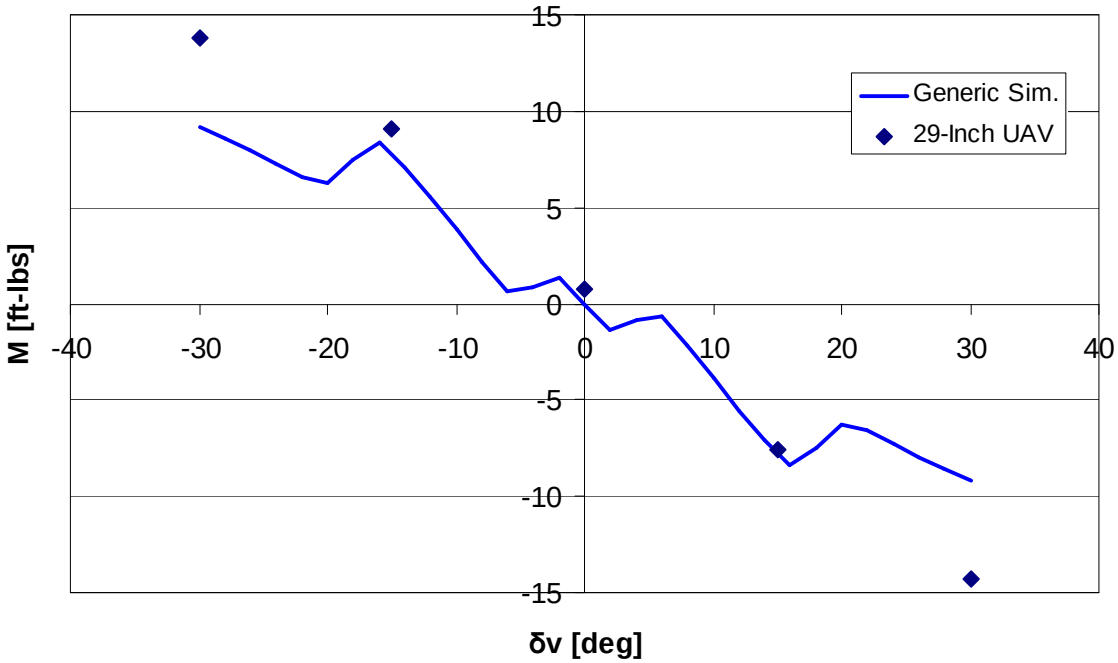

Figure 4.43. Pitching Moment vs Longitudinal Vane Deflection ($V = 0\ ft/s$, $\alpha = 0°$).

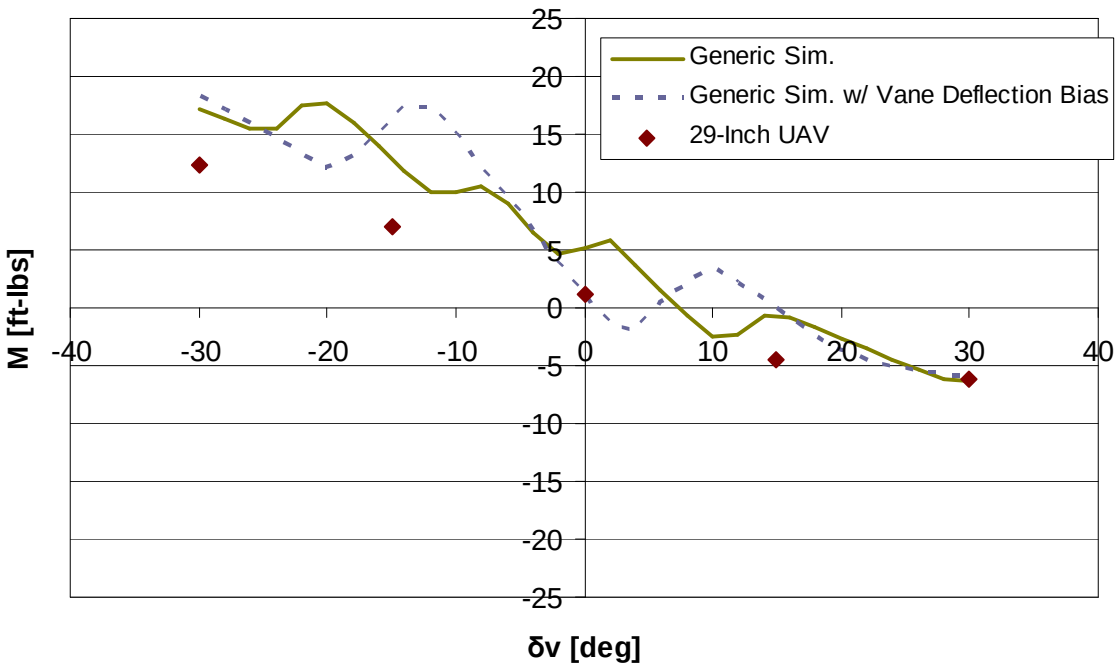

Figure 4.44. Pitching Moment vs Longitudinal Vane Deflection ($V = 40\ ft/s$, $\alpha = 0°$).

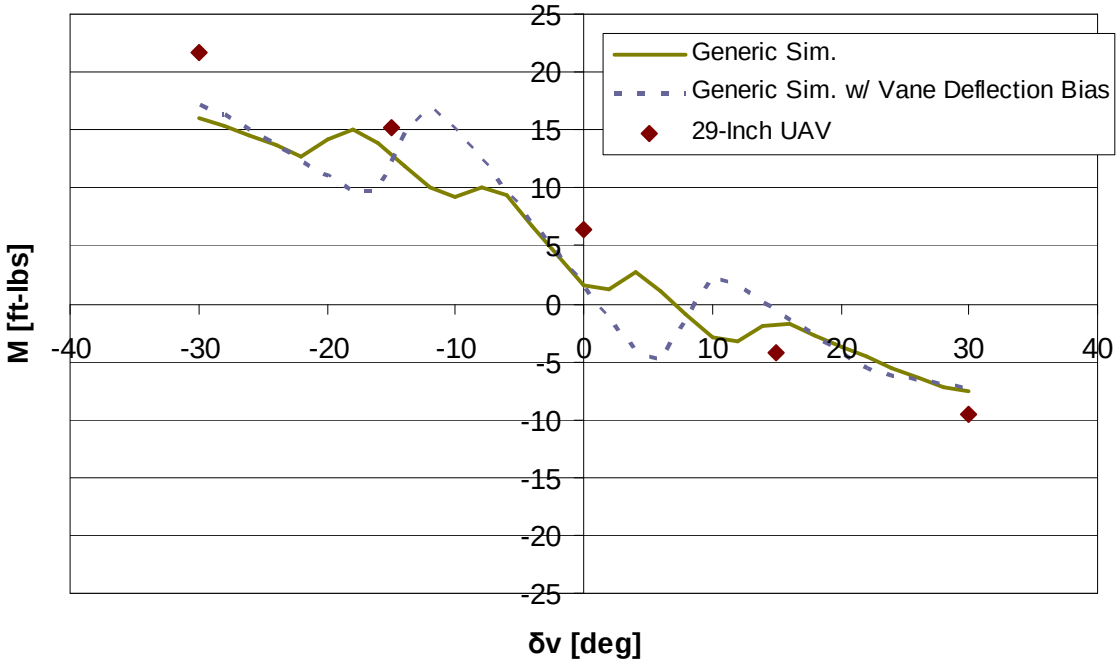

Figure 4.45. Pitching Moment vs Longitudinal Vane Deflection ($V = 40\ ft/s$, $\alpha = 30°$).

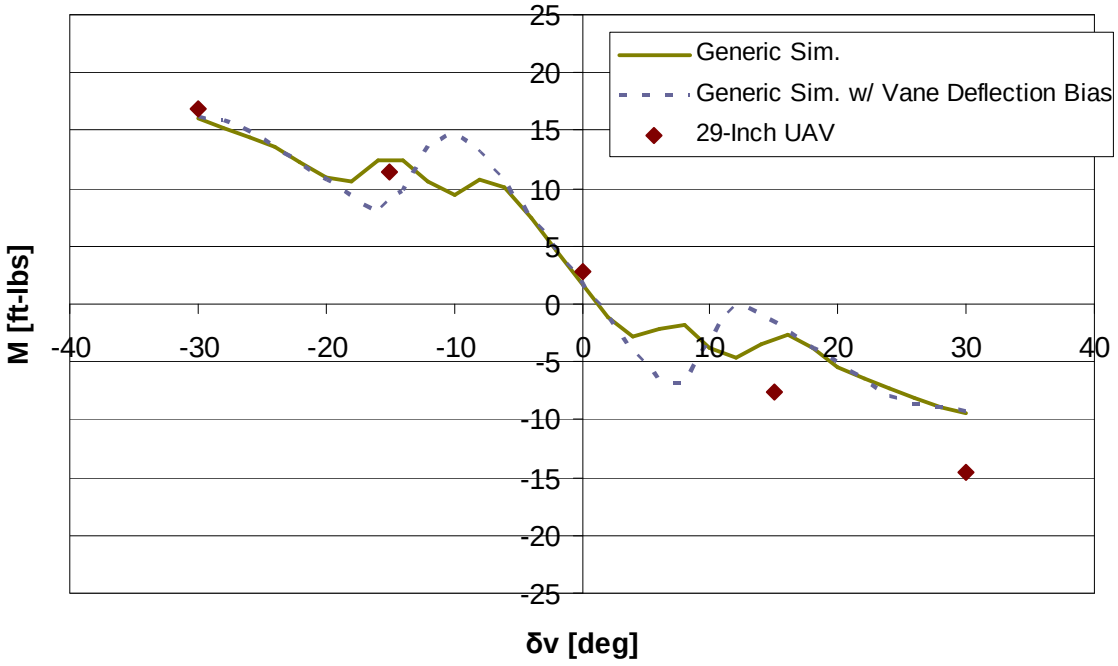

Figure 4.46. Pitching Moment vs Longitudinal Vane Deflection ($V = 40\ ft/s$, $\alpha = 60°$).

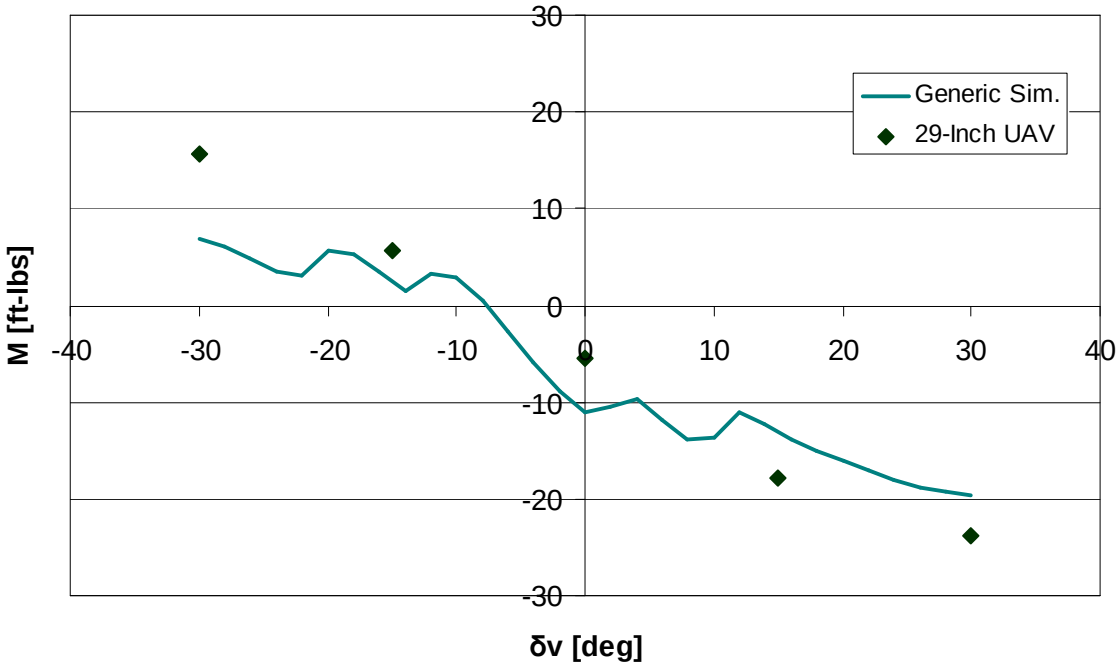

Figure 4.47. Pitching Moment vs Longitudinal Vane Deflection ($V = 80\ ft/s$, $\alpha = 40°$).

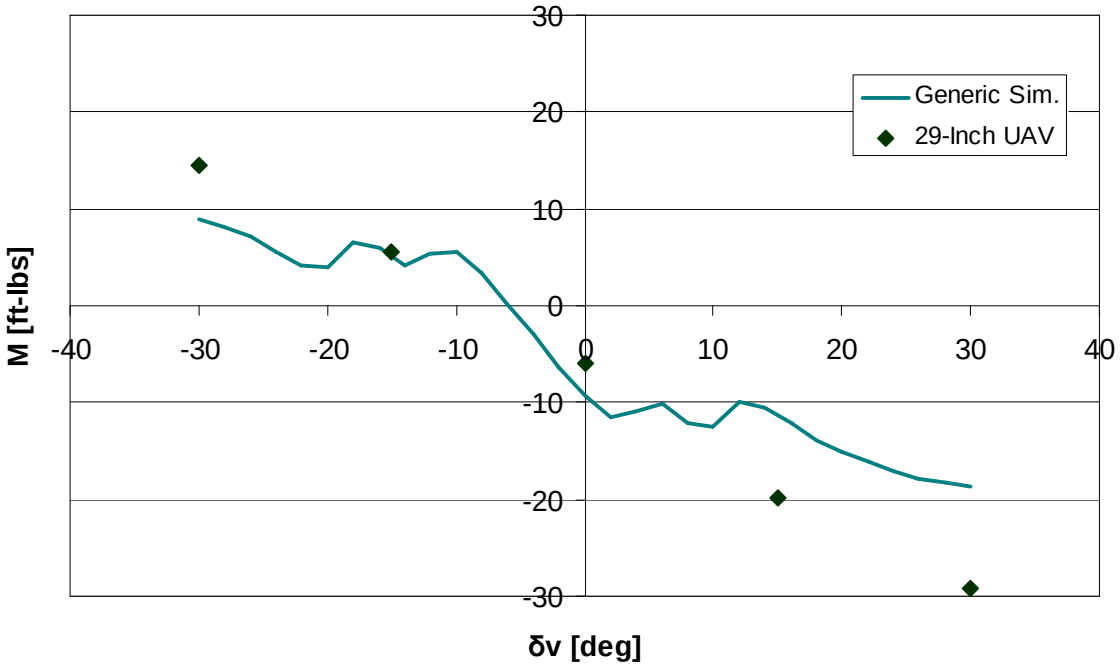

Figure 4.48. Pitching Moment vs Longitudinal Vane Deflection ($V = 80\ ft/s$, $\alpha = 50°$).

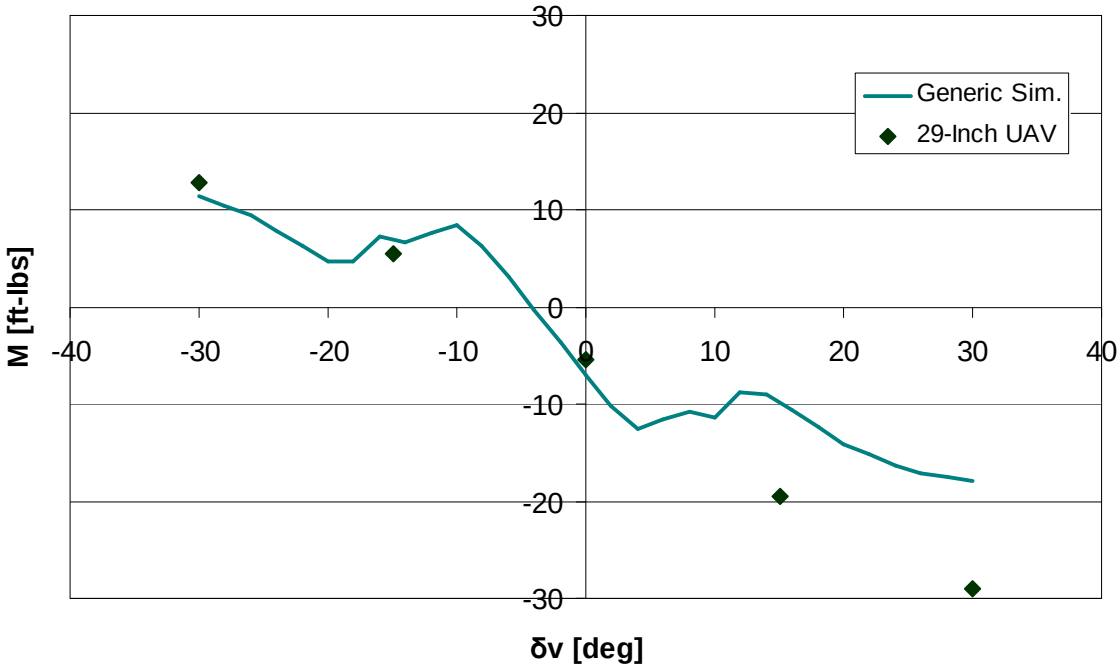

Figure 4.49. Pitching Moment vs Longitudinal Vane Deflection ($V = 80\ ft/s$, $\alpha = 60°$).

Chapter 5

Control System Design

5.1 Control Mixing Function for Tandem Ducted Fan Aircraft

A control mixing function was developed that converts conventional pilot inceptor inputs into a combination of exit vane deflections, and rotor collective and cyclic pitch. The pilot's inceptor inputs, in percent, are manipulated by gains, biases, and summing junctions that produce control deflections on the aircraft in degrees.

A schematic of the control mixing function can be seen in Figure 5.1. The control mixing function was designed to accommodate changes in aircraft configuration and it is easily modifiable. A summary of the elements in the control mixing function can be found in Table 5.1, and the range of control authority can be found in Table 5.2.

Because of the aircraft's tandem configuration, modifications from the standard control mixing of a conventional helicopter are necessary. Collective pitch control is achieved through the pilot's collective stick, in which an increase in collective

Pilot Inceptor	Control Deflection	Attitude Control
δ_{lat}	longitudinal cyclic pitch	roll
δ_{lon}	differential collective pitch	pitch
δ_{col}	collective pitch	heave
δ_{ped}	differential lateral vane	yaw

Table 5.1. Tandem Ducted Fan Control Mixing Elements.

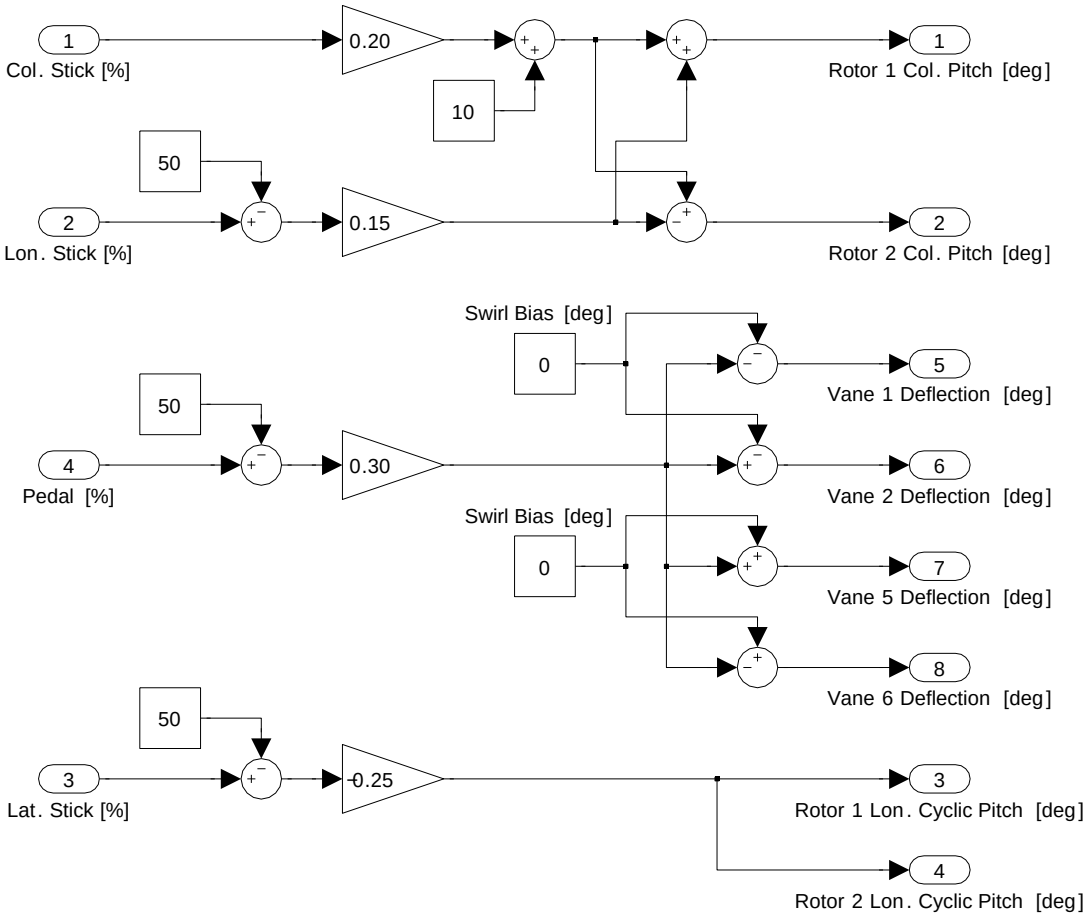

Figure 5.1. Tandem Ducted Fan Control Mixing Schematic.

stick corresponds to an increase in collective pitch on both rotors equally. It is interesting to note that increasing the collective in hover, for example, does not result in an increase in yaw moment of the aircraft as it would on a conventional helicopter. The opposite rotational directions of the tandem rotors cancel the increase in torque reaction produced by each rotor, and thus no net moment is experienced.

Lateral pilot stick deflections control lateral cyclic pitch on both rotors, which allow for roll control of the aircraft. It is important to note that rigid blades are used in the ducted rotor model; thus there is no phase lag between control inputs and rotor response. Therefore, *longitudinal* cyclic pitch, θ_{1c}, is actually used for roll control. Conventional lateral cyclic pitch would be used in the case of articulated rotor blades.

Longitudinal stick deflections control differential collective pitch on the rotors. Specifically, a forward stick displacement results in increased collective pitch on the aft rotor and a decrease in collective pitch on the front rotor, which correspond to pitch control of the aircraft. There is, however, cross-coupling between longitudinal stick displacement and yaw moment because the increase in collective pitch of one rotor increases the torque reaction on that rotor, and thus a net yaw moment is experienced.

Rudder pedals control differential lateral vane deflections, which allow for yaw control of the aircraft. Because the exit control vanes are located below the center of gravity of the aircraft, there is cross-coupling between lateral vane deflections and roll moment on the aircraft. This cross-coupling effect is illustrated in Figure 5.2.

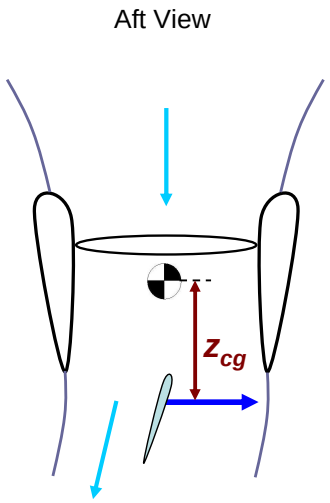

Figure 5.2. Pedal/Roll Cross-Coupling due to Vertical C.G. Offset of Vane.

There is a swirl bias term included in the control mixing function. This constant value is the amount of vane deflection, in degrees, that is added to each control vane to account for the swirl component of the exit flow. Note that the numbering convention used to label the control vanes is identical to the convention used in the FLIGHTLAB analysis, as shown in Figure 3.2.

An investigation into the vane deflection bias is briefly discussed in the vane correlation studies presented in Section 4.5. Future versions of the simulation model may contain a controller for the vane deflection bias as a function of rotor

Pilot Incpt.	Incpt. Range	Incpt. Orientation	Control Authority
δ_{lat}	0–100 %	left-right	$-12.5^\circ \leq \theta_{1c} \leq 12.5^\circ$
δ_{lon}	0–100 %	fore-aft	$-7.5^\circ \leq \theta_0 \leq 7.5^\circ$
δ_{col}	0–100 %	down-up	$10^\circ \leq \theta_0 \leq 30^\circ$
δ_{ped}	0–100 %	left-right	$-15^\circ \leq \delta_{v_{lat}} \leq 15^\circ$

Table 5.2. Tandem Ducted Fan Control Authority.

torque instead of a constant value, for example, to better accommodate the exit flow swirl component.

5.2 Investigation of Longitudinal Vane Control

The effects of using longitudinal vane deflections in forward flight were investigated using FLIGHTLAB. The goal was not only to determine whether the longitudinal deflection of the vanes would provide additional thrust in forward flight, but to also reduce an extreme nose-down attitude the vehicle may experience at a high forward flight speed.

Several variations in the control mixing function used for the deflection of longitudinal vanes were implemented and analyzed. In each case, however, the longitudinal vane deflection is only a function of airspeed, in which the vane deflection angle increases linearly from zero in hover to some angle in forward flight.

A few vane deflection rates are plotted in Figure 5.3, and results of the various configurations are presented in Figures 5.4 and 5.5. The first case shows no vane deflection, which corresponds to no control over the longitudinal vanes. The following two approximate rates, $0.12^\circ/fps$ (feet per second) and $0.26^\circ/fps$, correspond to 20° and 45° of longitudinal vane deflection, respectively, per 100 knots. The final case has a deflection rate of approximately $0.26^\circ/fps$ as well; however the deflection is limited to 25 degrees. Although the vane deflections appear to become quite large, the wake is skewed at the exit of the duct. Therefore the angle of attack of a vane is less than the vane deflection angle.

Figure 5.4 shows the results of the various vane deflection functions on trim pitch attitude. It is apparent from the results that longitudinal vane deflection as a function of forward flight speed decreases the nose-down pitch attitude for almost all of the trim flight speeds in the given range. Also, a higher rate of

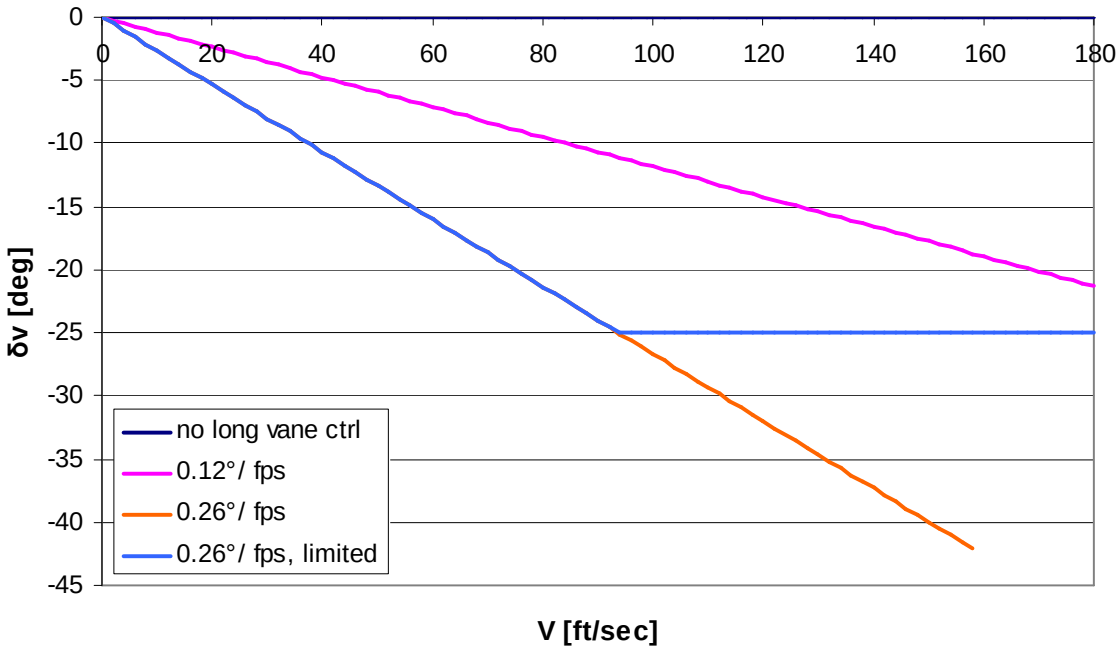

Figure 5.3. Longitudinal Vane Deflection vs Trim Airspeed.

vane deflection results in greater nose-down alleviation; however the $0.26°/fps$ case without the limiter terminates at the lowest airspeed. This is a result of the aircraft losing collective authority sooner than the other cases, which can be seen in the figure of collective stick displacement versus trim airspeed, Figure 5.5. The loss of collective authority at a lower flight speed is due to the inability to supply the power required to turn the flow. Additional power is required when the vane stalls in order to overcome the drag created by the vane.

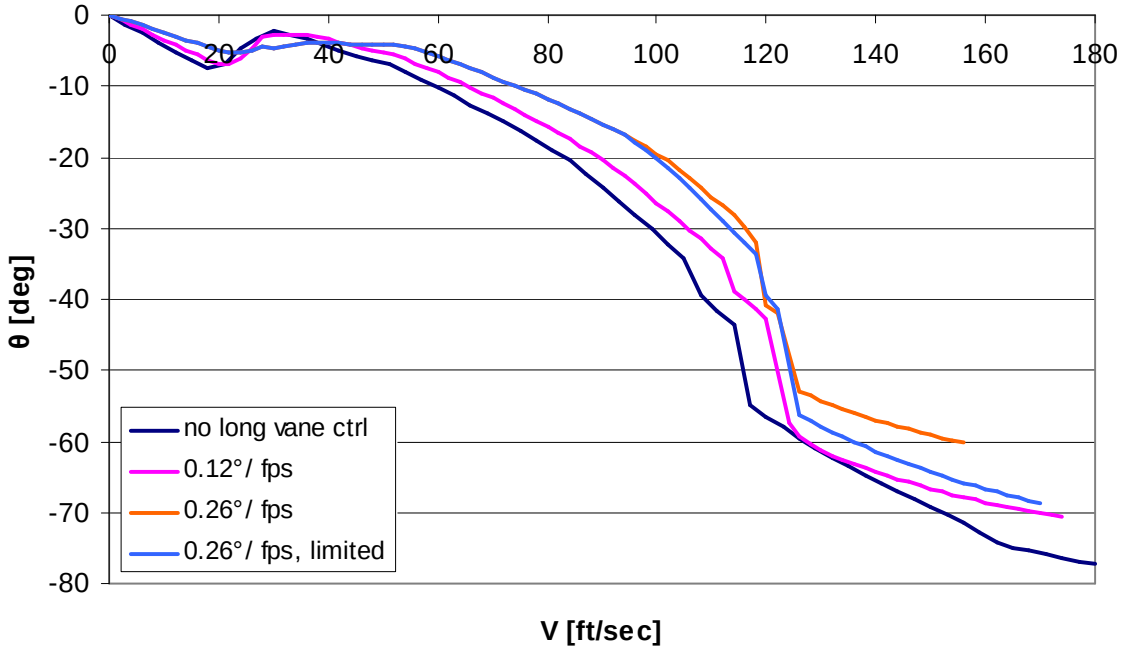

Figure 5.4. Pitch Attitude vs Trim Airspeed with Longitudinal Vane Control.

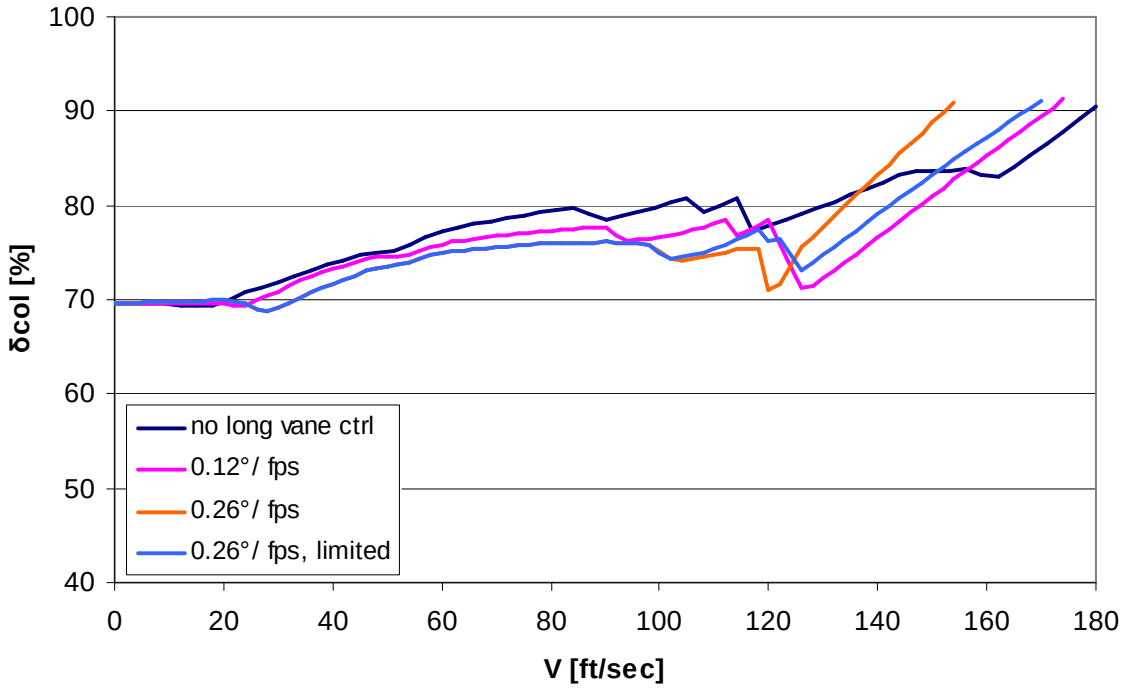

Figure 5.5. Collective Stick Displacement vs Trim Airspeed with Longitudinal Vane Control.

Chapter 6

Simulation Results

6.1 Trim Flight

Results of the trim flight controls needed through a range of airspeeds for the FLIGHTLAB model and the generic simulation model are presented. Trim flight analysis is important for the validation of the control system and pitching moment model. The trim results are also used to determine the operational limitations of the vehicle based on the control deflections needed at particular flight conditions.

6.1.1 FLIGHTLAB Simulation Results

A trim sweep was conducted using the large tandem ducted fan configuration modeled in FLIGHTLAB. The trends of the trim flight controls, particularly the increase in collective with an increase in airspeed, sparked the initial curiosity of the effects of the duct, and thus the inflow behavior before the plane of the rotor.

Note the continual increase in collective stick displacement versus trim flight speed. The collective stick behaves differently than that of an open rotor, in which the collective generally decreases as airspeed increases due to translational lift effect, and then increases as more power is required at higher flight speeds. The increasing trend of collective pitch over the entire flight range suggests that the ducted rotor configuration experiences very little translational lift effect.

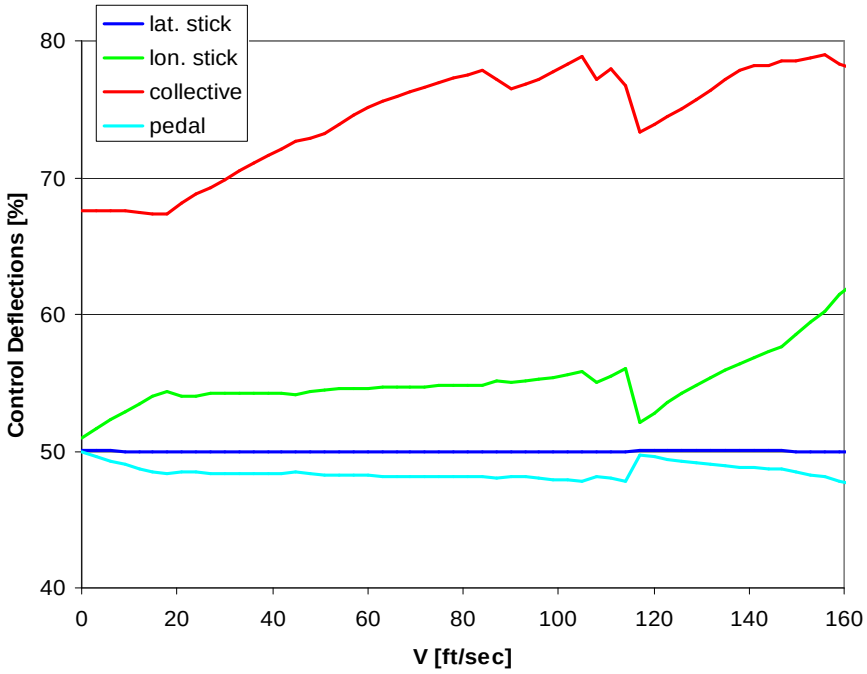

Figure 6.1. FLIGHTLAB Trim Flight Controls vs Airspeed.

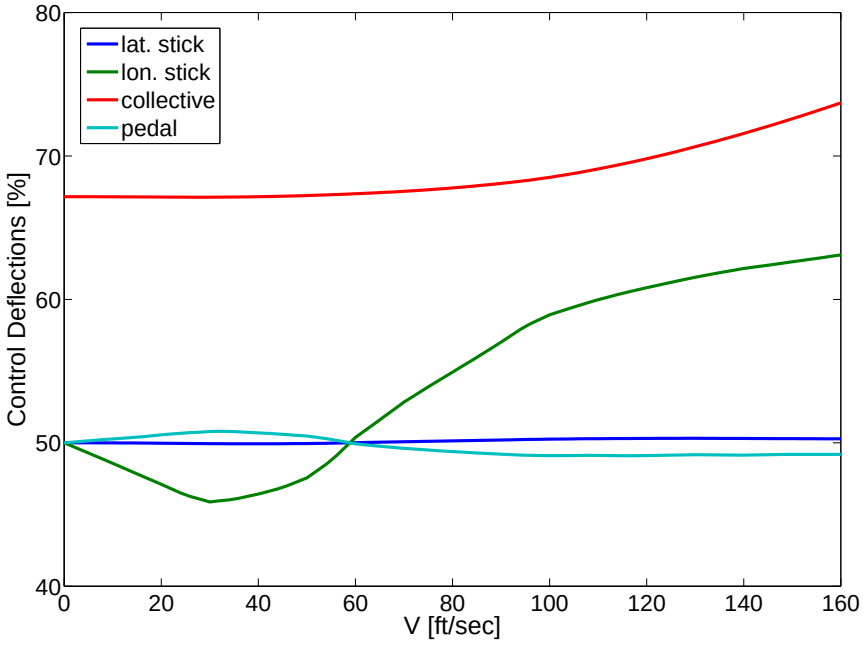

Figure 6.2. Generic Simulation Trim Flight Controls vs Airspeed ($k_{aug} = 0.40$, $k_{\chi_\infty} = 0.85$, $k_{\chi_R} = 0.75$).

6.1.2 Generic Tandem Ducted Fan Simulation Results

The large tandem ducted fan configuration, which is described in Section 2.5.2, was analyzed in sweeps of forward flight speeds using the generic simulation environment. Figure 6.2 was generated using empirical values that produced results that most closely matched the trends of the FLIGHTLAB trim sweep shown in Figure 6.1.

Comparisons of the trim flight controls between the FLIGHTLAB and generic simulation results show similar trends. Note the slight variation in trim lateral stick deflection as forward speed is increased due to cross-coupling between lateral stick and pedal. Also, note the cross-coupling between longitudinal stick and pedal.

Longitudinal stick displacement of the generic simulation model follows the trend of duct pitching moment versus airspeed, particularly normalized duct thrust offset versus airspeed, as shown in Figure 2.6. Note that the minimum value of longitudinal stick displacement at around 30 ft/sec, which is a forward stick displacement because of its orientation, corresponds to the maximum nose-up pitching moment produced. The forward stick displacement is needed to counteract the nose-up pitching moment generated. Also, note that longitudinal stick returns to center (50%) at approximately 60 ft/sec, which corresponds to zero duct thrust offset in Figure 2.6.

Figures 6.3 through 6.5 illustrate results generated using the same flow turning from the freestream to the far-wake flow ($k_{\chi_\infty} = 0.85$); however the portion of flow turned before the rotor, k_{χ_R}, is varied. Note that Figure 6.3 shows results for the smallest amount of turned flow before the rotor ($k_{\chi_R} = 0.20$). The trend for the collective pitch indicates that there is a prominent translational lift effect experienced by the rotor, much like an open rotor. Subsequent plots show an increase in the portion of turned flow before the plane of the rotor and thus the reduction of translational lift effect.

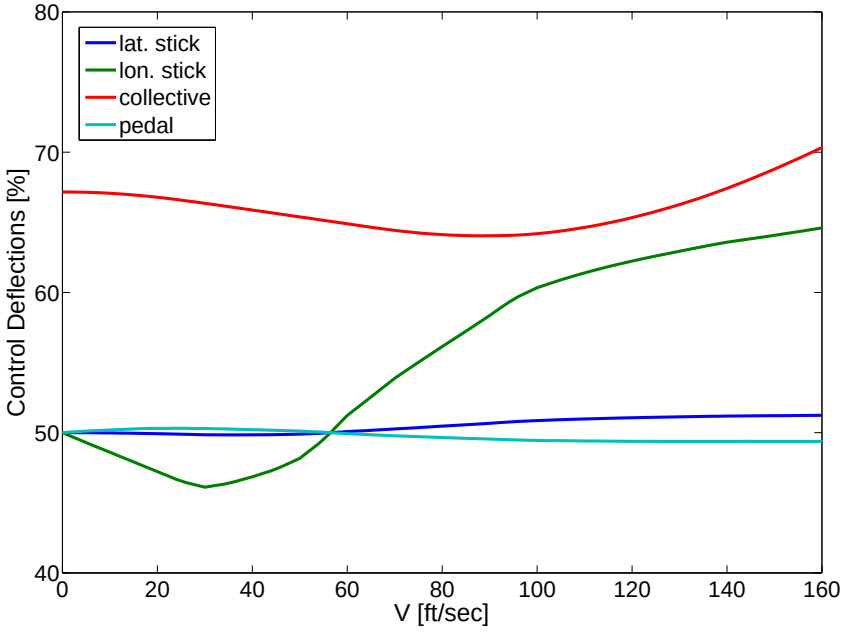

Figure 6.3. Generic Simulation Trim Flight Controls vs Airspeed ($k_{aug} = 0.40$, $k_{\chi_\infty} = 0.85$, $k_{\chi_R} = 0.20$).

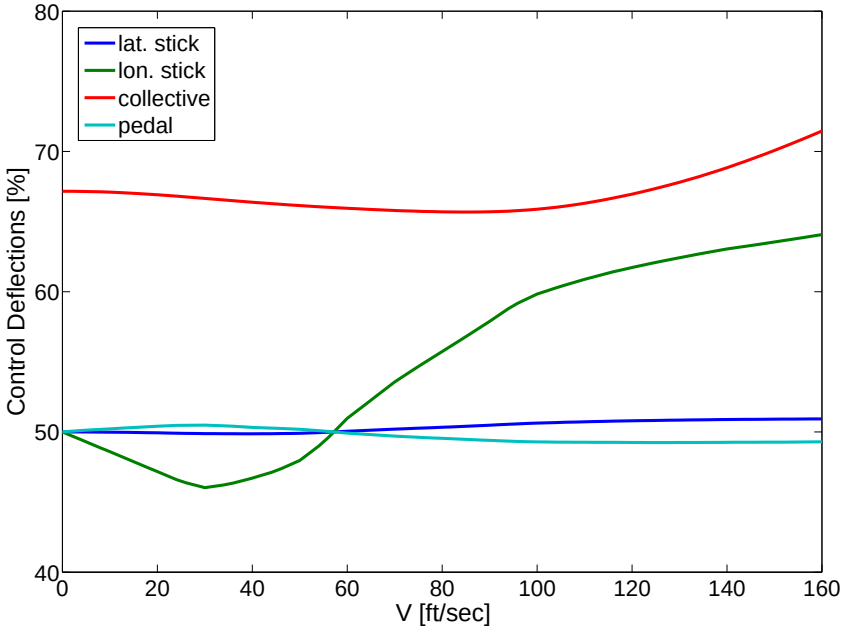

Figure 6.4. Generic Simulation Trim Flight Controls vs Airspeed ($k_{aug} = 0.40$, $k_{\chi_\infty} = 0.85$, $k_{\chi_R} = 0.40$).

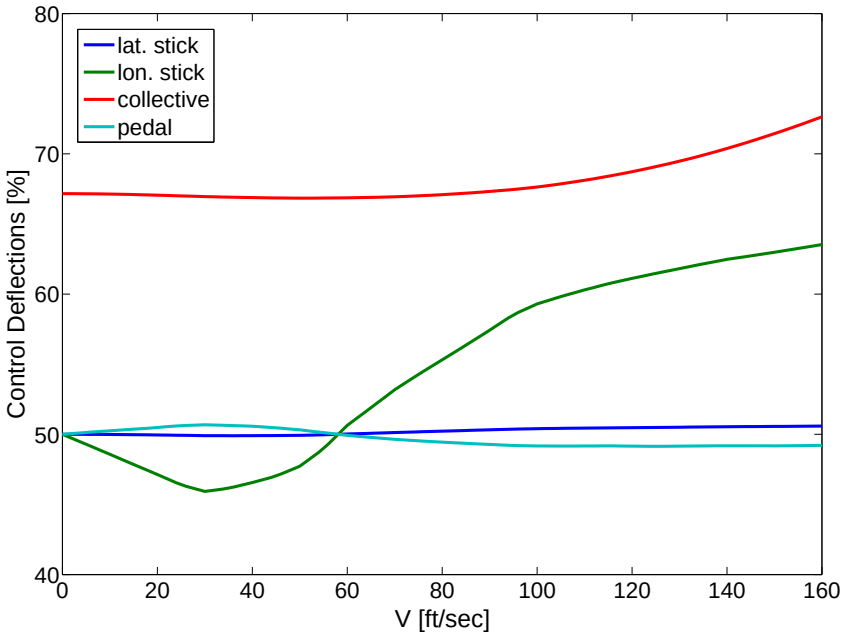

Figure 6.5. Generic Simulation Trim Flight Controls vs Airspeed ($k_{aug} = 0.40$, $k_{\chi_\infty} = 0.85$, $k_{\chi_R} = 0.60$).

Chapter 7

Conclusions and Future Work

7.1 Conclusions

The generic ducted fan simulation model generated results that correlate well with analytical results and experimental data sets of other ducted fan aircraft. Specifically, the single ducted fan configuration yielded results through a range of angles of attack and airspeeds that compared well with the 29-inch UAV experimental wind tunnel data. The comparisons included results of pitching moment coefficient, axial force, normal force, and pitching moment generated by longitudinal control vane deflections. Although simplistic components were included in the generic simulation model, such as basic models of pitching moment and fuselage drag, the aircraft characteristics and empirical factors were easily tuned to produce well-correlated results over a broad range of flight conditions.

Duct pitching moment behavior is sometimes unpredictable, and it varies quite substantially from edgewise to axial flight conditions. Based on the data analyzed, there is a nose-up pitching moment encountered in low-speed edgewise flight and a nose-down pitching moment experienced when transitioning to high-speed axial flight due to asymmetric lift between the leading and aft portions of the duct. It is assumed that the pitching moment becomes zero in pure axial flight. A better understanding of this concept has been achieved through analysis of the experimental data sets and generated computational results. It was also determined that knowledge of the pitching moment behavior is essential in properly modeling

a ducted fan system.

It was determined that the rotor collective pitch needed to trim a ducted fan system increases with airspeed, which is contrary to the collective pitch behavior of an open rotor on a conventional helicopter. This result suggests that there is flow turning from the freestream direction to the duct's vertical axis direction that occurs before the plane of the rotor. A flow turning efficiency factor before the rotor, k_{χ_R}, was investigated in a range of values from 0.20 to 0.75. The reduction in the horizontal component of velocity at the rotor at higher k_{χ_R} values, particularly around 0.60, eliminates the translational lift effect normally experienced by an open rotor.

A flow turning efficiency factor from freestream to far-wake flow, k_{χ_∞}, was investigated from a value of 0.20 up to and including a value of 0.90. Even with a large flow turning factor, the results generated remained consistent with the 29-inch UAV experimental wind tunnel data.

7.2 Continuation of Model Development

Further development of a duct pitching moment model would improve the accuracy of the simulation model, extend the range of usable flight speeds, and broaden the spectrum of applicable ducted fan vehicles. An improved pitching moment model may include the duct thrust offset as a function of airspeed, angle of attack, and inflow velocity.

Modifications to the vehicle mass properties, including a more accurate placement of the center of gravity, would help refine the simulation model. Improvement of the fuselage drag model, including more accurate values for the fuselage aerodynamic center relative to the vehicle center of gravity, may also improve the accuracy of the simulation model, especially at high airspeeds.

Configuring vane deflection bias to be a function of rotor speed or collective, for example, would allow the vanes to better conform with the swirl component of the exit flow. This would help correct vane stall issues and expand the flight envelope of the vehicle. Another possibility would be to model stators before the control vanes to reduce the swirl effect.

Incorporating the generic ducted fan model into a simulator facility would

enable the model to be analyzed in a real-time simulation environment. This would allow maneuvering flight to be experienced visually, and aid in the development of a more advanced control system.

Appendix A

Supplementary Material

A.1 Experimental Data

A.1.1 29-Inch Ducted Fan UAV Wind Tunnel Data

Figures A.1 through A.7 were used in the model correlation studies presented in Chapter 4.

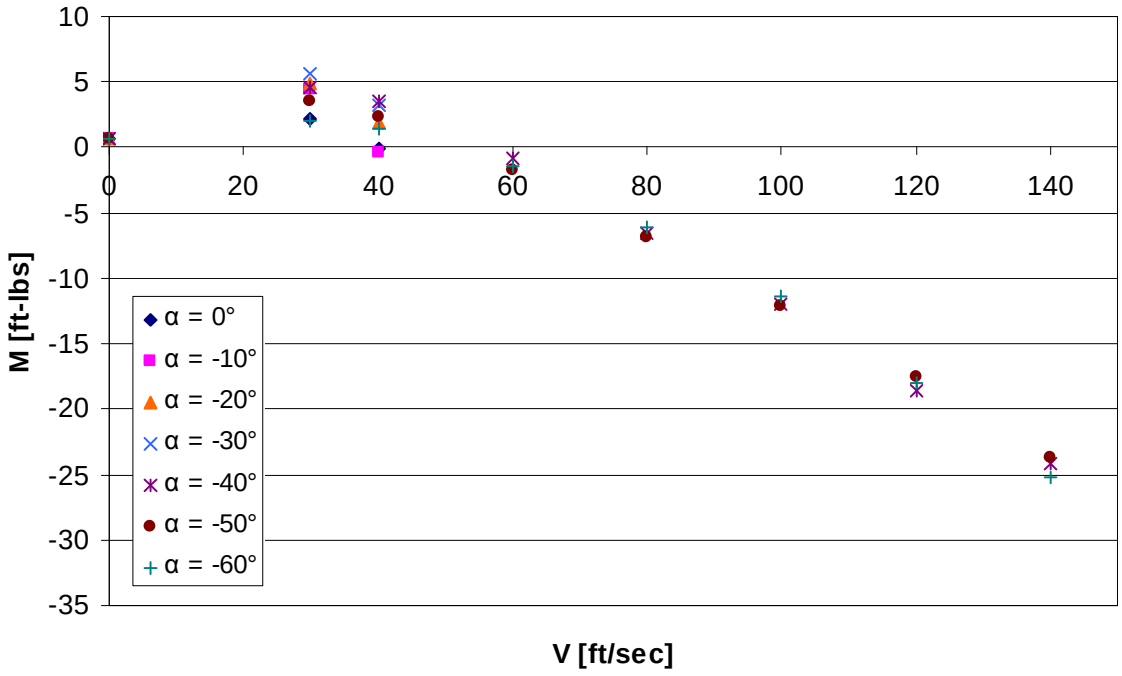

Figure A.1. 29-Inch UAV Pitching Moment vs Airspeed ($\Omega = 5500$ RPM).

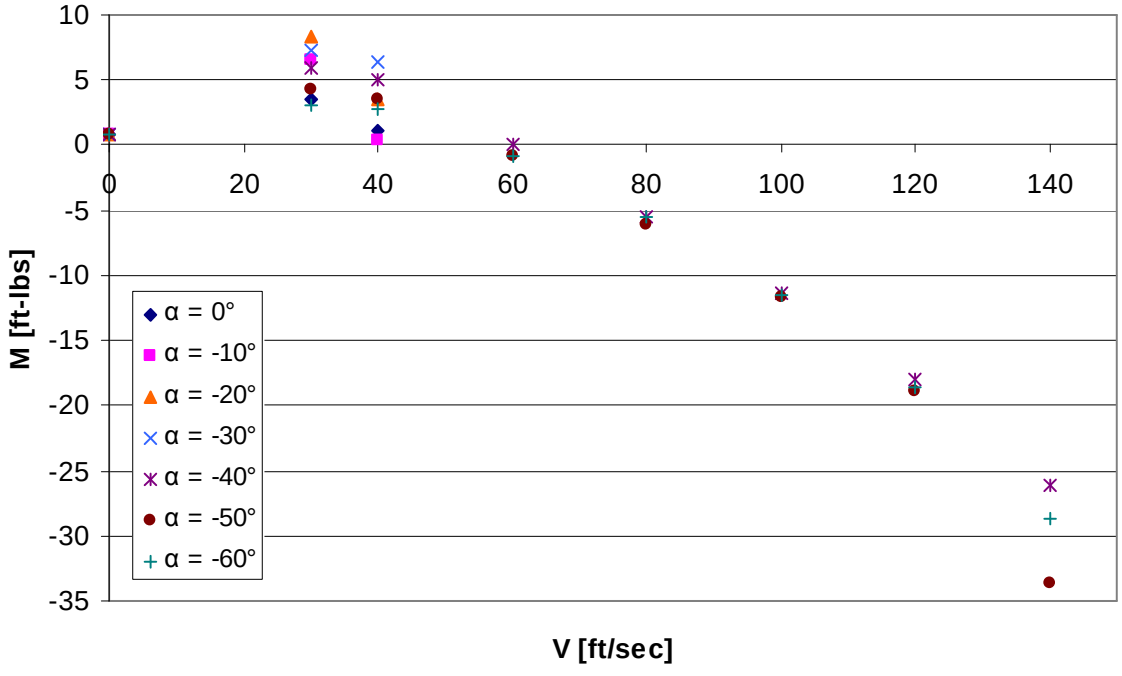

Figure A.2. 29-Inch UAV Pitching Moment vs Airspeed ($\Omega = 6000$ RPM).

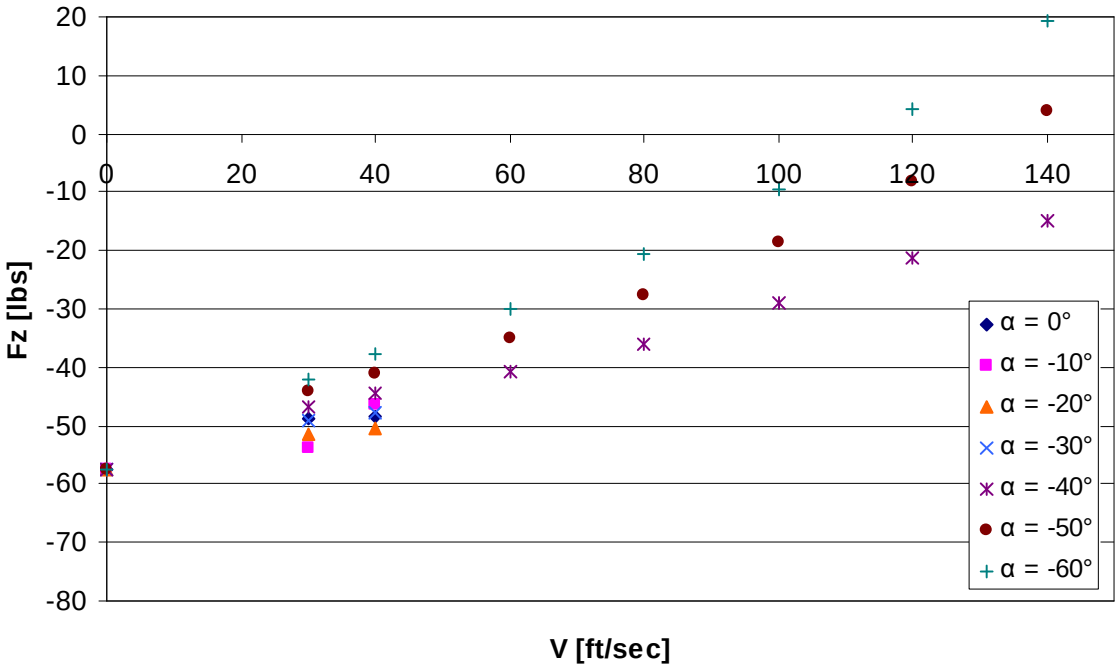

Figure A.3. 29-Inch UAV Axial Force vs Airspeed (Ω = 5500 RPM).

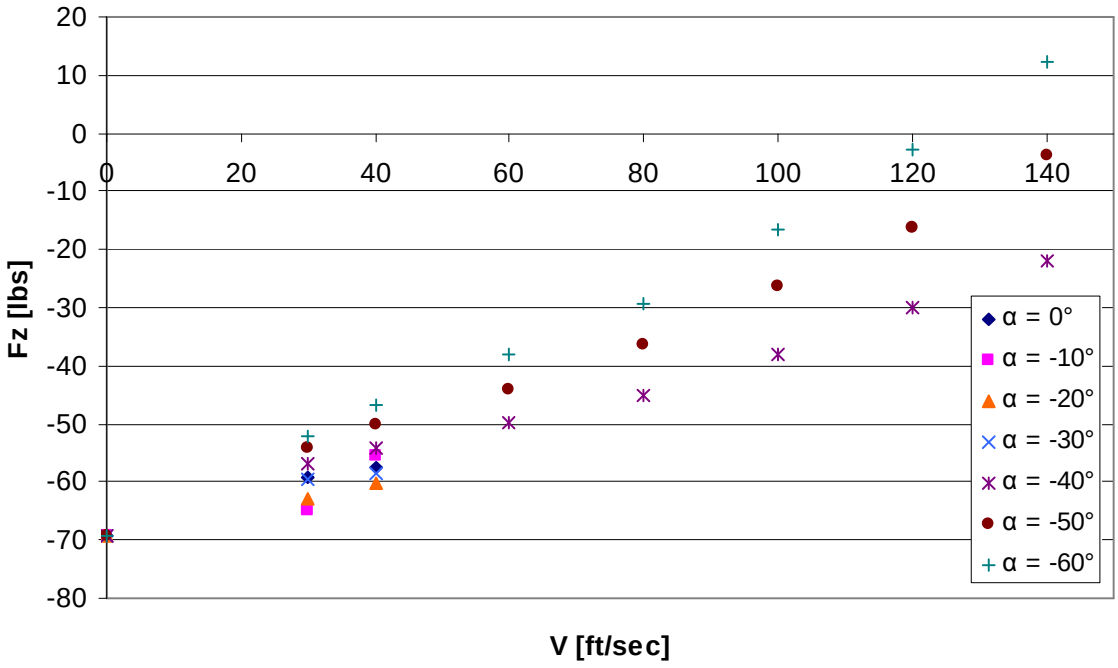

Figure A.4. 29-Inch UAV Axial Force vs Airspeed (Ω = 6000 RPM).

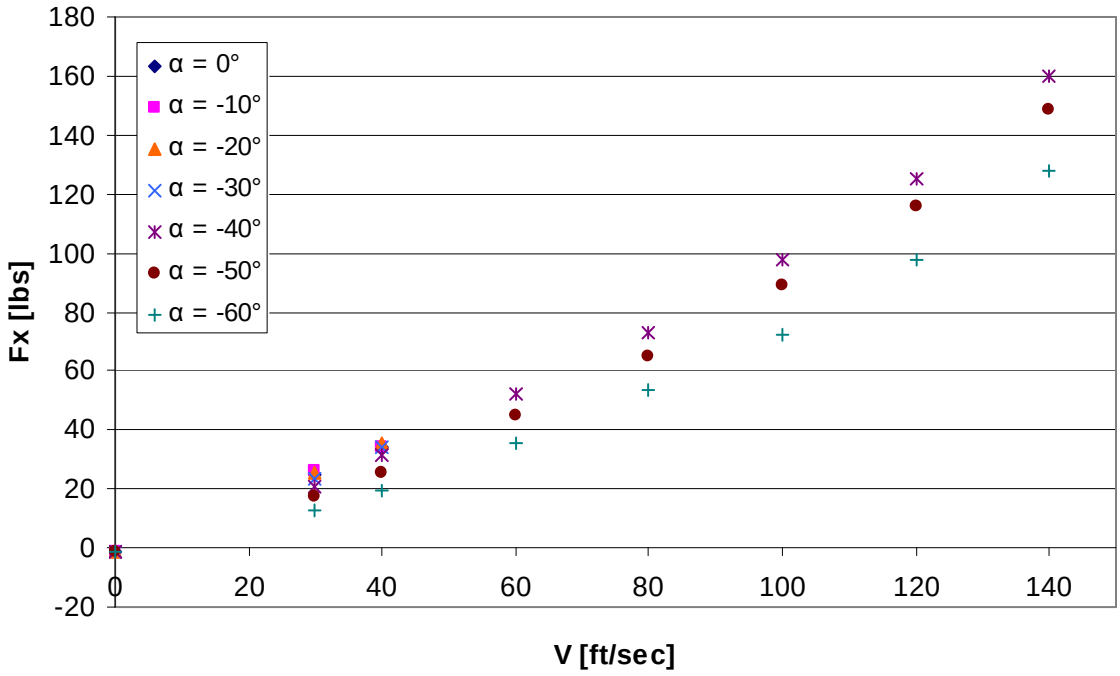

Figure A.5. 29-Inch UAV Normal Force vs Airspeed (Ω = 5500 RPM).

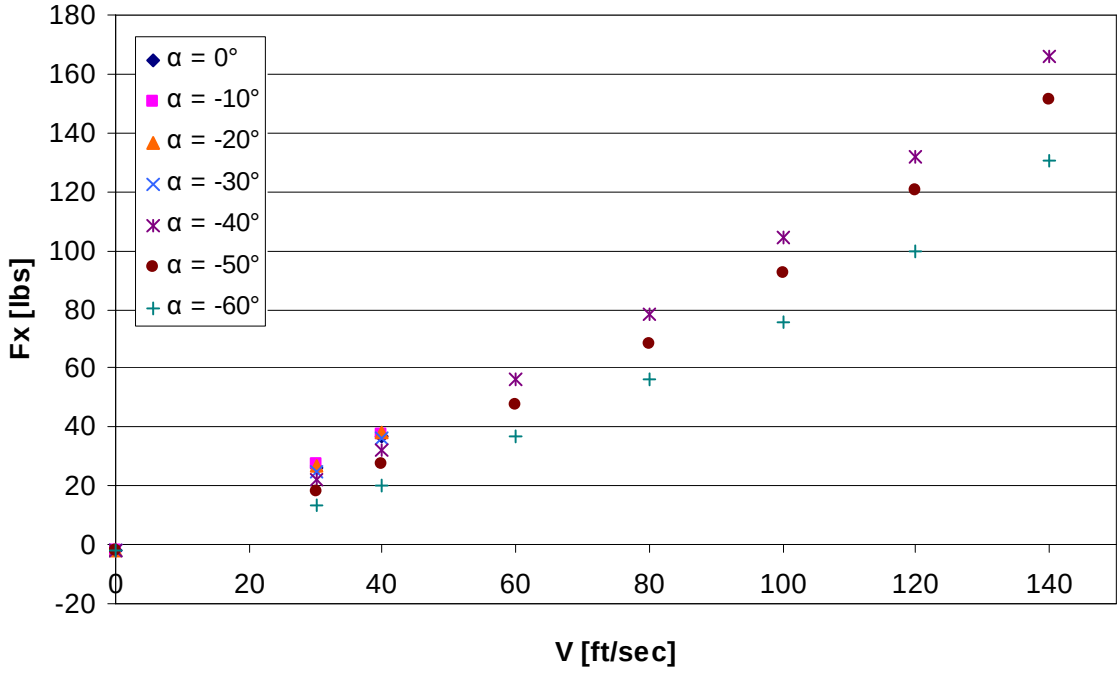

Figure A.6. 29-Inch UAV Normal Force vs Airspeed (Ω = 6000 RPM).

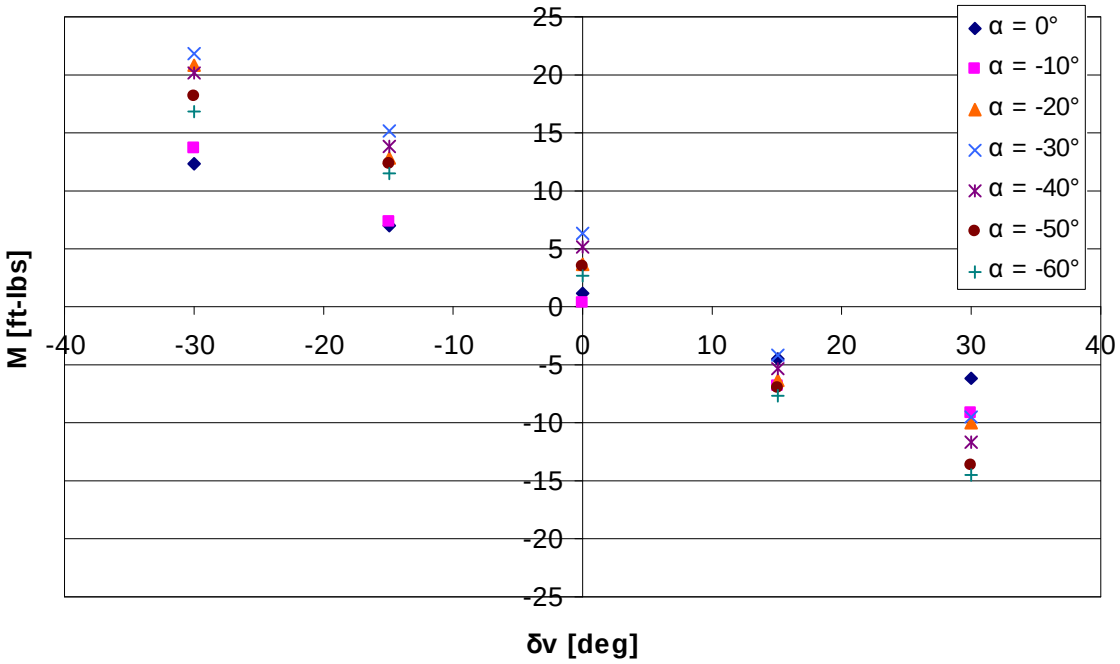

Figure A.7. 29-Inch UAV Pitching Moment vs Longitudinal Vane Deflection ($V = 40\ ft/s$).

A.2 Analytical Results

A.2.1 Generic Ducted Fan Simulation Results

The results presented in this section were generated using the small single ducted fan configuration as described in Section 2.5.1. The results are also shown in the model correlation studies in Chapter 4.

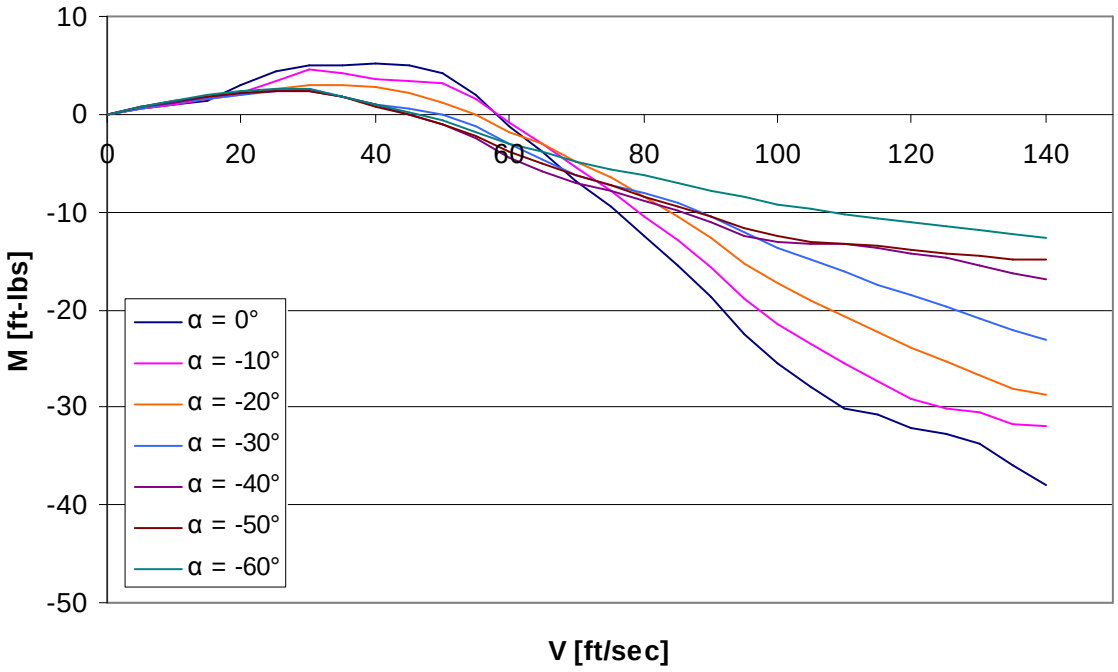

Figure A.8. Generic Ducted Fan Pitching Moment vs Airspeed (Ω = 5500 RPM).

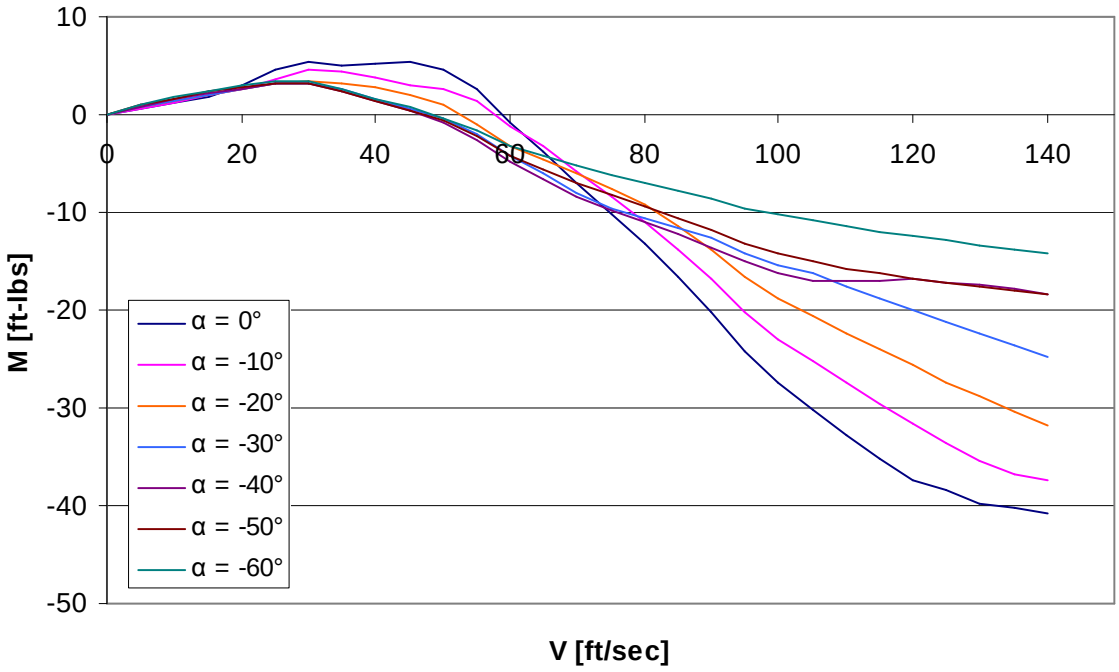

Figure A.9. Generic Ducted Fan Pitching Moment vs Airspeed (Ω = 6000 RPM).

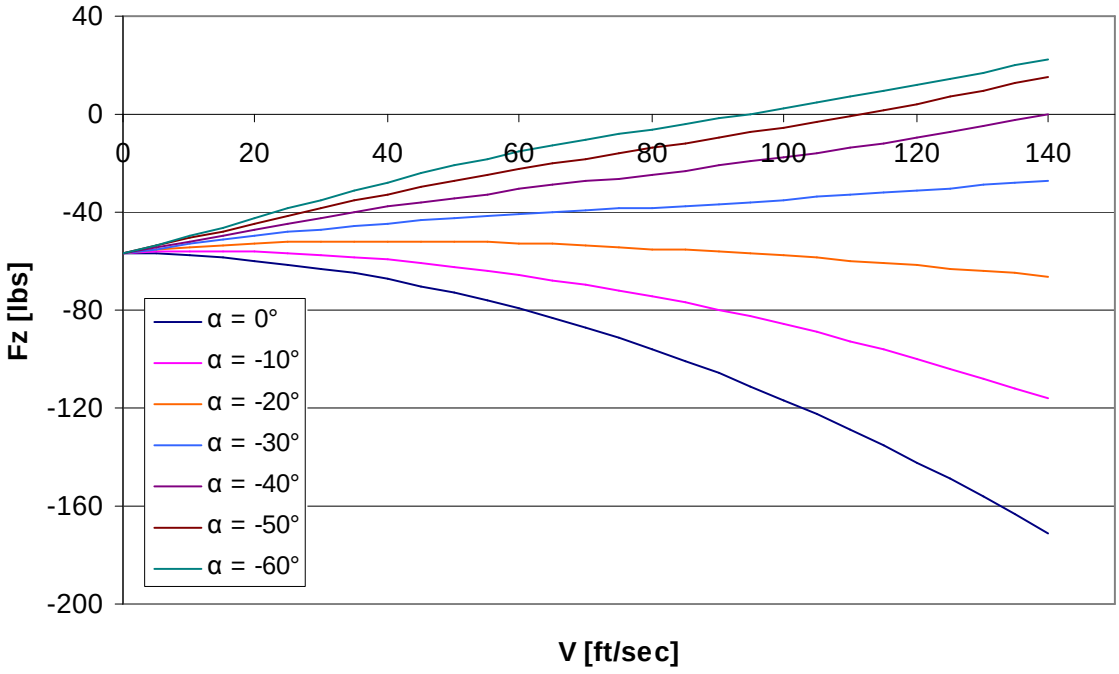

Figure A.10. Generic Ducted Fan Axial Force vs Airspeed (Ω = 5500 RPM).

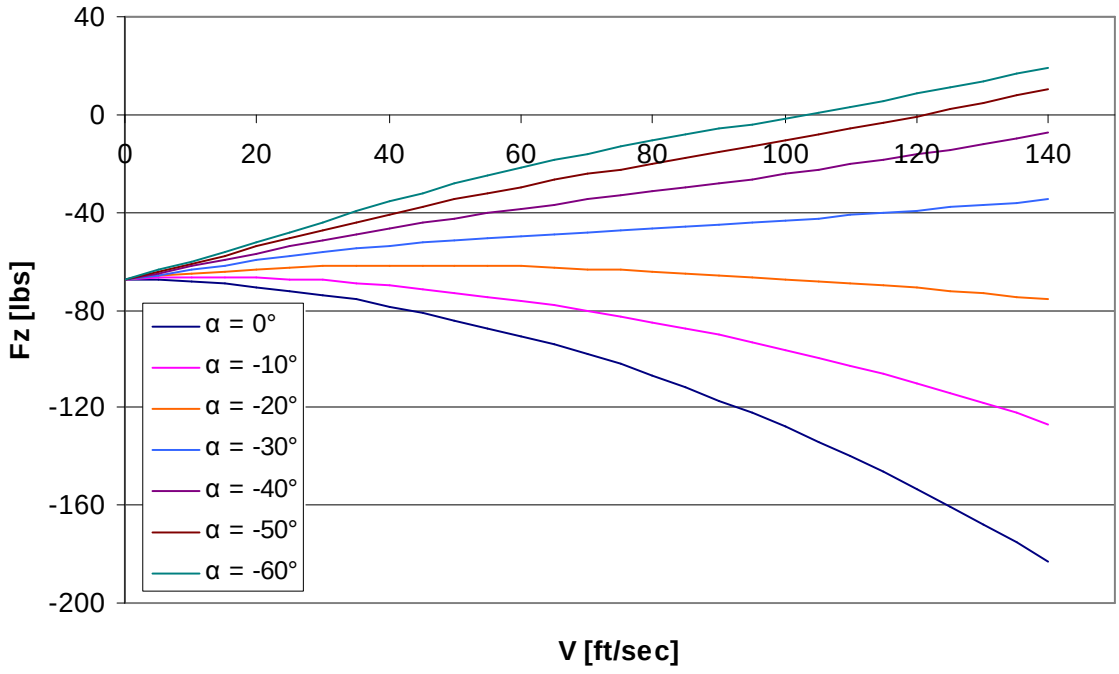

Figure A.11. Generic Ducted Fan Axial Force vs Airspeed (Ω = 6000 RPM).

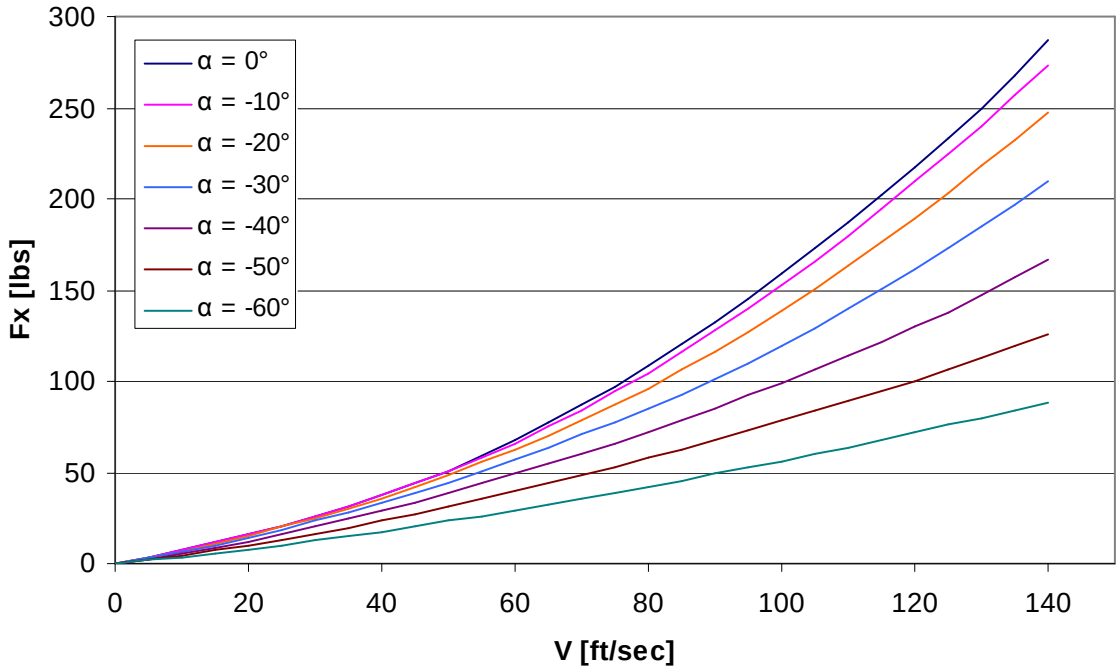

Figure A.12. Generic Ducted Fan Normal Force vs Airspeed (Ω = 5500 RPM).

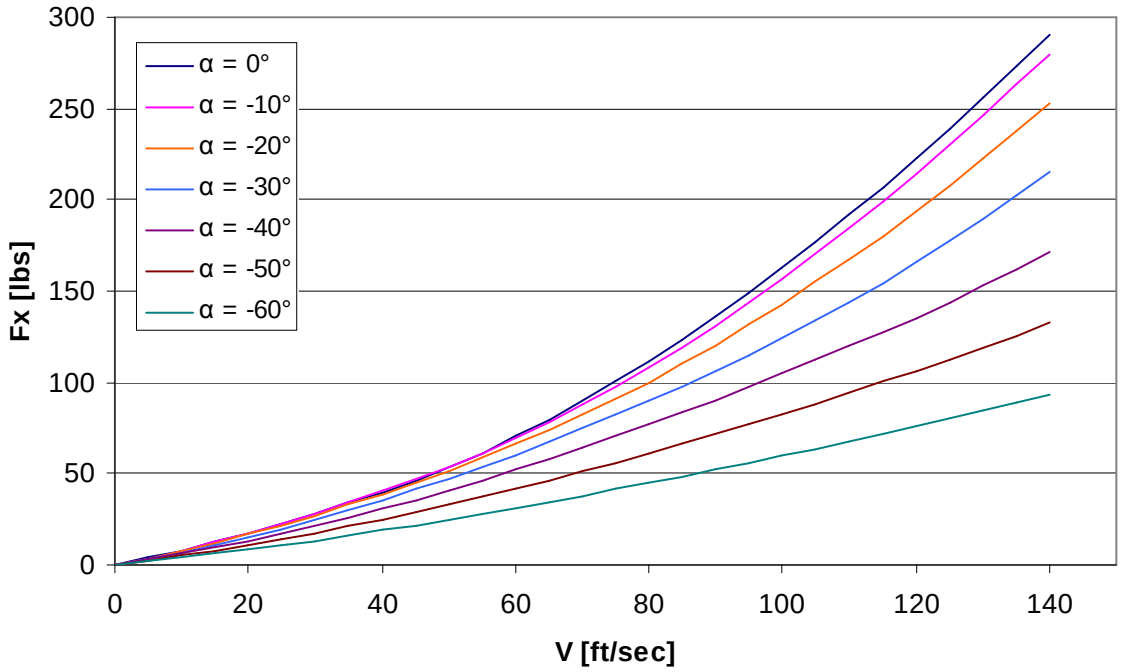

Figure A.13. Generic Ducted Fan Normal Force vs Airspeed (Ω = 6000 RPM).

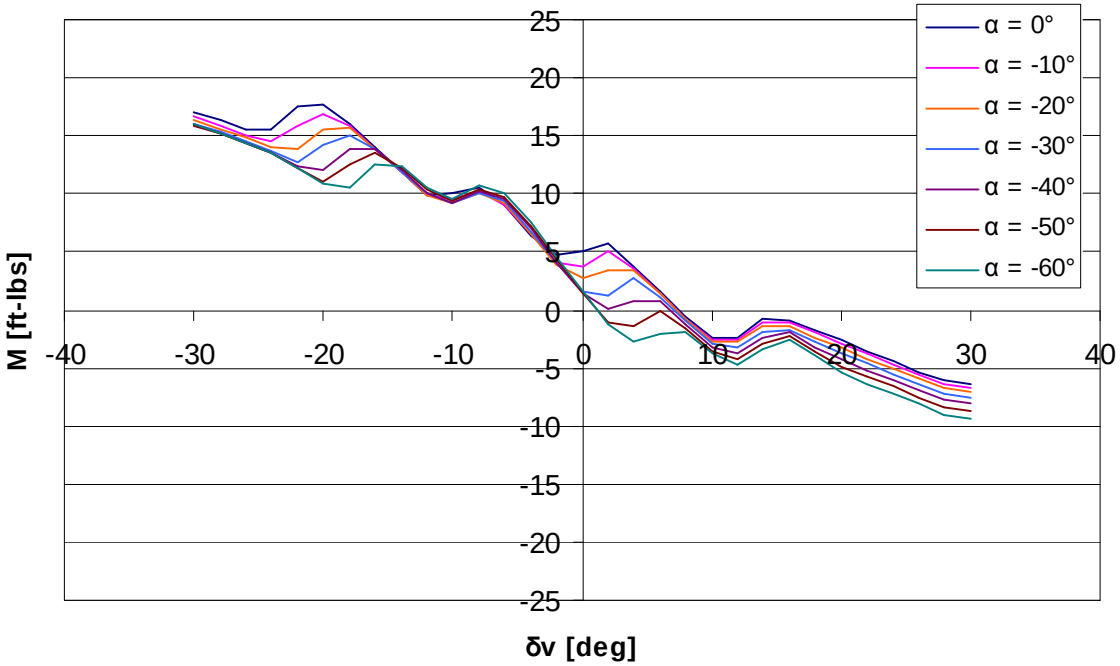

Figure A.14. Generic Simulation Pitching Moment vs Longitudinal Vane Deflection ($V = 40\ ft/s$).

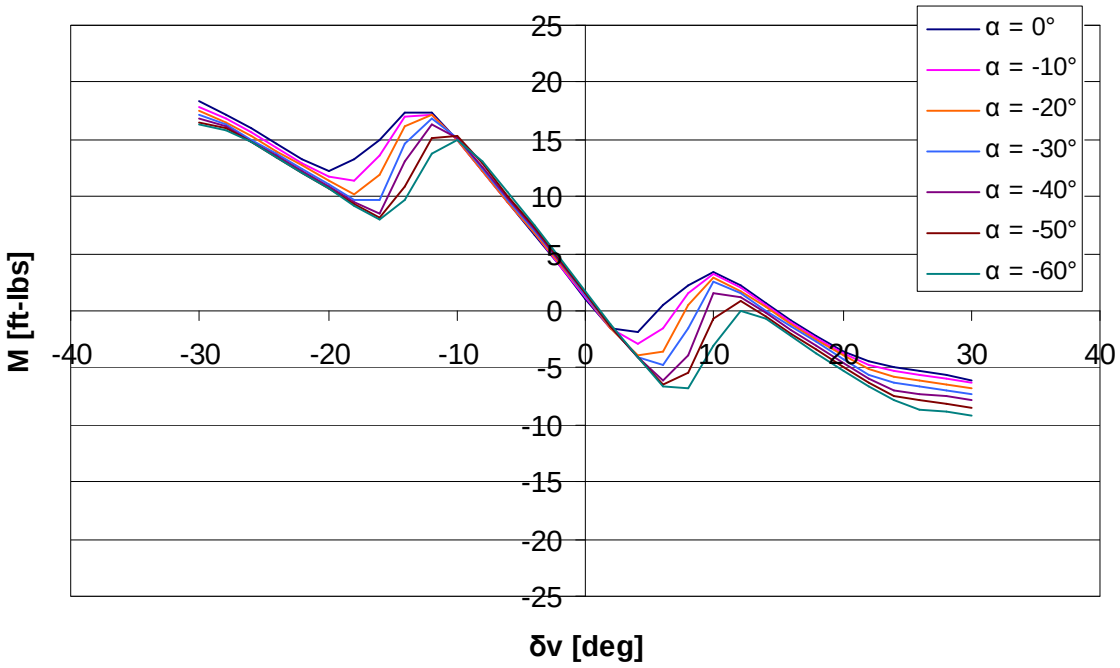

Figure A.15. Generic Simulation Pitching Moment vs Longitudinal Vane Deflection with 5° Vane Deflection Bias ($V = 40\ ft/s$).

A.2.2 FLIGHTLAB Step Input Response Tests

Figures A.16 through A.19 are results of control step response tests performed in order to validate the control mixing utilized in the FLIGHTLAB model, as described in Section 3.3.

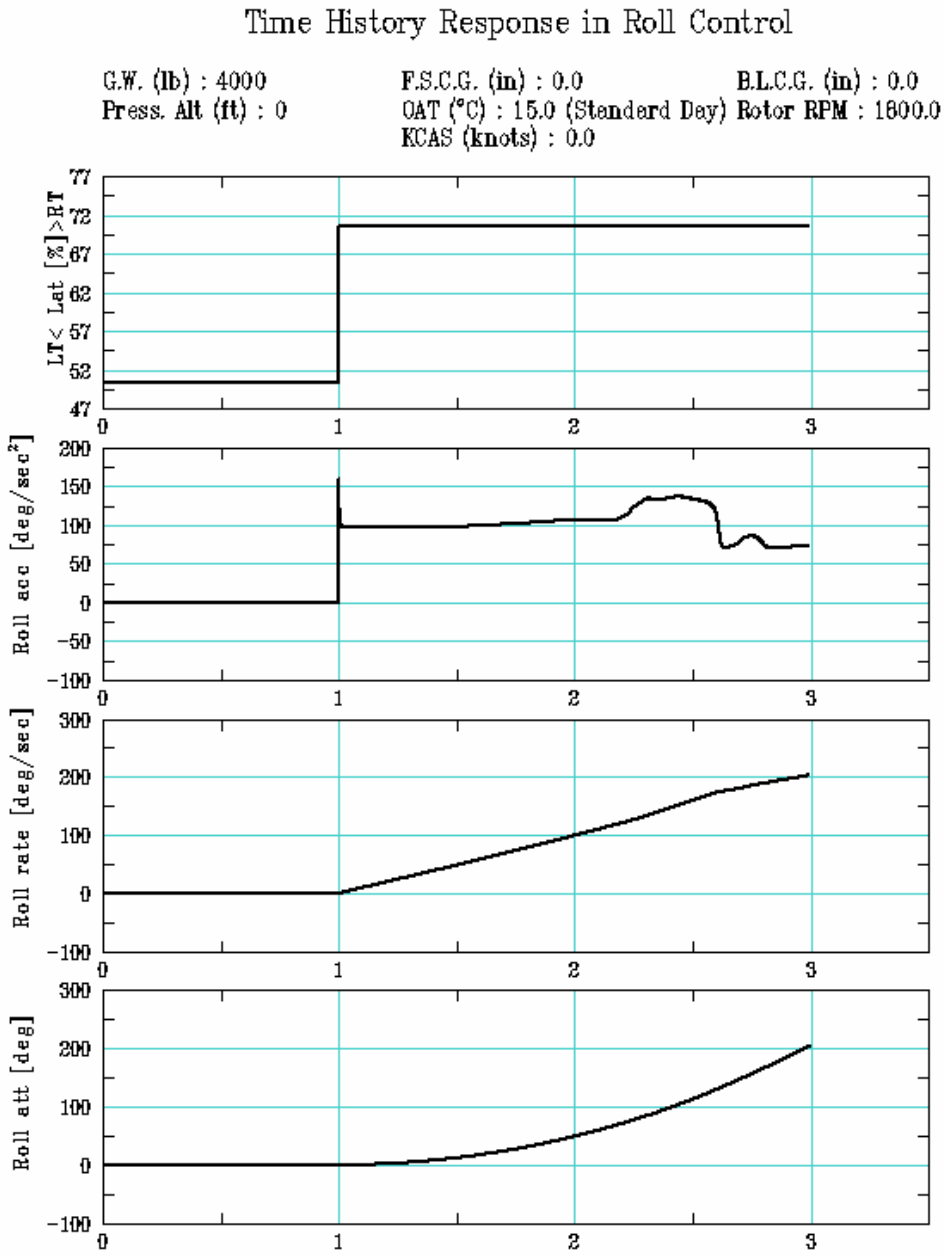

Figure A.16. FLIGHTLAB Roll Response to Lateral Stick Step Input in Hover.

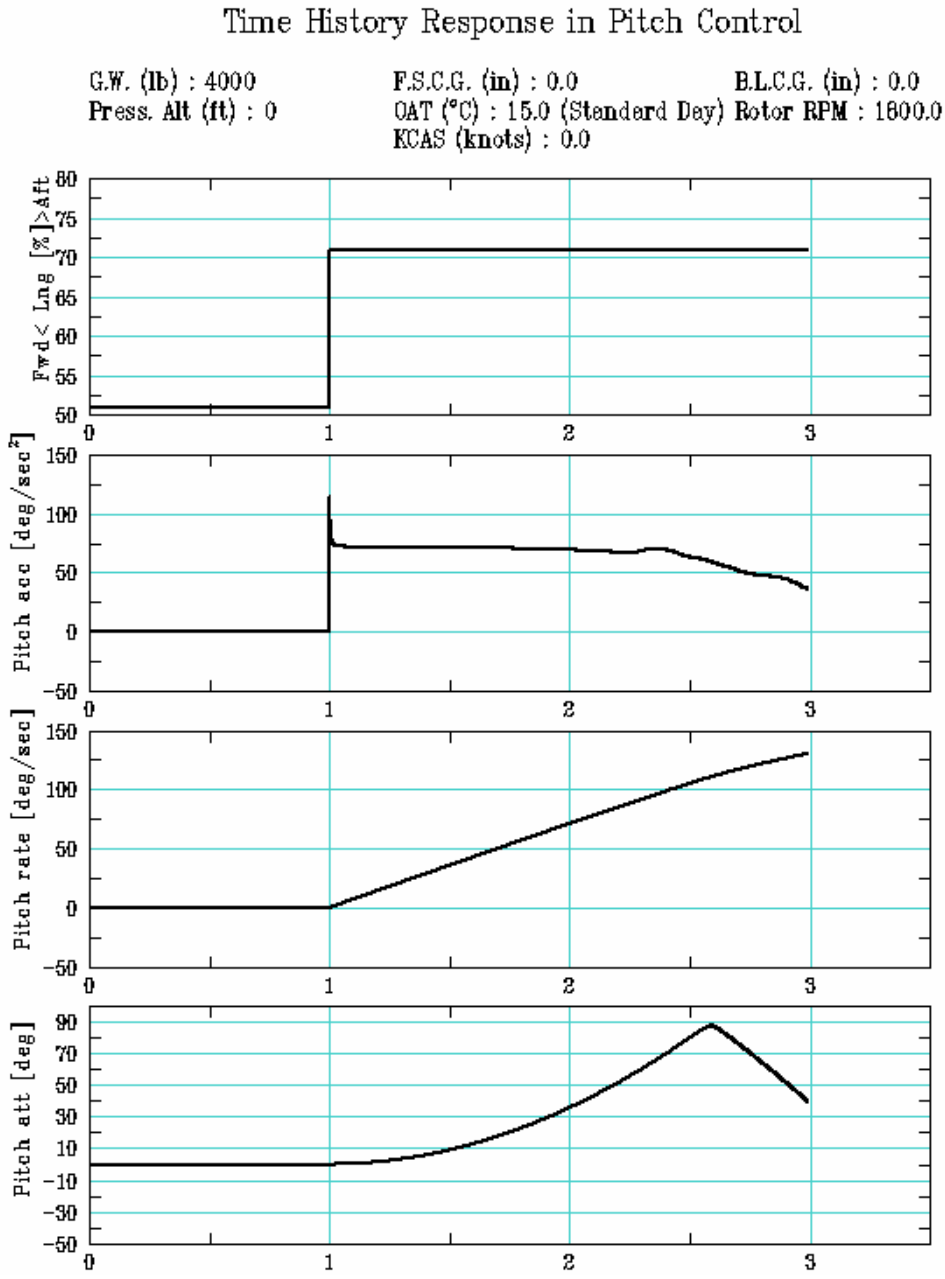

Figure A.17. FLIGHTLAB Pitch Response to Longitudinal Stick Step Input in Hover.

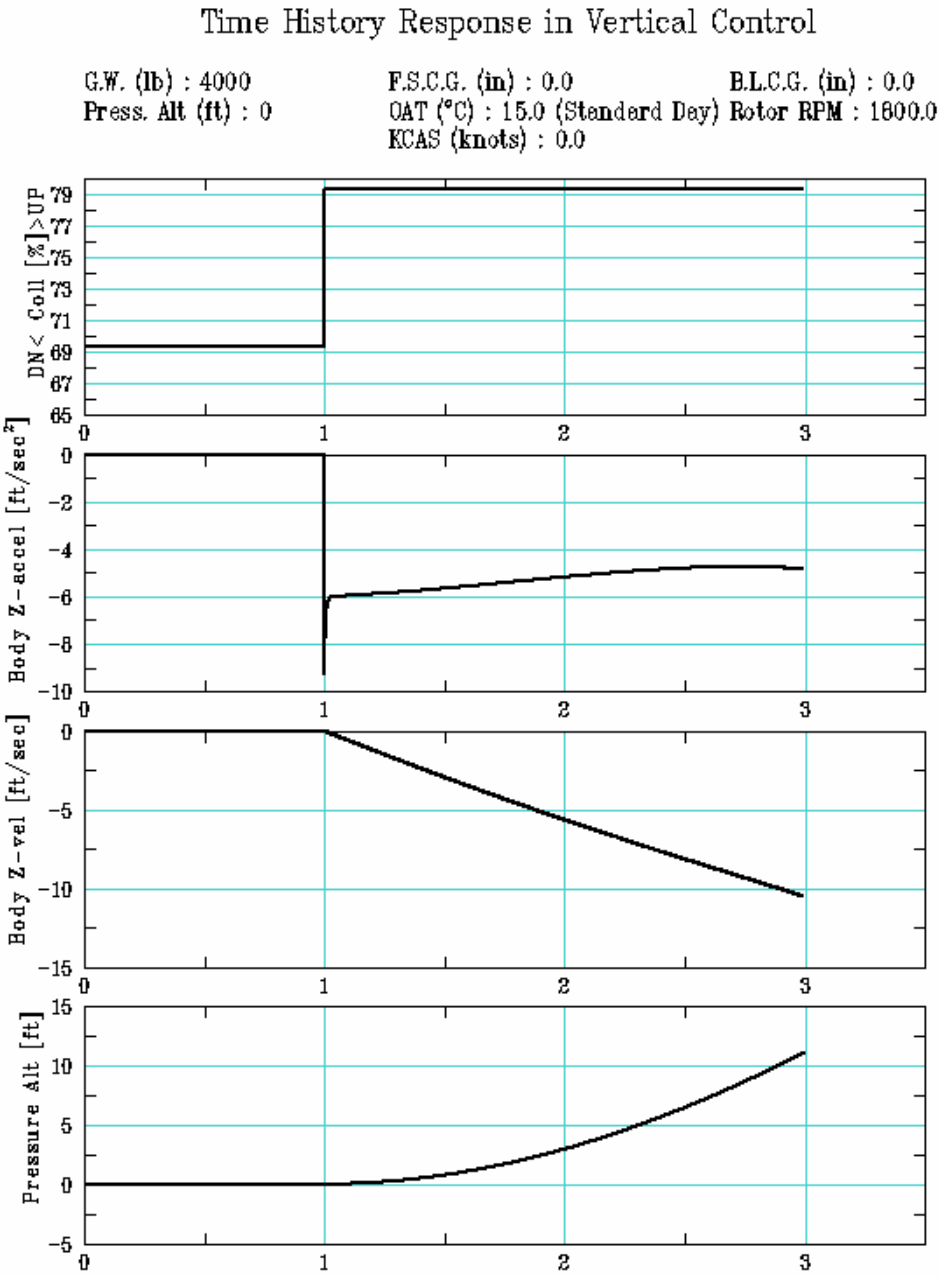

Figure A.18. FLIGHTLAB Heave Response to Collective Stick Step Input in Hover.

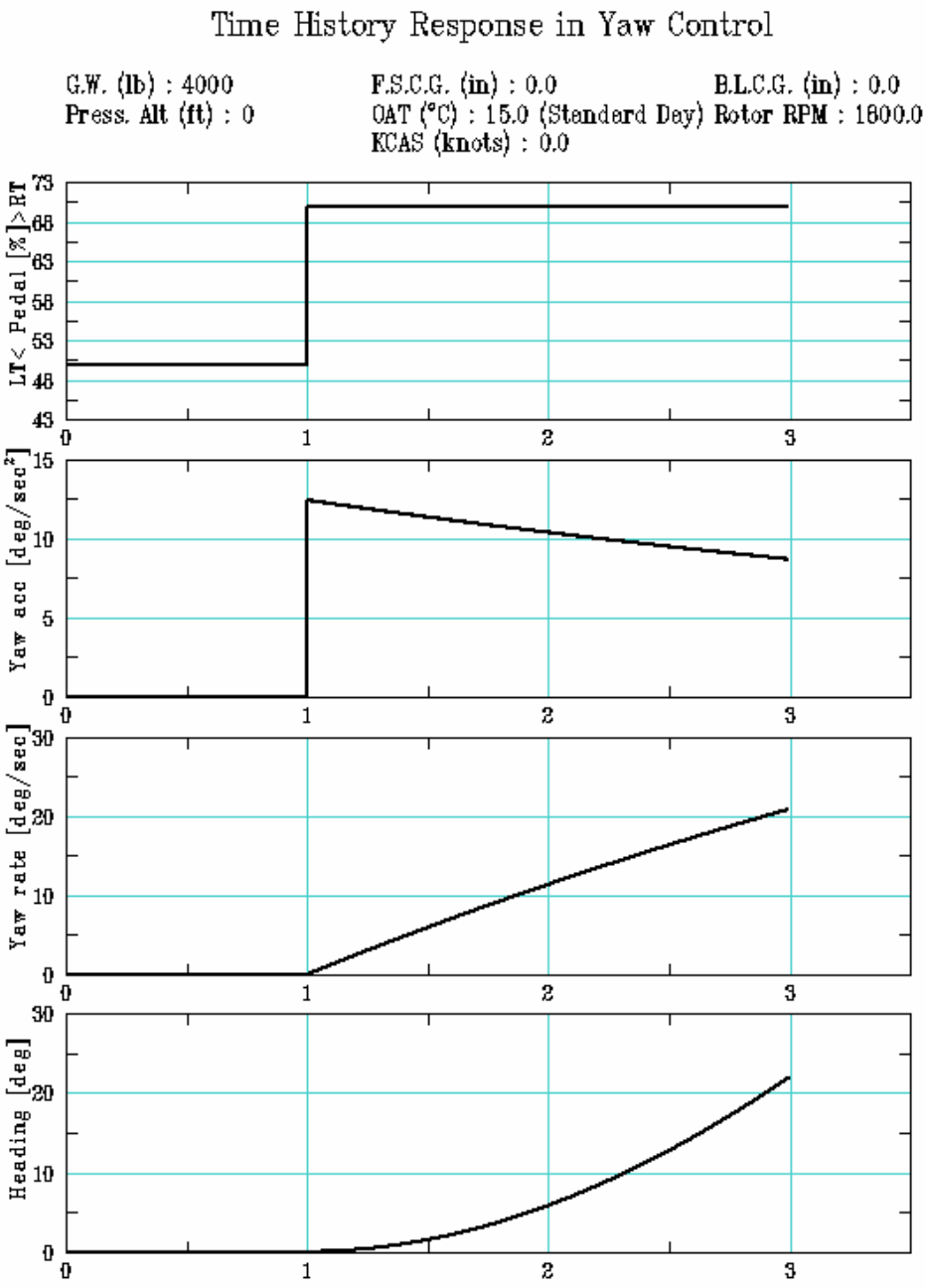

Figure A.19. FLIGHTLAB Yaw Response to Pedal Step Input in Hover.

Appendix B

MATLAB Code

```
function ductfan_init_large_tandem

global  INIT VISC RHO RADIUS CHORD NB RCO BTL HROT XROT YROT ISHAFT ...
    TWIST IDIRROT RETAB ALTAB CLTAB CDTAB D2R R2D DELT PSIV SV VANEFF ...
    XVANE YVANE ZVANE NVANES CHORDV CLVTAB CDVTAB ALVTAB REVTAB DELDRAG ...
    DXCG DYCG DZCG OMEGAREF G MASS IX IY IZ IXZ NROTORS NSTATES ...
    NFSTATES NRSTATES NCTRLS TRIMVARS XSCALE DELXLIN DELCLIN VXTRIM ...
    VYTRIM VZTRIM IUNITS CONTROL0;

IUNITS = 1;

%Time step
DELT = 0.01;
%Constants
D2R = pi/180.;
R2D = 180./pi;
%Atmospheric propeties
RHO = 0.002377;
VISC = 3.62e-7;

%Mass properties
%Accel. due to gravity [ft/s^2]
G = 32.174;
%Weight [lbs]
weight = 4000.;
```

```
%Aircraft Mass [slugs]
MASS = weight/G;
%Moments of Inertia [slug-ft^2]
IX = 1208.0;
IY = 5208.0;
IZ = 6083.0;
IXZ = 0.0;

%Rotor properties
NROTORS = 2;
RADIUS = 4.0; % [ft]
OMEGAREF = 188.5; % [rad/sec]
DCHORD = 4.0; % duct chord length [ft]
CHORD = 0.6; %Blade chord [ft]
RCO = 0.5; % Root cutout [ft]
NB = 6; % number of blades
BTL = 0.98; % nominal tip loss factor
XROT = [6.; -6.]; %Rotor center position rel. to fuse center [ft]
HROT = [0.; 0.];
YROT = [0.; 0.];
ISHAFT = [0.; 0.]; % shaft incidence
TWIST = -10.; % blade twist (deg)
IDIRROT = [1; -1]; % direction of rotation, 1 CCW, -1 CW, 0 Counter Rotating
%This script definmes NACA0012 airfoil data
naca0012;

%Vane propeties
NVANES = 4;
VANEFF = 1; % vane efficiency factor
%Initialize vane properties
PSIV = zeros(NVANES,NROTORS); %Azimuthal location of vanes around the rotor
XVANE = zeros(NVANES,NROTORS); %X-location of center of pressure on vane
                              %relative to the center of the rotor
YVANE = zeros(NVANES,NROTORS); %Y-location " "
ZVANE = zeros(NVANES,NROTORS); %Z-location " "
SV = 6.0*ones(NVANES,NROTORS); %Area of each vane [ft^2]
CHORDV = 1.5*ones(NVANES,NROTORS); %Vane chord [ft]

PSIV(1,1) = 0.;
PSIV(2,1) = 180.;
```

```
PSIV(3,1) = 90.;
PSIV(4,1) = 270.;
PSIV(1,2) = 0.;
PSIV(2,2) = 180.;
PSIV(3,2) = 90.;
PSIV(4,2) = 270.;
XVANE(1,1) = -0.5*RADIUS;
XVANE(2,1) = 0.5*RADIUS;
XVANE(3,1) = 0;
XVANE(4,1) = 0;
YVANE(1,1) = 0;
YVANE(2,1) = 0;
YVANE(3,1) = 0.5*RADIUS;
YVANE(4,1) = -0.5*RADIUS;
ZVANE(1,1) = 3.;
ZVANE(2,1) = 3.;
ZVANE(3,1) = 3.;
ZVANE(4,1) = 3.;
XVANE(1,2) = -0.5*RADIUS;
XVANE(2,2) = 0.5*RADIUS;
XVANE(3,2) = 0;
XVANE(4,2) = 0;
YVANE(1,2) = 0;
YVANE(2,2) = 0;
YVANE(3,2) = 0.5*RADIUS;
YVANE(4,2) = -0.5*RADIUS;
ZVANE(1,2) = 3.;
ZVANE(2,2) = 3.;
ZVANE(3,2) = 3.;
ZVANE(4,2) = 3.;

%NACA0012 properties used for vanes as well
CLVTAB = CLTAB;
CDVTAB = CDTAB;
ALVTAB = ALTAB;
REVTAB = RETAB;
%Rotor airfoil drag increment
DELDRAG = 0.0;
```

```
%C.G. location
DXCG = 0.;
DYCG = 0.;
DZCG = 0.;

%Number of state variables for fuselage degrees of freedom, rotor,
%propulsion system, and controls.
NFSTATES = 12;
NRSTATES = 2;
NSTATES = NFSTATES+NRSTATES;
%Number of controls
NCTRLS = 4;

%INDEX OF STATE VARIABLES
%Fuselage States
IDXF = [1:NFSTATES];
%Rotor States
IDXR = [NFSTATES+1:NFSTATES+NRSTATES];

%Initialize guess of states
xf = zeros(NFSTATES,1);
u0 = [50.;50.;50.;50.];
%Initial guess for trim solution
xf(1) = VXTRIM;
xf(2) = VYTRIM;
xf(3) = VZTRIM;
xr = [45.;45.];
x0 = [xf;xr];

%Set up trim variables
%State scale factors - used to weight relative value of state variables
%for trim and numerical integration
XSCALE = 1./[1. 1. 1. 57.3*ones(1,6) 1. 1. 1. 1. 1.]';

%Perturbations for trim and linearization
DELCLIN = [1. 1. 1. 1.];
DELXLIN = 0.1*XSCALE;
%Define Trim Variables
TRIMVARS = [1:8 IDXR NSTATES+1:NSTATES+NCTRLS];
```

```
INIT = 1;
%Run trim
current_aircraft = 'tandemDuctedfan';
[x0_new,u0_new,itrim] = trimmer(current_aircraft,x0,u0);
x0 = x0_new;
u0 = u0_new;

X0IC = x0;
CONTROL0 = u0;
xf = x0(IDXF);
XF0IC = x0(IDXF);
xr = x0(IDXR);
XR0IC = x0(IDXR);
current_aircraft = 'tandemDuctedfan';
```

```
function [F,M,Qr,xrdot] = ductfan_vec(xf,xr,omega_vec,theta0_vec,
                                      theta1s_vec,theta1c_vec,deltav,irotor)

%Ducted fan model
%Inputs:
%xf  =  fuselage states
%xr  =  rotor states
%omega  =  rotor speed
%theta0  =  collectiuve pitch
%theta1s,theta1c =  cyclic pitch
%deltav  =  vane deflections
%irotor  =  rotor index, for multiple rotors

global INIT VISC RHO RADIUS CHORD NB RCO BTL HROT XROT YROT ISHAFT ...
    TWIST IDIRROT RETAB ALTAB CLTAB CDTAB D2R R2D PSIV SV VANEFF XVANE ...
    YVANE ZVANE NVANES CHORDV CLVTAB CDVTAB ALVTAB REVTAB DELDRAG DXCG ...
    DYCG DZCG AD;
persistent NR NPSI DR RSEG DPSI TSHAFT KAUG KCHI KCHI_R VTAB DXTDTAB ...
    KVINDRAG TAUINFLOW INFLOW_MODEL;

%Initialize
if (INIT == 1)
    %Inflow Model Version (select 1 or 2)
    INFLOW_MODEL = 2;

    %Define radial blade elements (use equal annular areas)
    NR = 6;
    DR = zeros(NR,1);
    RSEG = zeros(NR,1);
    AnnularArea = pi*(RADIUS^2-RCO^2)/NR;
    RSEG(1) = 0.5*RCO+sqrt((0.5*RCO)^2+AnnularArea/(4*pi));
    DR(1) = AnnularArea/(2*pi*RSEG(1));
    for ir = 2:NR;
        rinner = RSEG(ir-1)+0.5*DR(ir-1);
        RSEG(ir) = 0.5*rinner+sqrt((0.5*rinner)^2+AnnularArea/(4*pi));
        DR(ir) = AnnularArea/(2*pi*RSEG(ir));
    end
```

```
  %Define azimuthal step
  NPSI = 24;
  DPSI = 2*pi/NPSI;

  %Disk area
  AD = pi*RADIUS^2;

  %Transformation used for rotor shaft inclination relative to body axes
  cis = cos(ISHAFT(irotor)*D2R);
  sis = sin(ISHAFT(irotor)*D2R);
  TSHAFT = [cis 0 sis; 0 1 0; -sis 0 cis];

  %Max. Thrust Augmentation Factor (augmentation in hover conditions)
  KAUG = 0.4;

  %Turning efficiency of duct (Freestream to infinity, apprev. of KCHI_INF)
  KCHI = 0.85;

  %Portion of total turned flow that is turned before the rotor
  %(e.g. if KCHI_R = KCHI then all the flow is turned before the rotor)
  KCHI_R = 0.60;

  %Empirical duct thrust offset versus airspeed data
  %(for use with pitching moment model)
  VTAB = [0. 5. 10. 15. 20. 25. 30. 35. 40. 45. 50. 55. 60. 65. 70. 75. 80.
          85. 90. 95. 100. 105. 110. 115. 120. 125. 130. 135. 140. 200.];
DXTDTAB = [0.0 0.069 0.138 0.208 0.277 0.346 0.393 0.386 0.363 0.335
           0.288 0.199 0.076 -0.014 -0.105 -0.181 -0.253 -0.324 -0.397
           -0.473 -0.521 -0.549 -0.572 -0.591 -0.605 -0.617 -0.626 -0.634
           -0.639 -0.639];

  %Inflow time constant
  TAUINFLOW = 0.1;

  %Induced drag coefficient of vanes, 1/(pi*e*AR)
  KVINDRAG = 1./(pi*0.8*RADIUS/CHORDV(1,1));

  %Initialize forces, moments, torques to zero
  F = zeros(3,1);
  M = zeros(3,1);
```

```
    Qh = 0.;
    xrdot = 0;
end

theta0 = theta0_vec(irotor);
theta1s = theta1s_vec(irotor);
theta1c = theta1c_vec(irotor);
omega = omega_vec(irotor);

%Location of rotor hub relative to CG
hrot = HROT(irotor)+DZCG;
xrot = XROT(irotor)-DXCG;
yrot = YROT(irotor)-DYCG;

%Parameter represents rotation direction of rotor
idir = IDIRROT(irotor);
SignIdir = sign(idir);
%Define states
u = xf(1);
v = xf(2);
w = xf(3);
p = xf(4);
q = xf(5);
r = xf(6);
vi0 = xr(irotor);
%induced velocity only rotor state for now
%In future will use 3 state Pitt-Peters inflow
%vi1s = xr(2);
%vi1c = xr(3);

%Calculate hub/wind axis velocities and angular rates
Vh = TSHAFT*[(u-q*hrot-r*yrot);(v+p*hrot+r*xrot);w-q*xrot+p*yrot];
Vtot = norm(Vh);
Vinplane = max(sqrt(Vh(1)^2+Vh(2)^2),1e-12);
Vz = -Vh(3);
alphad = atan2(Vz,Vinplane);
cpsiw = Vh(1)/Vinplane;
spsiw = Vh(2)/Vinplane;
psiw = atan2(Vh(2),Vh(1));
```

```
%Wind axis transformation
Tw2h = [cpsiw -spsiw;spsiw cpsiw];

%Shroud pitching moment parameter (x_TD/R)
xtdor = interp1(VTAB,DXTDTAB,Vtot);

%Time averaged integration of forces and moments over rotor disk
%assumes rigid rotor
Tr = 0;
Lr = 0;
Mr = 0;
Qr = 0;
Xr = 0;
Yr = 0;

psi = [0:DPSI:2*pi-DPSI];
spsi = sin(psi);
cpsi = cos(psi);

%Blade pitch
thetab = D2R*(theta0+SignIdir*theta1s*spsi+theta1c*cpsi);
%Tip loss, constant for now, can be function of stall effects
Btl = BTL*RADIUS*ones(1,NPSI);
%Blade segment pitch
thetaseg = ones(NR,1)*thetab+TWIST*D2R*((RSEG-RCO)/(RADIUS-RCO))*ones(1,NPSI);
chifact1 = (KCHI^2-2*KCHI);

if (INFLOW_MODEL == 2)
    VRx = Vtot*cos(alphad+KCHI_R*(pi/2-alphad));
    VRz = Vtot*sin(alphad+KCHI_R*(pi/2-alphad))+vi0;
    VEx = Vtot*cos(alphad+KCHI*(pi/2-alphad));
    VEz = Vtot*sin(alphad+KCHI*(pi/2-alphad))+vi0;
else
    VRx = Vinplane*(1.-KCHI_R);
    VRz = Vz+vi0;
    VEx = Vinplane*(1.-KCHI);
    VEz = VRz;
end
```

```
%Magnitude of velocity at rotor
Vr = sqrt(VRx^2+VRz^2);
%Perpindicular
Vp = -VRz+RSEG*(p*spsi+q*cpsi);
%Tangential
%(note term (spsi*cpsiw+cpsi*spisw) acounts for direction of relative
%wind.  SignIdir accounts for direction of rotation.
Vt = RSEG*(omega-SignIdir*r)+VRx*ones(size(RSEG))
     *(spsi*cpsiw+cpsi*spsiw*SignIdir);

%Velocity and angle of attack and Re #
Vseg = sqrt(Vp.^2+Vt.^2);
alphaseg = mod(R2D*(thetaseg+atan2(Vp,Vt)),360);
Renumseg = max(RHO*Vseg*CHORD/VISC,160000);
Renumseg = min(Renumseg,5e6);

%Tip Loss Factor
tlfactor = (ones(NR,1)*Btl-(RSEG-0.5*DR)*ones(1,NPSI))./(DR*ones(1,NPSI));
tlfactor = max(min(tlfactor,1.),0.);

% CL and CD table lookup for all blade elements at each azimuth location
Clseg = interp2(RETAB,ALTAB,CLTAB,Renumseg,alphaseg).*tlfactor;
Cdseg = interp2(RETAB,ALTAB,CDTAB,Renumseg,alphaseg)+DELDRAG;
Fpseg = 0.5*RHO*CHORD*(DR*ones(1,NPSI)).*Vseg.*(Clseg.*Vt+Cdseg.*Vp);
Ftseg = 0.5*RHO*CHORD*(DR*ones(1,NPSI)).*Vseg.*(Cdseg.*Vt-Clseg.*Vp);

%Sum forces and moments over the blade
Fpblade = sum(Fpseg);
Ftblade = sum(Ftseg);
Mfblade = sum(Fpseg.*(RSEG*ones(1,NPSI)));
Mlblade = sum(Ftseg.*(RSEG*ones(1,NPSI)));

%Time averaged forces and moments of rotor
Lr = sum(-SignIdir*(Mfblade.*spsi))*NB/NPSI;
Mr = sum(Mfblade.*cpsi)*NB/NPSI;
Qr = sum(Mlblade)*NB/NPSI;
Tr = sum(Fpblade)*NB/NPSI;
Xr = sum(-Ftblade.*spsi)*NB/NPSI;
Yr = sum(-SignIdir*(Ftblade.*cpsi))*NB/NPSI;
```

```
%Total thurst
Tduct = KAUG*Tr;
T = Tduct+Tr;

%Momentum Drag (Ram Drag)
if (INFLOW_MODEL == 2)
    Dm = RHO*AD*Vr*(cos(alphad)-cos(alphad+0.5*(-2*alphad+pi)*KCHI))*Vtot;
else
    Dm = RHO*AD*Vr*KCHI*Vinplane;
end

%Inflow Calculation
augfact = 1./(1+KAUG);
viqs = vi0;
infloweqn = 999.;
iter = 0;
iter_max = 100;
%Iterate to get quasi-steady inflow.
if (INFLOW_MODEL == 2)
    while ( abs(infloweqn)>0.0001 && iter<iter_max )
      inflowfact1 = sin(alphad+KCHI_R*(pi/2-alphad));
      inflowfact2 = sin(alphad+KCHI*(pi/2-alphad));
      infloweqn = T/(RHO*AD*sqrt(viqs^2+2*inflowfact1*viqs*Vtot+Vtot^2))
      -augfact*(viqs-sin(alphad)*Vtot+inflowfact1*Vtot-sin(alphad)
      *KAUG*Vtot+0.5*sqrt(8*(-sin(alphad)+inflowfact2)*(1+KAUG)*Vtot*
      (viqs+inflowfact1*Vtot)+4*(viqs+(inflowfact1-inflowfact2-
      inflowfact2*KAUG)*Vtot)^2));
      dinfdvi = -T*(viqs+inflowfact1*Vtot)/(RHO*AD*(sqrt(viqs^2+2*inflowfact1
      *viqs*Vtot+Vtot^2))^3)-augfact*(1+0.5*(8*(viqs+(inflowfact1-inflowfact2
      -inflowfact2*KAUG)*Vtot)+8*(1+KAUG)*Vtot*(inflowfact2-sin(alphad)))
      /(2*sqrt(4*(viqs+(inflowfact1-inflowfact2-inflowfact2*KAUG)*Vtot)^2
      +8*(1+KAUG)*Vtot*(viqs+inflowfact1*Vtot)*(inflowfact2-sin(alphad)))));
      del_vi = -(1./dinfdvi)*infloweqn;
      viqs = viqs+0.5*del_vi;
      iter = iter+1;
    end
else
    while ( abs(infloweqn)>0.0001 && iter<iter_max )
      inflowfact = (KAUG*Vz-viqs)/(1+KAUG);
      infloweqn = Vr*(  -inflowfact+sqrt(inflowfact^2-chifact1*Vinplane^2))
```

```
      -T/(RHO*AD);
      dinfdvi = (Vz+viqs)*viqs/Vr +  ...
      Vr*(augfact+((-KAUG*Vz+viqs)*augfact^2 )/sqrt((-KAUG*Vz+viqs)^2*augfact^2
      -chifact1*Vinplane^2));
      del_vi = -(1./dinfdvi)*infloweqn;
      viqs = viqs+0.5*del_vi;
      iter = iter+1;
    end
end
xrdot = 1./TAUINFLOW*(viqs-vi0);

%Vane forces and moments
Xv = 0.;
Yv = 0.;
Zv = 0.;
Lv = 0.;
Mv = 0.;
Nv = 0.;

%Swirl angular velocity
omega_swirl = Qr/(RHO*AD*Vr*0.5*RADIUS^2)*SignIdir;
for iv = 1:NVANES;
    %Vane center of pressure position vector
    r_v = [XVANE(iv,irotor);YVANE(iv,irotor);ZVANE(iv,irotor)];

    %velocity vector in hub-wind axes
    Vv_vec = [VEx*cpsiw;VEx*spsiw;-VEz];
    cpsiv = cos(PSIV(iv,irotor)*D2R);
    spsiv = sin(PSIV(iv,irotor)*D2R);

    %Add swirl component
    Vtheta = omega_swirl*norm(r_v(1:2));
    Vv_vec(1) = Vv_vec(1)-Vtheta*spsiv;
    Vv_vec(2) = Vv_vec(2)-Vtheta*cpsiv;

    %Add angular motion
    Vv_vec = Vv_vec+cross([p;q;r],r_v);
    Vv_tot = norm(Vv_vec);
    qv = 0.5*RHO*Vv_tot^2;
```

```
    %Transformation from hub-wind axes to vane axes
    % uv  =  chordwise vel
    % vv  =  spanwise vel
    % wv  =  norm vel
    Th2v = [0 0 -1;-1 0 0;0 1 0]*[cpsiv -spsiv 0;spsiv cpsiv 0; 0 0 1];
    temp = Th2v*Vv_vec;
    uv = temp(1);
    vv = temp(2);
    wv = temp(3);

    %AOA and sideslip angle of vane
    alphav = atan2(wv,uv);
    betav = asin(vv/Vv_tot);

    %Transform from vane wind axes back to vane axes
    Tw2v = [cos(alphav) 0 -sin(alphav);0 1 0;sin(alphav) 0 cos(alphav)]
    *[cos(betav) -sin(betav) 0;sin(betav) cos(betav) 0; 0 0 1];

    %Lift and drag of vanes
    %deltav defined positive trailing edge deflected in clockwise direction
    Renumv = RHO*Vv_tot*CHORDV(iv,irotor)/VISC;
    Renumv = max(min(Renumv,5e6),160000);
    alphavtab = mod(R2D*alphav-deltav(iv,irotor),360);
    Clv = interp2(REVTAB,ALVTAB,CLVTAB,Renumv,alphavtab)*VANEFF;
    Cdv = interp2(REVTAB,ALVTAB,CDVTAB,Renumv,alphavtab)+KVINDRAG*Clv^2;
    Dvane = Cdv*qv*SV(iv,irotor);
    Lvane = Clv*qv*SV(iv,irotor);
    temp = Tw2v*[-Dvane;0;-Lvane];

    %Transform vane forces and moments into hub axes
    Fvane = Th2v'*temp;
    Mvane = cross(r_v,Fvane);
    Xv = Xv+Fvane(1);
    Yv = Yv+Fvane(2);
    Zv = Zv+Fvane(3);
    Lv = Lv+Mvane(1);
    Mv = Mv+Mvane(2);
    Nv = Nv+Mvane(3);
end
```

```
%Fuselage (duct) drag
[Ff,Mf] = fuselage_drag([u;v;w]);

%Forces and moments in hub system
Fh = zeros(3,1);
Mh = zeros(3,1);
Fh(1) = Xr-Dm*cpsiw+Xv;
Fh(2) = Yr-Dm*spsiw+Yv;
Fh(3) = -T+Zv;
Mh(1) = Lr-Tduct*xtdor*RADIUS*spsiw+Lv;
Mh(2) = Mr+Tduct*xtdor*RADIUS*cpsiw+Mv;
Mh(3) = Qr*SignIdir+Nv;

%Transform to body systems
F = TSHAFT'*Fh+Ff;
M = TSHAFT'*Mh+Mf+cross([xrot;0;-hrot],F);
```

```
function [Ff,Mf] = fuselage_drag(indat)

%Fuselage Drag Model
%Models lift, drag, and side forces on fuselage
%Inputs : Fuselage State Vector, xf
%Outputs: Fuselage Force Vector, Ff
%         Fuselage Moment Vector, Mf

global RHO;

%Aerodynamic center of fuselage
XFUS = 0.;
HFUS = 0.;

%Frontal drag area [ft^2]
D1FUSE = 6.4;
%Vertical drag area [ft^2]
D2FUSE = 0.99;
%Sideward drag area [ft^2]
D3FUSE = 6.4;

%Lift slope [ft^2/radian]
L1FUSE = 0.;
%Side force lift slope [ft^2/radian]
Y1FUSE = 0.;

%Local velcities
uf = indat(1);
vf = indat(2);
wf = indat(3);

%Calculate dynamic pressure, angle of attack (alpha), sideslip angle (beta)
vxy2 = uf^2+vf^2;
vxy = sqrt(vxy2);
Vtot2 = vxy2+wf^2;
qfus = 0.5*RHO*Vtot2;
betaf = atan2(vf,uf);
alphaf = atan2(wf,vxy);
```

```
sa = sin(alphaf);
sa2 = sa^2;
s2a = sin(2*alphaf);
sb = sin(betaf);
sb2 = sb^2;
s2b = sin(2*betaf);
cb = cos(betaf);
cb2 = cb^2;
ca = cos(alphaf);
ca2 = ca^2;

%Formula for drag, lift, and side force equivalent flat plate area
dq = D1FUSE+((D2FUSE-D1FUSE)*sa2+(D3FUSE-D2FUSE-D1FUSE)*sb2*ca2);
lq = 0.5*L1FUSE*s2a*cb2;
yq = -0.5*Y1FUSE*s2b*ca2;

%Transform from wind axes back to body axes
Twf = [cb*ca -sb -cb*sa; sb*ca cb -sb*sa; sa 0. ca];
temp = Twf*[-dq;yq;-lq];

%Scale by dynamic pressure, qfus
Ff = temp*qfus;
%Resolve moments at c.g.
Mf = [0 HFUS 0;-HFUS 0 -XFUS;0 XFUS 0]*Ff;
```

Bibliography

[1] Yoeli, R., "Ducted Fan Utility Vehicles and Other Flying Cars," *Collection of Technical Papers - 2002 Biennial International Powered Lift Conference and Exhibit*, Williamsburg, VA, United States, 2002, pp. 1–6.

[2] Leishman, J. G., *Principles of Helicopter Aerodynamics*, Cambridge University Press, New York, NY, United States, 2nd ed., 2006.

[3] McCormick, B. W., *Aerodynamics of V/STOL Flight*, Dover Publications, Inc., Mineola, NY, United States, 2nd ed., 1999.

[4] Chang, I.-C. and Rajagopalan, R., "CFD Analysis for Ducted Fans with Validation," *Collection of Technical Papers - 21st AIAA Applied Aerodynamics Conference*, Orlando, FL, United States, 2003, pp. 122–136.

[5] Guerrero, I., Gelhausen, P., Myklebust, A., and Londenberg, K., "A Powered Lift Aerodynamic Analysis for the Design of Ducted Fan UAVs," *Collection of Technical Papers - 2nd AIAA Unmanned Unlimited Systems, Technologies, and Operations*, San Diego, CA, United States, 2003, pp. 447–454.

[6] Alpman, E., Long, L., and Kothmann, B., "Understanding Ducted-Rotor Antitorque and Directional Control Characteristics Part II: Unsteady Simulations," *Journal of Aircraft*, Vol. 41, No. 6, 2004, pp. 1370–1378.

[7] Lind, R., Nathman, J., and Gilchrist, I., "Ducted Rotor Performance Calculations and Comparisons with Experimental Data," *Collection of Technical Papers - 44th AIAA Aerospace Sciences Meeting*, Vol. 17, Reno, NV, United States, 2006, pp. 12849–12856.

[8] Avanzini, G., D'Angelo, S., and De Matteis, G., "Performance and Stability of Ducted-Fan Uninhabited Aerial Vehicle Model," *Journal of Aircraft*, Vol. 40, No. 1, 2003, pp. 86–93.

[9] De Divitiis, N., "Performance and Stability Analysis of a Shrouded-Fan Unmanned Aerial Vehicle," *Journal of Aircraft*, Vol. 43, No. 3, 2006, pp. 681–691.

[10] Avanzini, G., Ciniglio, U., and De Matteis, G., "Full-Envelope Robust Control of a Shrouded-Fan Unmanned Vehicle," *Journal of Guidance, Control, and Dynamics*, Vol. 29, No. 2, 2006, pp. 435–443.

[11] Hess, R. and Bakhtiari-Nejad, M., "Sliding Mode Control of a Nonlinear Ducted-Fan UAV Model," *Collection of Technical Papers - AIAA Guidance, Navigation, and Control Conference 2006*, Vol. 2, Keystone, CO, United States, 2006, pp. 748–762.

[12] Spaulding, C., Mansur, M., Tischler, M., Hess, R., and Franklin, J., "Nonlinear Inversion Control for a Ducted Fan UAV," Vol. 2, San Francisco, CA, United States, 2005, pp. 1209–1234.

[13] Johnson, E. and Turbe, M., "Modeling, Control, and Flight Testing of a Small Ducted-Fan Aircraft," *Journal of Guidance, Control, and Dynamics*, Vol. 29, No. 4, 2006, pp. 769–779.

[14] He, C. and Xin, H., "An Unsteady Ducted Fan Model for Rotorcraft Flight Simulation," *Annual Forum Proceedings - AHS International*, Vol. 2, Phoenix, AZ, United States, 2006, pp. 1081–1097.

[15] Abbot, I. H. and Von Doenhoff, A. E., *Theory of Wing Sections*, Dover Publications, Inc., New York, NY, United States, 2nd ed., 1959.

[16] Phillips, W., "Propeller Momentum Theory with Slipstream Rotation," *Journal of Aircraft*, Vol. 39, No. 1, 2002, pp. 184–187.

[17] Pereira, J. and Chopra, I., "Performance and Surface Pressure Measurements on a MAV-Scale Shrouded Rotor in Translational Flight," *Annual Forum Proceedings - AHS International*, Vol. 3, Virginia Beach, VA, United States, 2007, pp. 2330–2353.

[18] Fleming, J., Jones, T., Lusardi, J., Gelhausen, P., and Enns, D., "Improved Control of Ducted Fan VTOL UAVs in Crosswind Turbulence," *AHS International 4th Decennial Specialists' Conference on Aeromechanics*, San Francisco, CA, United States, 2004, pp. 17–28.

[19] Birkbeck, N., Levesque, J., and Amaral, J. N., "A Dimension Abstraction Approach to Vectorization in Matlab," *International Symposium on Code Generation and Optimization, CGO 2007*, San Jose, CA, United States, 2007, pp. 115–127.

[20] Kuo, B. C. and Golnaraghi, F., *Automatic Control Systems*, John Wiley and Sons, Inc., Hoboken, NJ, United States, 8th ed., 2003.

[21] Pitt, D. and Peters, D., "Theoretical Prediction of Dynamic-Inflow Derivatives," *Vertica*, Vol. 5, No. 1, 1981, pp. 21–34.